

Binary Black Hole Mergers in the first Advanced LIGO Observing Run

The LIGO Scientific Collaboration and The Virgo Collaboration^a
(16 JUNE 2016)

The first observational run of the Advanced LIGO detectors, from September 12, 2015 to January 19, 2016, saw the first detections of gravitational waves from binary black hole mergers. In this paper we present full results from a search for binary black hole merger signals with total masses up to $100M_{\odot}$ and detailed implications from our observations of these systems. Our search, based on general-relativistic models of gravitational wave signals from binary black hole systems, unambiguously identified two signals, GW150914 and GW151226, with a significance of greater than 5σ over the observing period. It also identified a third possible signal, LVT151012, with substantially lower significance, which has a 87% probability of being of astrophysical origin. We provide detailed estimates of the parameters of the observed systems. Both GW150914 and GW151226 provide an unprecedented opportunity to study the two-body motion of a compact-object binary in the large velocity, highly nonlinear regime. We do not observe any deviations from general relativity, and place improved empirical bounds on several high-order post-Newtonian coefficients. From our observations we infer stellar-mass binary black hole merger rates lying in the range $9\text{--}240\text{Gpc}^{-3}\text{yr}^{-1}$. These observations are beginning to inform astrophysical predictions of binary black hole formation rates, and indicate that future observing runs of the Advanced detector network will yield many more gravitational wave detections.

I. INTRODUCTION

The first observing run (O1) of the Advanced LIGO detectors took place from September 12, 2015, to January 19, 2016. The detectors provided unprecedented sensitivity to gravitational waves over a range of frequencies from 30 Hz to several kHz [1], which covers the frequencies of gravitational waves emitted during the late inspiral, merger and ring-down of stellar-mass binary black holes (BBHs). In this paper, we report the results of a matched-filter search using relativistic models of BBH waveforms during the whole of the first Advanced LIGO observing run. The compact binary coalescence (CBC) search targets gravitational-wave emission from compact-object binaries with individual masses from $1M_{\odot}$ to $99M_{\odot}$, total mass less than $100M_{\odot}$ and dimensionless spins up to 0.99. Here we report on results of the search for BBHs. The search was performed using two independently implemented analyses, referred to as PyCBC [2–4] and GstLAL [5–7]. These analyses use a common set of template waveforms [8–10], but differ in their implementations of matched filtering [11, 12], their use of detector data-quality information [13], the techniques used to mitigate the effect of non-Gaussian noise transients in the detector [5, 14], and the methods for estimating the noise background of the search [3, 15]. We obtain results that are consistent between the two analyses.

The search identified two BBH mergers: GW150914, observed on September 14, 2015 at 09:50:45 UTC [16], and GW151226, observed on December 26, 2015 at 03:38:53 UTC [17]. Both of these signals were observed with a significance greater than 5σ . In addition a third candidate event, LVT151012, consistent with a BBH merger was observed on October 12, 2015 at 09:54:43 UTC with a significance of $\lesssim 2\sigma$. Although LVT151012 is not significant enough to claim an unambiguous detection, it is more likely to have re-

sulted from a gravitational-wave signal than from an instrumental or environmental noise transient. The key parameters of these events are summarized in Table I.

The properties of the sources can be inferred from the observed gravitational waveforms. In particular, the binary evolution, which is encoded in the phasing of the gravitational wave signal, is governed by the masses and spins of the binary components. The sky location of the source is primarily determined through time of arrival differences at the two Advanced LIGO sites. The observed amplitudes and relative phase of the signal in the two Advanced LIGO detectors can be used to further restrict the sky location and infer the distance to the source and the binary orientation. We provide a detailed evaluation of the source properties and inferred parameters of GW150914, GW151226 and LVT151012. We use models of the waveform covering the inspiral, merger and ringdown phases based on combining post-Newtonian (PN) theory [18–23], the effective-one-body (EOB) formalism [24–28] and numerical relativity simulations [29–35]. One model is restricted to spins aligned with the orbital angular momentum [8, 9] while the other allows for non-aligned orientation of the spins, which can lead to precession of the orbital plane [36, 37]. The parameters of GW150914 have been reported previously in [38, 39]. We provide revised results which make use of updated instrumental calibration.

The emitted signals depend upon the strong field dynamics of general relativity; thus our observations provide an extraordinary opportunity to test the predictions of general relativity for binary coalescence waveforms. Several tests of general relativity were performed using GW150914, as described in [41]. One of these was a parametrized test for the consistency of the observed waveform with a general relativity based model. We perform a similar test on GW151226. Since this source is of lower mass than GW150914, the observed waveform lasts for many more cycles in the detector data, allowing us to better constrain the PN coefficients that describe the evolution of the binary through the inspiral phase. In addition, we combine the results from GW150914 and GW151226 to place still tighter bounds on deviations from general relativity.

^a Full author list given at the end of the article

| Event | GW150914 | GW151226 | LVT151012 |
|---|------------------------------------|------------------------------------|------------------------------------|
| Signal-to-noise ratio ρ | 23.7 | 13.0 | 9.7 |
| False alarm rate FAR/yr ⁻¹ | $< 6.0 \times 10^{-7}$ | $< 6.0 \times 10^{-7}$ | 0.37 |
| p-value | 7.5×10^{-8} | 7.5×10^{-8} | 0.045 |
| Significance | $> 5.3 \sigma$ | $> 5.3 \sigma$ | 1.7σ |
| Primary mass $m_1^{\text{source}}/M_\odot$ | $36.2^{+5.2}_{-3.8}$ | $14.2^{+8.3}_{-3.7}$ | 23^{+18}_{-6} |
| Secondary mass $m_2^{\text{source}}/M_\odot$ | $29.1^{+3.7}_{-4.4}$ | $7.5^{+2.3}_{-2.3}$ | 13^{+4}_{-5} |
| Chirp mass $\mathcal{M}^{\text{source}}/M_\odot$ | $28.1^{+1.8}_{-1.5}$ | $8.9^{+0.3}_{-0.3}$ | $15.1^{+1.4}_{-1.1}$ |
| Total mass $M^{\text{source}}/M_\odot$ | $65.3^{+4.1}_{-3.4}$ | $21.8^{+5.9}_{-1.7}$ | 37^{+13}_{-4} |
| Effective inspiral spin χ_{eff} | $-0.06^{+0.14}_{-0.14}$ | $0.21^{+0.20}_{-0.10}$ | $0.0^{+0.3}_{-0.2}$ |
| Final mass $M_f^{\text{source}}/M_\odot$ | $62.3^{+3.7}_{-3.1}$ | $20.8^{+6.1}_{-1.7}$ | 35^{+14}_{-4} |
| Final spin a_f | $0.68^{+0.05}_{-0.06}$ | $0.74^{+0.06}_{-0.06}$ | $0.66^{+0.09}_{-0.10}$ |
| Radiated energy $E_{\text{rad}}/(M_\odot c^2)$ | $3.0^{+0.5}_{-0.4}$ | $1.0^{+0.1}_{-0.2}$ | $1.5^{+0.3}_{-0.4}$ |
| Peak luminosity $\ell_{\text{peak}}/(\text{erg s}^{-1})$ | $3.6^{+0.5}_{-0.4} \times 10^{56}$ | $3.3^{+0.8}_{-1.6} \times 10^{56}$ | $3.1^{+0.8}_{-1.8} \times 10^{56}$ |
| Luminosity distance D_L/Mpc | 420^{+150}_{-180} | 440^{+180}_{-190} | 1000^{+500}_{-500} |
| Source redshift z | $0.09^{+0.03}_{-0.04}$ | $0.09^{+0.03}_{-0.04}$ | $0.20^{+0.09}_{-0.09}$ |
| Sky localization $\Delta\Omega/\text{deg}^2$ | 230 | 850 | 1600 |

TABLE I. Details of the three most significant events. The false alarm rate, p-value and significance are from the PyCBC analysis; the GstLAL results are consistent with this. For source parameters, we report median values with 90% credible intervals that include statistical errors, and systematic errors from averaging the results of different waveform models. The uncertainty for the peak luminosity includes an estimate of additional error from the fitting formula. The sky localization is the area of the 90% credible area. Masses are given in the source frame; to convert to the detector frame multiply by $(1+z)$. The source redshift assumes standard cosmology [40].

The observed events begin to reveal a population of stellar-mass black hole mergers. We use these signals to constrain the rates of BBH mergers in the universe, and begin to probe the mass distribution of black hole mergers. The inferred rates are consistent with those derived from GW150914 [42]. We also discuss the astrophysical implications of the observations and the prospects for future Advanced LIGO and Virgo observing runs.

The results presented here are restricted to BBH systems with total masses less than $100M_\odot$. Searches for more massive black holes, compact binary systems containing neutron stars and unmodeled transient signals will be reported elsewhere.

This paper is organized as follows: Sec. II provides an overview of the Advanced LIGO detectors during the first observing run, and the data used in the search. Sec. III presents the results of the search, details of the two gravitational wave events, GW150914 and GW151226, and the candidate event LVT151012. Sec. IV provides detailed parameter-estimation results for the events. Sec. V presents results for the consistency of the two events, GW150914 and GW151226, with the predictions of general relativity. Sec. VI presents the inferred rate of stellar-mass BBH mergers, and VII discusses the implications of these observations and future prospects. We include appendices that provide additional technical details of the methods used. Appendix A describes the CBC search, with A 1 and A 2 presenting details of the construction and tuning of the two independently implemented analyses used in the search, highlighting differences from the methods described in [43]. Appendix B provides a description of the parameter-estimation analysis and includes a summary table of results for all three events. Appendix C and Appendix D provide details of the methods used to infer merger rates and mass distributions respectively.

II. OVERVIEW OF THE INSTRUMENTS AND THE DATA SET

The two Advanced LIGO detectors, one located in Hanford, Washington (H1) and one in Livingston, Louisiana (L1) are modified Michelson interferometers with 4-km long arms. The interferometer mirrors act as test masses, and the passage of a gravitational wave induces a differential arm length change which is proportional to the gravitational-wave strain amplitude. The Advanced LIGO detectors came on line in September 2015 after a major upgrade targeting a 10-fold improvement in sensitivity over the initial LIGO detectors [44]. While not yet operating at design sensitivity, both detectors reached an instrument noise 3 to 4 times lower than ever measured before in their most sensitive frequency band between 100 Hz and 300 Hz [1]. The corresponding observable volume of space for BBH mergers, in the mass range reported in this paper, was ~ 30 times greater, enabling the successful search reported here.

The typical instrument noise of the Advanced LIGO detectors during O1 is described in detail in [46]. In the left panel of Figure 1 we show the amplitude spectral density of the total strain noise of both detectors ($\sqrt{S(f)}$), calibrated in units of strain per $\sqrt{\text{Hz}}$ [47]. Overlaid on the noise curves of the detectors, the waveforms of GW150914, GW151226 and LVT151012 are also shown. The expected SNR ρ of a signal, $h(t)$, can be expressed as

$$\rho^2 = \int_0^\infty \frac{(2|\tilde{h}(f)|\sqrt{f})^2}{S_n(f)} d\ln(f), \quad (1)$$

where $\tilde{h}(f)$ is the Fourier transform of the signal. Writing it in this form motivates the normalization of the waveform plotted in Figure 1 as the area between the signal and noise curves is indicative of the SNR of the events.

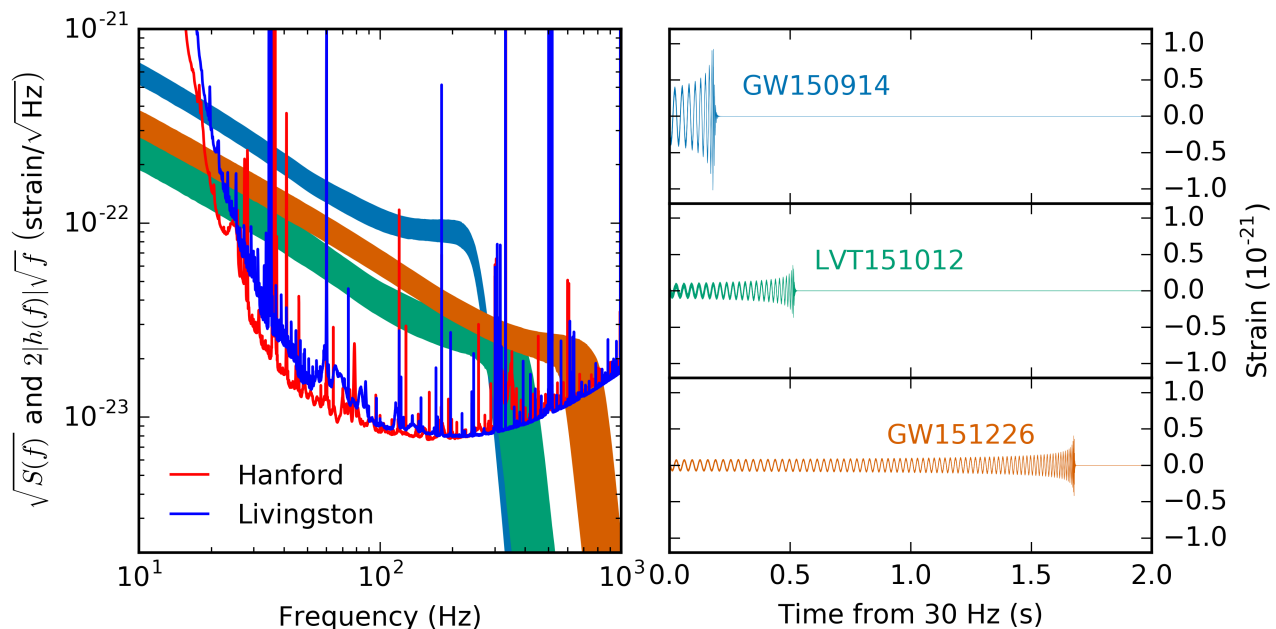


FIG. 1. Left: Amplitude spectral density of the total strain noise of the H1 and L1 detectors, $\sqrt{S(f)}$, in units of strain per $\sqrt{\text{Hz}}$, and the recovered signals of GW150914, GW151226 and LVT151012 plotted so that the relative amplitudes can be related to the SNR of the signal (as described in the text). Right: Time evolution of the waveforms from when they enter the detectors' sensitive band at 30 Hz. All bands show the 90% credible regions of the LIGO Hanford signal reconstructions from a coherent Bayesian analysis using a non-precessing spin waveform model [45].

The gravitational-wave signal from a BBH merger takes the form of a chirp, increasing in frequency and amplitude as the black holes spiral inwards. The amplitude of the signal is maximum at the merger, after which it decays rapidly as the final black hole rings down to equilibrium. In the frequency domain, the amplitude decreases with frequency during inspiral, as the signal spends a greater number of cycles at lower frequencies. This is followed by a slower falloff during merger and then a steep decrease during the ringdown. The amplitude of GW150914 is significantly larger than the other two events and at the time of the merger the gravitational-wave signal lies well above the noise. GW151226 has lower amplitude but sweeps across the whole detector's sensitive band up to nearly 800 Hz. The corresponding time series of the three waveforms are plotted in the right panel of Figure 1 to better visualize the difference in duration within the Advanced LIGO band: GW150914 lasts only a few cycles while LVT151012 and GW151226 have lower amplitude but last longer.

The analysis presented in this paper includes the total set of O1 data from September 12, 2015 to January 19, 2016, which contains a total coincident analysis time of 51.5 days accumulated when both detectors were operating in their normal state. As described in [13] with regard to the first 16 days of O1 data, the output data of both detectors typically contain non-stationary and non-Gaussian features, in the form of transient noise artifacts of varying durations. Longer duration artifacts, such as non-stationary behavior in the interferometer noise, are not very detrimental to CBC searches as they occur on a time-scale that is much longer than any CBC wave-

form. However, shorter duration artifacts can pollute the noise background distribution of CBC searches. Many of these artifacts have distinct signatures [48] visible in the auxiliary data channels from the large number of sensors used to monitor instrumental or environmental disturbances at each observatory site [49]. When a significant noise source is identified, contaminated data are removed from the analysis data set. After applying this data quality process, detailed in [50], the remaining coincident analysis time in O1 is 48.6 days. The analyses search only stretches of data longer than a minimum duration, to ensure that the detectors are operating stably. The choice is different in the two analyses and reduces the available data to 46.1 days for the PyCBC analysis and 48.3 days for the GstLAL analysis.

III. SEARCH RESULTS

Two different, largely independent, analyses have been implemented to search for stellar-mass BBH signals in the data of O1: PyCBC [2–4] and GstLAL [5–7]. Both these analyses employ matched filtering [51–59] with waveforms given by models based on general relativity [8, 9] to search for gravitational waves from binary neutron stars, BBHs, and neutron star–black hole binaries. In this paper, we focus on the results of the matched filter search for BBHs. Results of the searches for binary neutron stars and neutron star–black hole binaries will be reported elsewhere. These matched-filter searches are complemented by generic transient searches which are sensi-

tive to BBH mergers with total mass $\sim 30M_\odot$ or greater [60].

A bank of template waveforms is used to cover the parameter space to be searched [53, 61–64]. The gravitational waveforms depend upon the masses $m_{1,2}$ (using the convention that $m_1 \geq m_2$), and angular momenta $S_{1,2}$ of the binary components. We characterise the angular momentum in terms of the dimensionless spin magnitude

$$a_{1,2} = \frac{c}{Gm_{1,2}^2} |S_{1,2}|, \quad (2)$$

and the component aligned with the direction of the orbital angular momentum, L , of the binary [65, 66],

$$\chi_{1,2} = \frac{c}{Gm_{1,2}^2} S_{1,2} \cdot \hat{L}. \quad (3)$$

We restrict this template bank to systems for which the spin of the systems is aligned (or anti-aligned) with the orbital angular momentum of the binary. Consequently, the waveforms depends primarily upon the chirp mass [67–69]

$$\mathcal{M} = \frac{(m_1 m_2)^{3/5}}{M^{1/5}}, \quad (4)$$

the mass ratio [18]

$$q = \frac{m_2}{m_1} \leq 1, \quad (5)$$

and the effective spin parameter [70–73]

$$\chi_{\text{eff}} = \frac{m_1 \chi_1 + m_2 \chi_2}{M}, \quad (6)$$

where $M = m_1 + m_2$ is the binary’s total mass. The chirp mass and effective spin are combinations of masses and spin which have significant impact on the evolution of the inspiral, and are therefore accurately measured parameters for gravitational waveforms [56, 74–77].

The minimum black hole mass is taken to be $2M_\odot$, consistent with the largest known masses of neutron stars [78]. There is no known maximum black hole mass [79], however we limit this template bank to binaries with a total mass less than $M \leq 100M_\odot$. For higher mass binaries, the Advanced LIGO detectors are sensitive to only the final few cycles of inspiral plus merger, making the analysis more susceptible to noise transients. The results of searches for more massive BBH mergers will be reported in future publications. In principle, black hole spins can lie anywhere in the range from -1 (maximal and anti-aligned) to $+1$ (maximal and aligned). We limit the spin magnitude to less than 0.99, which is the region over which we are able to generate valid template waveforms [8]. The bank of templates used for the analysis is shown in Figure 2.

Both analyses separately correlate the data from each detector with template waveforms that model the expected signal. The analyses identify candidate events that are detected at both the Hanford and Livingston observatories consistent with the 10 ms inter-site propagation time. Additional signal consistency tests are performed to mitigate the effects of

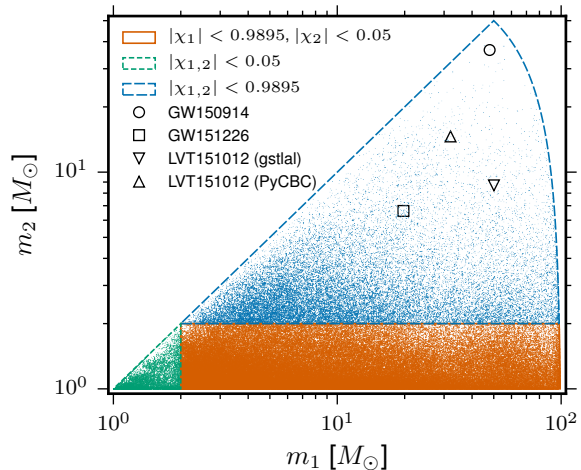


FIG. 2. The four-dimensional search parameter space covered by the template bank shown projected into the component-mass plane, using the convention $m_1 > m_2$. The colours indicate mass regions with different limits on the dimensionless spin parameters χ_1 and χ_2 . Symbols indicate the best matching templates for GW150914, GW151226 and LVT151012. For GW150914, GW151226 the template was the same in the PyCBC and GstLAL searches while for LVT151012 they differed. The parameters of the best matching templates are not the same as the detector frame masses provided by the detailed parameter estimation discussed in Section IV.

non-stationary transients in the data. Events are assigned a detection-statistic value that ranks their likelihood of being a gravitational-wave signal. For PyCBC, $\hat{\rho}_c$ is the quadrature sum of signal-consistency re-weighted SNRs in the two detectors. For GstLAL, $\ln \mathcal{L}$ is the log-likelihood ratio for the signal and noise models. The detection statistics are compared to the estimated detector noise background to determine, for each candidate event, the probability that detector noise would give rise to at least one equally significant event. Further details of the analysis methods are available in Appendix A.

The results for the two different analyses are presented in Figure 3. The figure shows the observed distribution of events, as well as the background distribution used to assess significance. In both analyses, there are three events that lie above the estimated background: GW150914, GW151226 and LVT151012. All three of these are consistent with being BBH merger signals and are discussed in further detail below. The templates producing the highest significance in the two analyses are indicated in Figure 2, the gravitational waveforms are shown in Figure 1 and key parameters are summarized in Table I. There were no other significant BBH triggers in the first advanced LIGO observing run. All other observed events are consistent with the noise background for the search. Follow up of the coincident events $\hat{\rho}_c \approx 9$ in the PyCBC analysis suggests that they are likely due to noise fluctuations or poor data quality, rather than a population of weaker gravitational-wave signals.

It is clear from Figure 3 that at high significance, the background distribution is dominated by the presence of GW150914 in the data. Consequently, once an event has

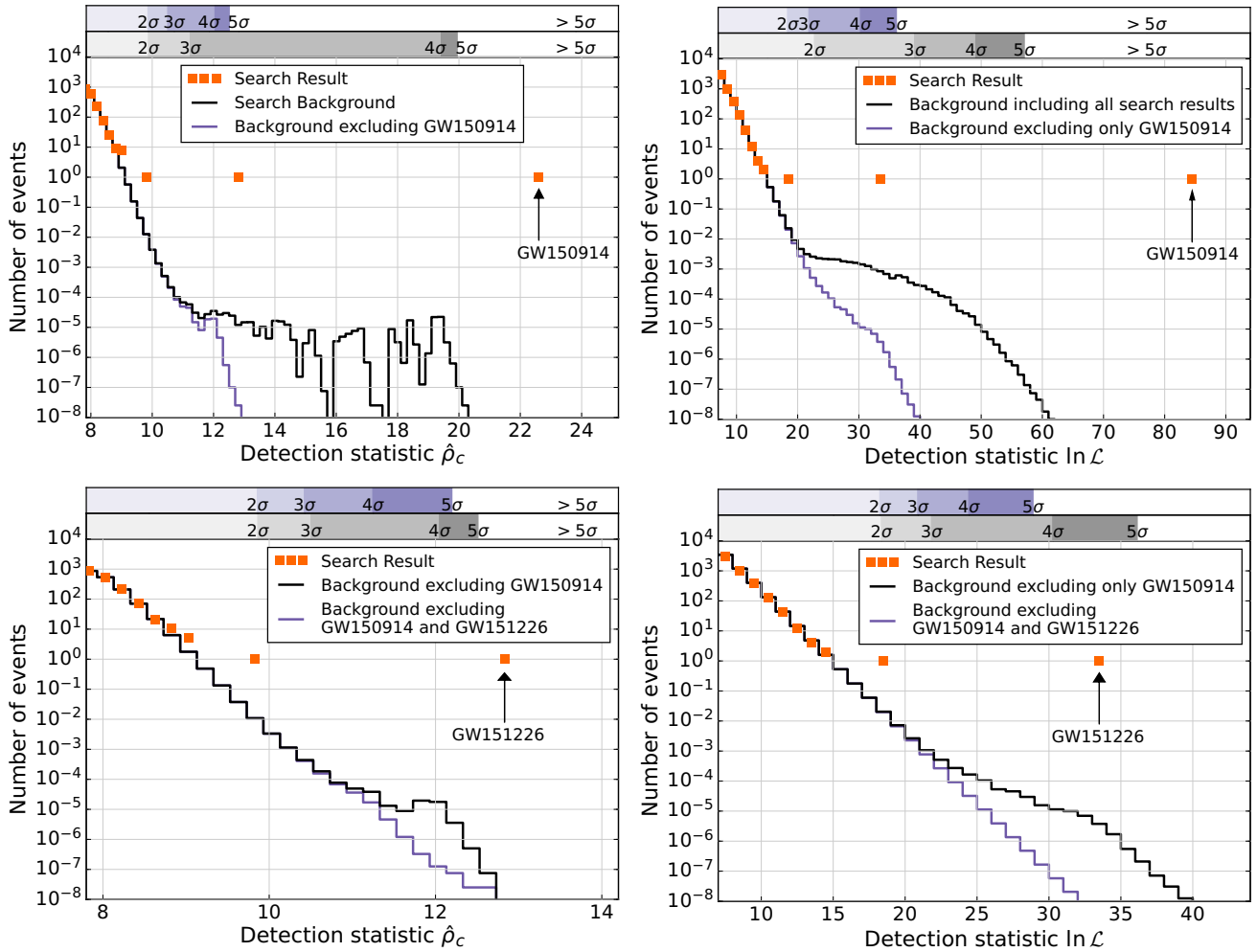


FIG. 3. Search results from the two analyses. The upper left hand plot shows the PyCBC result for signals with chirp mass $\mathcal{M} > 1.74M_{\odot}$ (the chirp mass of a $m_1 = m_2 = 2M_{\odot}$ binary) and $f_{\text{peak}} > 100\text{Hz}$ while the upper right hand plot shows the GstLAL result. In both analyses, GW150914 is the most significant event in the data, and is more significant than any background event in the data. It is identified with a significance greater than 5σ in both analyses. As GW150914 is so significant, the high significance background is dominated by its presence in the data. Once it has been identified as a signal, we remove it from the background estimation to evaluate the significance of the remaining events. The lower plots show results with GW150914 removed from both the foreground and background, with the PyCBC result on the left and GstLAL result on the right. In both analyses, GW151226 is identified as the most significant event remaining in the data. GW151226 is more significant than the remaining background in the PyCBC analysis, with a significance of greater than 5σ . In the GstLAL search GW151226 is measured to have a significance of 4.5σ . The third most significant event in the search, LVT151012 is identified with a significance of 1.7σ and 2.0σ in the two analyses respectively. The significance obtained for LVT151012 is only marginally affected by including or removing background contributions from GW150914 and GW151226.

been confidently identified as a signal, we remove triggers associated to it from the background in order to get an accurate estimate of the noise background for lower amplitude events. The lower panel of Figure 3 shows the search results with GW150914 removed from both the foreground and background distributions.

A. GW150914

GW150914 was observed on September 14, 2015 at 09:50:45 UTC with a matched filter SNR of 23.7.¹ It is recovered with a re-weighted SNR in the PyCBC analysis of $\hat{\rho}_c = 22.7$ and a likelihood of 84.7 in the GstLAL analysis. A detailed discussion of GW150914 is given in [16, 38, 43], where it was presented as the most significant event in the first

¹ We quote the matched filter SNR as computed by the PyCBC search using the updated calibration, the GstLAL values agree within 2%.

16 days of Advanced LIGO observing. The results presented here differ from the previous ones in two ways: they make use of the full O1 data set, and they use the final instrumental calibration. Thus, while GW150914 remains the most significant in this search, the recovered SNR and significance of the event differ slightly from the previously reported values. In particular, for the PyCBC analysis, the event is recovered with slightly lower SNR than with the preliminary calibration and with a higher value of the χ^2 signal consistency test in the H1 detector. This leads to a reduction of the detection statistic, $\hat{\rho}_c$, from 23.6 in [16] to the current value of 22.7. Additionally, for the PyCBC analysis, a re-definition of the mass bins used to group templates with similar background, caused the significance of GW150914 to be evaluated against a different background.² For the GstLAL analysis of the full O1 data set, a decrease in the background probability for GW150914 increased the likelihood over the original value of 78.

GW150914 remains the most significant event in both analyses. Furthermore, in both cases, there are no background events with significance equal to or greater than GW150914. Consequently, we can only calculate a limit on the false alarm rate (FAR) for GW150914. Using the time-shift method to estimate background, we limit the FAR of GW150914 to be less than $6.0 \times 10^{-7} \text{ yr}^{-1}$. This corresponds to a p-value of 7.5×10^{-8} , or a significance of 5.3σ . The significance is greater than the 5.1σ derived in [43] due to a tripling of the analysis time, which allows time-shifts to probe smaller false alarm rates.

The GstLAL analysis estimates the p-value assuming that noise triggers are equally likely to occur in any of the templates within a background bin. Under this assumption, the GstLAL analysis estimates the p-value of GW150914 to be 8.8×10^{-12} , which is the minimum p-value that can be informed by the data. However, as stated in [43], breaking that assumption implies that the minimum p-value would be higher. For this reason we quote the more conservative PyCBC bound on the false alarm probability of GW150914 here and in Ref. [16].

B. GW151226

GW151226 was observed on December 26, 2015 at 03:38:53 UTC with a combined matched filter SNR of 13.0. The signal was identified as the second most significant event in both the PyCBC and GstLAL analyses with $\hat{\rho}_c = 12.8$ and $\ln \mathcal{L} = 22.6$ respectively.

Signal consistency tests show no sign of transient noise affecting the analyses at this time, and checks of the instrumental data reveal no serious data quality issues at the time of the event. When single interferometer triggers from GW150914

are used in our background estimation methods, the tail of the distribution is dominated by their presence. As GW150914 is confidently identified as a gravitational wave signal [16], we remove any background events associated to it from the distribution.

The background distribution, under the assumption that GW150914 is a gravitational wave, is shown in the bottom row of Fig. 3. Now, GW151226 is more significant than all background events in the PyCBC analysis. Its significance cannot be measured and, as for GW150914, we limit the FAR to be less than $6.0 \times 10^{-7} \text{ yr}^{-1}$. This corresponds to a p-value of 7.5×10^{-8} , or a significance of 5.3σ . In the GstLAL analysis the background extends past the observed likelihood of GW151226, and the event is recovered with a FAR of 1 per 44000 years which corresponds to a p-value of 3.5×10^{-6} and a significance of 4.5σ .

C. LVT151012

The third most significant event in O1 is LVT151012 observed on October 12, 2015 at 09:54:43 UTC. It was observed with a combined matched-filter SNR of 9.7, and detection statistic values $\hat{\rho}_c = 9.7$ and $\ln \mathcal{L} = 18.1$. The SNR of this event is considerably lower than GW150914 and GW151226 and, even though the signal consistency tests show no signs of noise origin, the search background is such that the FAR of LVT151012 is 1 per 2.7 years and 1 per 5.9 years in the PyCBC and GstLAL analyses respectively. This equates to p-values of 0.045 and 0.025, or significances of 1.7σ and 2.0σ . For PyCBC, the estimate of the significance is essentially unaffected by the removal of the background associated to GW150914 and GW151226. For GstLAL, inclusion of GW150914 changes the p-value of LVT151012 but inclusion of GW151226 has little effect. These results are consistent with expectations for candidate events with low matched-filter SNR, since PyCBC and GstLAL use different ranking statistics and background estimation methods.

The significance of this event is such that we do not confidently claim this event as a gravitational wave signal. However, it is more likely to be a gravitational wave signal than noise based on our estimate for the rate of gravitational wave signals (see Sec. VI). Detector characterization studies have not identified an instrumental or environmental artifact as causing this candidate event [13]. Parameter-estimation results for LVT151012 are presented in the following section, and these are consistent with our expectations for an astrophysical BBH source. The inferred component masses of LVT151012 lie roughly between the masses of GW150914 and GW151226 as shown in Fig. 4.

IV. SOURCE PROPERTIES

In this Section, we present the inferred properties of the sources of GW150914, LVT151012 and GW151226, assuming that the signals each originate from a binary coalescence as described by general relativity. Tests of the consistency of

² The frequency at peak amplitude of the best-matching template is $f_{\text{peak}} = 144 \text{ Hz}$. With the tuning used for the original result, this placed it in noise-background class (iii) of the PyCBC analysis [43]. However, with the improved O1 tuning, that changed the boundaries of the noise-background classes, this event is in noise-background class (ii).

the signal with the predictions of general relativity are presented in Sec. V. Full results for GW150914 have been provided in [38, 39], and key results for LVT151012 have been given in [43]. Here we give results based upon an updated calibration of the data. The analyses of all three signals closely mirrors the original analysis of GW150914, as detailed in [38], and is described in Appendix B.

The results match our expectations for a coherent signal in both detectors, and give us no reason to suspect that any of the signals are not of astrophysical origin. All three signals are consistent with originating from BBHs. Key parameters for the three events are included in Table I, and detailed results are provided in Table IV in Appendix B.

A. Masses

The binary component masses of all three systems lie within the range expected for stellar-mass black holes. The least massive black hole is the secondary of GW151226, which has a 90% credible lower bound that $m_2^{\text{source}} \geq 5.6 M_\odot$. This is above the expected maximum neutron star mass of $\sim 3 M_\odot$ [80, 81], and beyond the mass gap where there is currently a dearth of black holes observed in x-ray binaries [82–84]. The range of our inferred component masses overlaps with those for stellar-mass black holes measured through x-ray observations, but extends beyond the $\sim 16 M_\odot$ maximum of that population [85–87].

GW150914 corresponds to the heaviest BBH system ($M^{\text{source}} = 65.3^{+4.1}_{-3.4} M_\odot$) we observed and GW151226 corresponds to the least massive ($M^{\text{source}} = 21.8^{+5.9}_{-1.7} M_\odot$). Higher mass systems merge at a lower gravitational wave (GW) frequency. For lower mass systems the GW signal is dominated by the inspiral of the binary components, whereas for higher mass systems the merger and ringdown parts of the signal are increasingly important. The transition from being inspiral-dominated to being merger and ringdown-dominated depends upon the sensitivity of the detector network as a function of frequency; GW150914 had SNR approximately equally split between the inspiral and post-inspiral phases [41]. Information about the masses are encoded in different ways in the different parts of the waveform: the inspiral predominately constrains the chirp mass [69, 74, 88] and the ringdown is more sensitive to the total mass [89]; hence the best measured parameters depend upon the mass [90–92]. This is illustrated in the posterior probability distributions for the three events in Fig. 4. For the lower mass GW151226 and LVT151012, the posterior distribution follows curves of constant chirp mass, but for GW150914 the posterior is shaped more by constraints on the total mass.³

The mass ratio q also differs between the events. We infer that GW150914 came from a near equal mass system (the

90% credible lower bound of the mass ratio is $q \geq 0.65$); but GW151226 and LVT151012 have posterior support for more unequal mass ratios ($q \geq 0.28$ and $q \geq 0.24$ respectively). The mass ratio has a large uncertainty, as it is degenerate with the spin of the compact objects [74, 93, 94]. This degeneracy could be broken if a signal contains a clear imprint of precession [95–97], but we are yet to observe this signature. Measurement of the mass ratio could inform our understanding of the origin of BBH systems.

Following the inspiral, the BBHs merge to form a final remnant black hole. We estimate the masses of these using fitting formulae calibrated to numerical relativity simulations [35, 98]. Each final mass is 0.95–0.98 of the initial total mass of the binary components, as similar fractions of 0.02–0.05 are radiated away as GWs. While predominantly determined by the total mass, the radiated energy also depends upon the mass ratio and component spins; our results are consistent with expectations for moderately spinning black holes [99, 100]. The remnant black holes are more massive than any black hole observed to date in an x-ray binary, the least massive being GW151226’s $M_f^{\text{source}} = 20.8^{+6.1}_{-1.7} M_\odot$. The final black hole masses, as well as their spins, are shown in Fig. 4. The remnant for GW150914 has a mass of $M_f^{\text{source}} = 62.3^{+3.7}_{-3.1} M_\odot$ and is the most massive stellar-mass black hole observed to date.

BBHs mergers have extremely high GW luminosities: the peak values are $3.6^{+0.5}_{-0.4} \times 10^{56} \text{ erg s}^{-1}$, $3.1^{+0.8}_{-1.8} \times 10^{56} \text{ erg s}^{-1}$ and $3.3^{+0.8}_{-1.6} \times 10^{56} \text{ erg s}^{-1}$ for GW150914, LVT151012 and GW151226 respectively. These luminosities are calculated using a fit to non-precessing numerical-relativity simulations [101], and the uncertainty includes the estimated error from this fit. Whereas the energy radiated scales with the total mass, the luminosity is comparable for all three systems. There is some variation from differences in the mass ratios and spins, and uncertainty in these dominate the overall uncertainty. The luminosity is independent of the total mass as this sets both the characteristic energy scale and characteristic time scale for the system.⁴

B. Spins

A black hole has three intrinsic properties: mass, spin and electric charge [103–106]. We expect the charge of astrophysical black holes to be negligible [107–109]. Both the masses and spins of the black holes leave an imprint on the GW signal during a coalescence. However, the effects of the spins of the binary components are sub-dominant, and they are more difficult to constrain than the masses.

Only weak constraints can be placed on the spin magnitudes of the binary components: in all cases the uncertainty spans the majority of the allowed range of $[0, 1]$. We can better infer the spin of the more massive black hole, as this has

³ Correlations are tighter for the detector-frame mass than for the source-frame masses because the latter include additional uncertainty from the redshift.

⁴ For BBHs, the characteristic luminosity is set by the Planck luminosity $c^5/G = 3.6 \times 10^{59} \text{ erg s}^{-1} = 2.0 \times 10^5 M_\odot c^2 \text{ s}^{-1}$ [102], and the peak luminosities are about 0.1% of this.

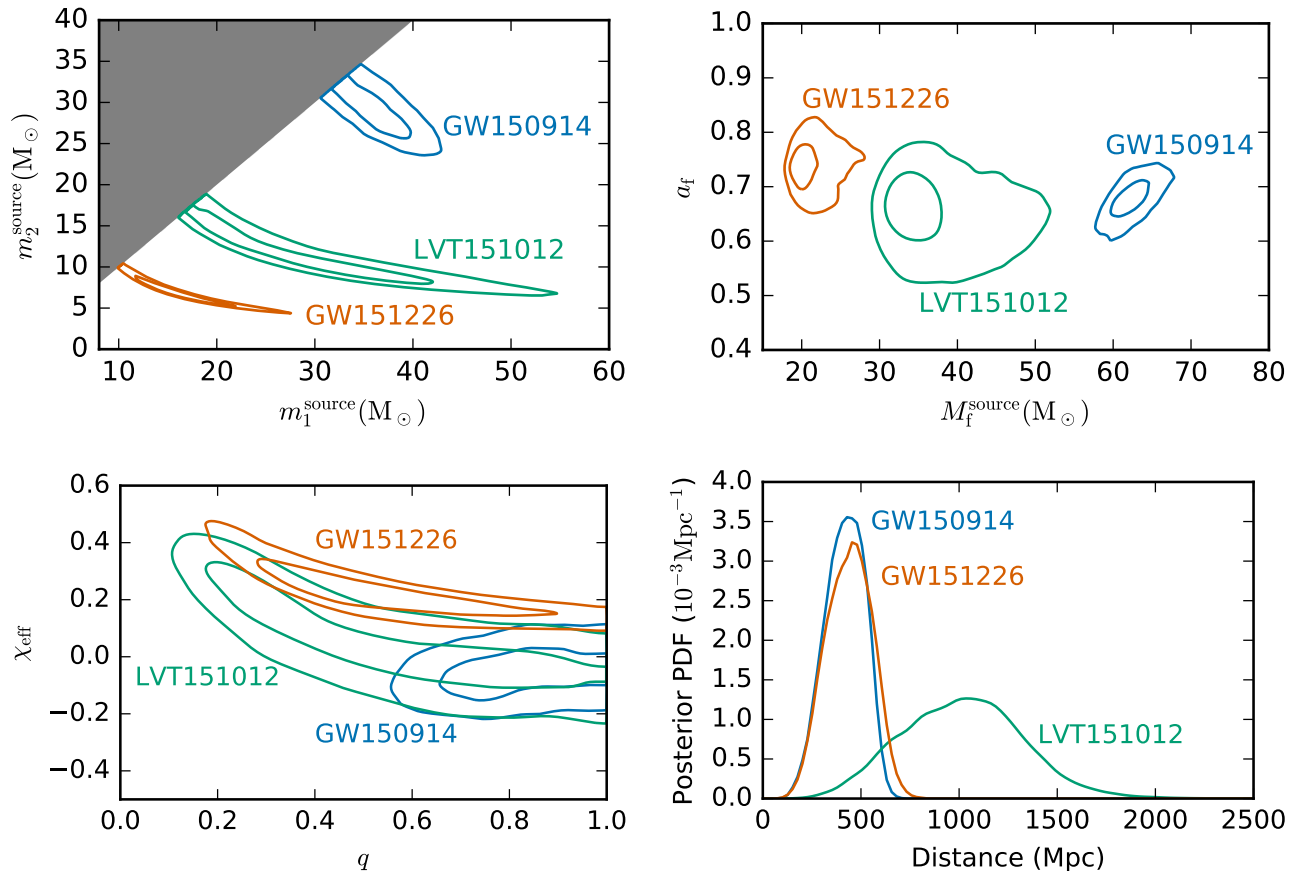


FIG. 4. Posterior probability densities of the masses, spins and distance to the three events GW150914, LVT151012 and GW151226. For the two dimensional distributions, the contours show 50% and 90% credible regions. *Top left:* component masses m_1^{source} and m_2^{source} for the three events. We use the convention that $m_1^{\text{source}} \geq m_2^{\text{source}}$, which produces the sharp cut in the two-dimensional distribution. For GW151226 and LVT151012, the contours follow lines of constant chirp mass ($\mathcal{M}^{\text{source}} = 8.9_{-0.3}^{+0.3} M_\odot$ and $\mathcal{M}^{\text{source}} = 15.1_{-1.1}^{+1.4} M_\odot$ respectively). In all three cases, both masses are consistent with being black holes. *Top right:* The mass and dimensionless spin magnitude of the final black holes. *Bottom left:* The effective spin and mass ratios of the binary components. *Bottom right:* The luminosity distance to the three events.

a greater impact upon the inspiral. We find that smaller spins are favoured, and place 90% credible bounds on the primary spin $a_1 \leq 0.7$ for GW150914, $a_1 \leq 0.7$ for LVT151012, and $a_1 \leq 0.8$ for GW151226. In the case of GW151226, we infer that at least one of the components has a spin of ≥ 0.2 at the 99% credible level.

While the individual component spins are poorly constrained, there are combinations that can be better inferred. The effective spin χ_{eff} , as defined in Equation 6, is a mass-weighted combination of the spins parallel to the orbital angular momentum [71–73]. It is +1 when both the spins are maximal and parallel to the angular momentum, -1 when both spins are maximal and antiparallel to the angular momentum, and 0 when there is no net mass-weighted aligned spin. Systems with positive χ_{eff} complete more cycles when inspiralling from a given orbital separation than those with negative χ_{eff} [70, 110]. While χ_{eff} has a measurable effect on the inspiral, this is degenerate with that of the mass ratio as illustrated for the lower mass inspiral-dominated signals in Fig. 4.

Observations for all three events are consistent with small values of the effective spin: $|\chi_{\text{eff}}| \leq 0.17, 0.28$ and 0.35 at 90% probability for GW150914, LVT151012 and GW151226 respectively. This indicates that large parallel spins aligned or antialigned with the orbital angular momentum are disfavored.

It may be possible to place tighter constraints on each component’s spin by using waveforms that include the full effects of precession [39]. This will be investigated in future analyses.

All three events have final black holes with spins of ~ 0.7 , as expected for mergers of similar-mass black holes [111, 112]. The final spin is dominated by the orbital angular momentum of the binary at merger. Consequently, it is more precisely constrained than the component spins and is broadly similar across the three events. The masses and spins of the final black holes are plotted in Fig. 4.

The spin of the final black hole, like its mass, is calculated using fitting formulae calibrated against numerical relativity simulations. In [38] we used a formula which only included contributions from the aligned components of the com-

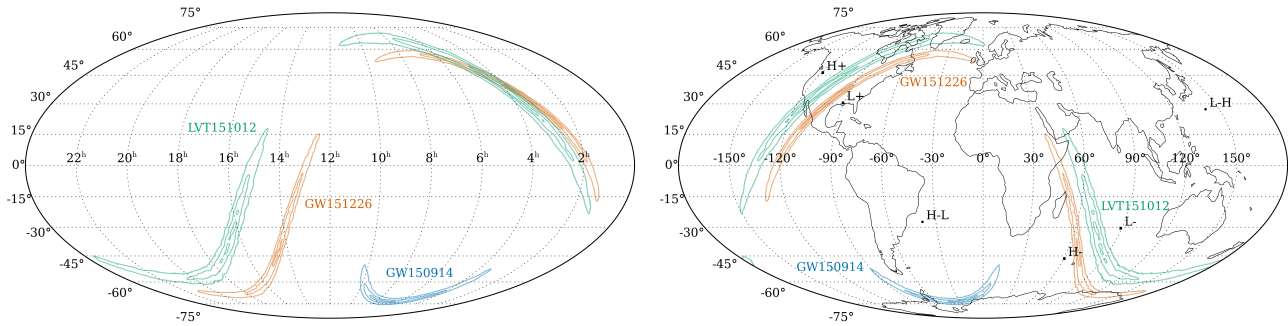


FIG. 5. Posterior probability distributions for the sky locations of GW150914, LVT151012 and GW151226 shown in a Mollweide projection. The left plot shows the probable position of the source in equatorial coordinates (right ascension is measured in hours and declination is measured in degrees). The right plot shows the localization with respect to the Earth at the time of detection. H+ and L+ mark the Hanford and Livingston sites, and H- and L- indicate antipodal points; H-L and L-H mark the poles of the line connecting the two detectors (the points of maximal time delay). The sky localization forms part of an annulus, set by the difference in arrival times between the detectors.

ponents' spins [98]; we now use an updated formula which also incorporates the effects of in-plane spins [113]. This has a small impact on spin of GW150914 (changing from $0.67_{-0.06}^{+0.05}$ to $0.68_{-0.06}^{+0.05}$), and a larger effect on GW151226 (changing from $0.72_{-0.05}^{+0.05}$ to $0.74_{-0.06}^{+0.06}$) as its components have more significant spins.

C. Distance, inclination and sky location

The luminosity distance to the source is inversely proportional to the signal's amplitude. GW150914 and GW151226 have comparable distance estimates of $D_L = 420_{-180}^{+150}$ Mpc (redshift $z = 0.09_{-0.04}^{+0.03}$) and $D_L = 440_{-190}^{+180}$ Mpc ($z = 0.09_{-0.04}^{+0.03}$) respectively.⁵ GW151226 originates from a lower mass system than GW150914 and hence the GW signal is intrinsically quieter, and its SNR is lower than GW150914's even though the distances are comparable. LVT151012 is the quietest signal and is inferred to be at a greater distance $D_L = 1000_{-500}^{+500}$ Mpc ($z = 0.20_{-0.09}^{+0.09}$).

In all cases, there is significant fractional uncertainty for the distance. This is predominantly a consequence of the degeneracy between the distance and the binary's inclination, which also impacts the signal amplitude [93, 115, 116].

The inclination is only weakly constrained; in all cases there is greatest posterior support for the source being either face on or face off (angular momentum pointed parallel or antiparallel to the line of sight). This is the orientation that produces the greatest GW amplitude and so is consistent with the largest distance. The inclination could potentially be better constrained in a precessing system [96, 117]. Only for

GW150914 is there preference for one of the configurations, with there being greater posterior support for the source being face off [38].

Sky localization from a GW detector network is primarily determined by the measured delay in the signal arriving at the sites, with additional information coming from the signal amplitude and phase [118–120]. For a two-detector network, the sky localization forms a characteristic broken annulus [121–124]. Adding additional detectors to the network would improve localization abilities [125–128]. The sky localizations of the three events are shown in Fig. 5; this shows both celestial coordinates (indicating the origin of the signal) and geographic coordinates (illustrating localization with respect to the two detectors). The arrival time at Hanford relative to Livingston was $\Delta t_{HL} = 7.0_{-0.2}^{+0.2}$ ms for GW150914, $\Delta t_{HL} = -0.6_{-0.6}^{+0.6}$ ms for LVT151012, and $\Delta t_{HL} = 1.1_{-0.3}^{+0.3}$ ms for GW151226.

The 90% credible region for sky localization is 230 deg^2 for GW150914, 850 deg^2 for GW151226, and 1600 deg^2 for LVT151012. As expected, the sky area is larger for quieter events. The sky area is expected to scale inversely with the square of the SNR [124, 129], and we see that this trend is followed.

V. TESTS OF GENERAL RELATIVITY

GW150914 provided us with the first empirical access to the genuinely strong-field dynamics of gravity. With the frequency of the waveform peak amplitude well aligned with the best instrument sensitivity, the part of the coalescence just before merger, as well as the merger-ringdown regime, could be studied in considerable detail, as described in [41]. This allowed for checks of the consistency between masses and spins estimated from different portions of the waveform [130], as well as parameterized tests of the waveform as a whole [131–134]. Even though not much of the early inspiral was in the detectors' sensitive band, interesting bounds could be placed on departures from general relativity in the PN coefficients

⁵ We convert between luminosity distance and redshift using a flat Λ CDM cosmology with Hubble parameter $H_0 = 67.9 \text{ km s}^{-1} \text{ Mpc}^{-1}$ and matter density parameter $\Omega_m = 0.306$ [40]. The redshift is used to convert between the observed detector-frame masses and the physical source-frame masses, $m = (1+z)m^{\text{source}}$ [114].

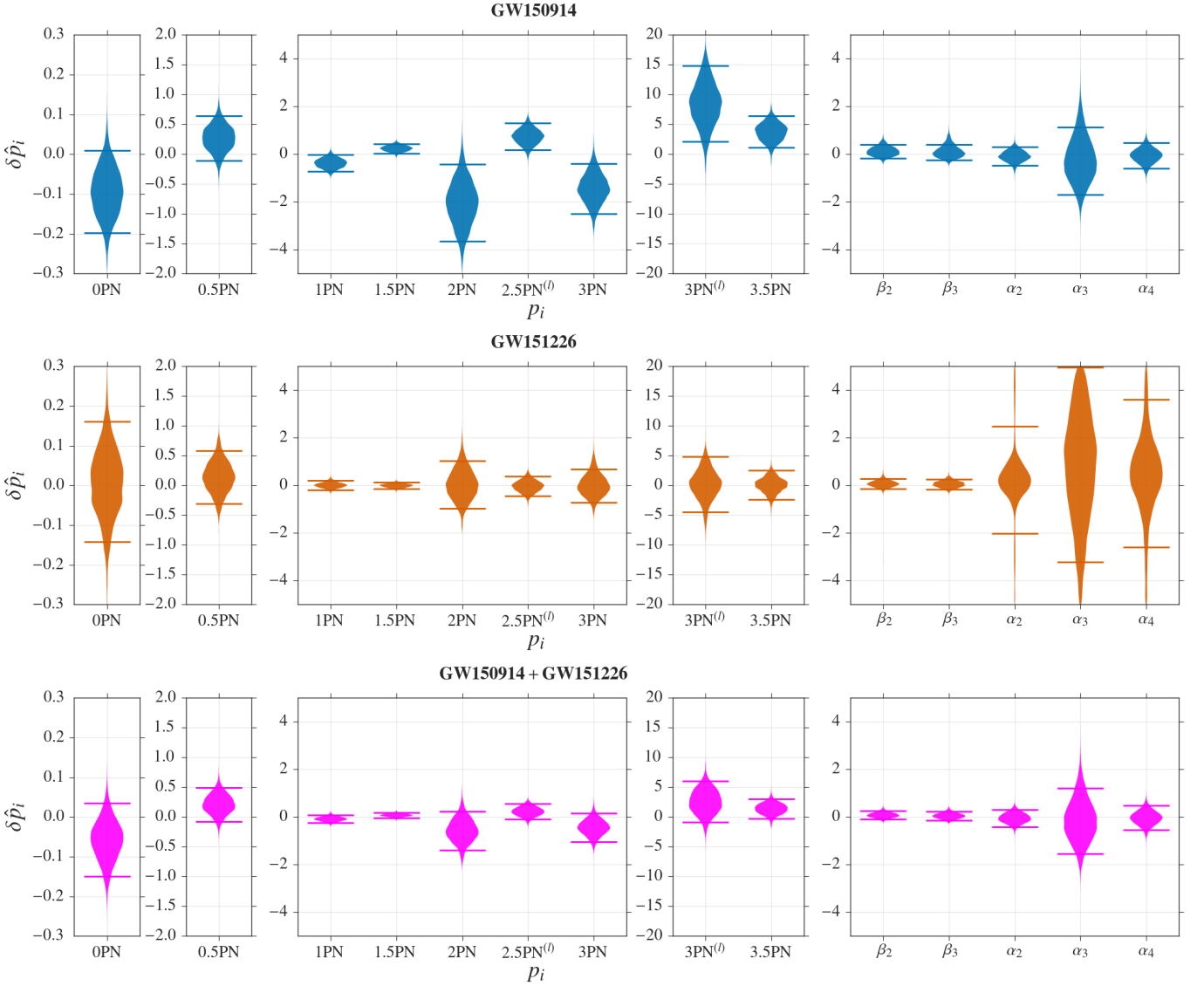


FIG. 6. Posterior density distributions and 90% credible intervals for relative deviations $\delta \hat{p}_i$ in the PN parameters p_i , as well as intermediate parameters β_i and merger-ringdown parameters α_i . The top panel is for GW150914 by itself and the middle one for GW151226 by itself, while the bottom panel shows *combined* posteriors from GW150914 and GW151226. While the posteriors for deviations in PN coefficients from GW150914 show large offsets, the ones from GW151226 are well-centered on zero as well as being more tight, causing the combined posteriors to similarly improve over those of GW150914 alone. For deviations in the β_i , the combined posteriors improve over those of either event individually. For the α_i , the joint posteriors are mostly set by the posteriors from GW150914, whose merger-ringdown occurred at frequencies where the detectors are the most sensitive.

up to 3.5PN. Since the source of GW151226 merged at ~ 450 Hz, the signal provides the opportunity to probe the PN inspiral with many more waveform cycles, albeit at relatively low SNR. Especially in this regime, it allows us to tighten further our bounds on violations of general relativity.

As in [41], to analyze GW151226 we start from the IMR-Phenom waveform model of [35–37] which is capable of describing inspiral, merger, and ringdown, and partly accounts for spin precession. The phase of this waveform is characterized by phenomenological coefficients $\{p_i\}$, which include PN coefficients as well as coefficients describing merger and ringdown. The latter were obtained by calibrating against nu-

merical waveforms and tend to multiply specific powers of f , and they characterize the gravitational-wave amplitude and phase in different stages of the coalescence process. We then allow for possible departures from general relativity, parameterized by a set of testing coefficients $\delta \hat{p}_i$, which take the form of *fractional* deviations in the p_i [135, 136]. Thus, we replace $p_i \rightarrow (1 + \delta \hat{p}_i) p_i$ and let one or more of the $\delta \hat{p}_i$ vary freely in addition to the source parameters that also appear in pure general relativity waveforms, using the general relativity expressions in terms of masses and spins for the p_i themselves. Our testing coefficients are those in Table I of

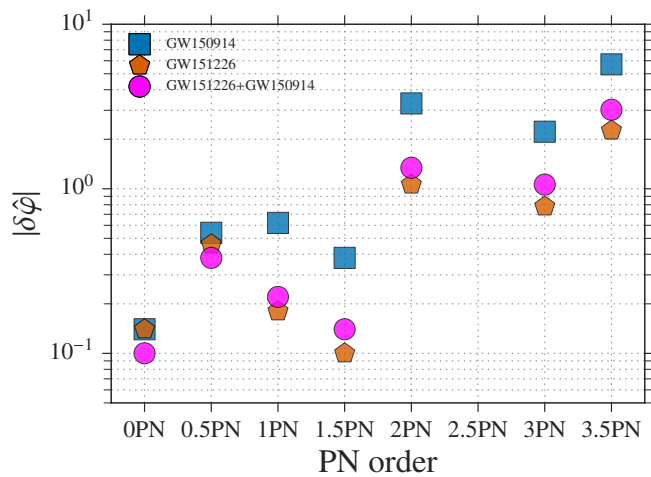


FIG. 7. The 90% credible upper bounds on deviations in the PN coefficients, from GW150914 and GW151226. Also shown are joint upper bounds from the two detections; the main contributor is GW151226, which had many more inspiral cycles in band than GW150914. At 1 PN order and higher the joint bounds are slightly looser than the ones from GW151226 alone; this is due to the large offsets in the posteriors for GW150914.

[41]. For convenience we list them again: (i) $\{\delta\hat{\phi}_0, \dots, \delta\hat{\phi}_7\}$ ⁶ and $\{\delta\hat{\phi}_{5l}, \delta\hat{\phi}_{6l}\}$ for the PN coefficients (where the last two multiply a term of the form $f^\gamma \log f$), (ii) intermediate-regime parameters $\{\delta\hat{\beta}_2, \delta\hat{\beta}_3\}$, and (iii) merger-ringdown parameters $\{\delta\hat{\alpha}_2, \delta\hat{\alpha}_3, \delta\hat{\alpha}_4\}$.⁷

In our analyses we let each one of the $\delta\hat{p}_i$ in turn vary freely while all others are fixed to their general relativity values, $\delta\hat{p}_j = 0$ for $j \neq i$. These tests model general relativity violations that would occur predominantly at a particular PN order (or in the case of the intermediate and merger-ringdown parameters, a specific power of frequency in the relevant regime), although together they can capture deviations that are measurably present at more than one order.⁸

Given more than one detection of BBH mergers, posterior distributions for the $\delta\hat{p}_i$ can be combined to yield stronger constraints. In Fig. 6 we show the posteriors from GW150914, generated with final instrumental calibration, and GW151226 by themselves, as well as joint posteriors from the two events together. We do not present similar results for the candidate LVT151012 since it is not as confident a detection as the others; furthermore, its smaller detection SNR means that its contribution to the overall posteriors is insignificant.

⁶ This includes a 0.5PN testing parameter $\delta\hat{\phi}_1$; since ϕ_1 is identically zero in general relativity, we let $\delta\hat{\phi}_1$ be an absolute rather than a relative deviation.

⁷ We do not consider parameters that are degenerate with the reference time or the reference phase, nor the late-inspiral parameters $\delta\hat{\sigma}_i$ (for which the uncertainty on the calibration can be almost as large as the measurement uncertainty).

⁸ In [41], for completeness we had also shown results from analyses where the parameters in each of the regimes (i)-(iii) are allowed to vary simultaneously; however, these tests return wide and uninformative posteriors.

For GW150914, the testing parameters for the PN coefficients, $\delta\hat{\phi}_i$ and $\delta\hat{\phi}_{il}$, showed moderately significant (2 – 2.5σ) deviations from their general relativity values of zero [41]. By contrast, the posteriors of GW151226 tend to be centered on the general relativity value. As a result, the offsets of the combined posteriors are smaller. Moreover, the joint posteriors are considerably tighter, with a 1 - σ spread as small as 0.07 for deviations in the 1.5PN parameter ϕ_3 , which encapsulates the leading-order effects of the dynamical self-interaction of spacetime geometry (the “tail” effect) [137] as well as spin-orbit interaction [66, 138, 139].

In Fig. 7, we show the 90% credible upper bounds on the magnitude of the fractional deviations in PN coefficients, $|\delta\hat{\phi}_i|$, which are affected by both the offsets and widths of the posterior density functions for the $\delta\hat{\phi}_i$. We show bounds for GW150914 and GW151226 individually, as well as the joint upper bounds resulting from the combined posterior density functions of the two events. Not surprisingly, the quality of the joint bounds is mainly due to GW151226, because of the larger number of inspiral cycles in the detectors’ sensitive frequency band. Note how at high PN order the combined bounds are slightly looser than the ones from GW151226 alone; this is because of the large offsets in the posteriors from GW150914.

Next we consider the intermediate-regime coefficients $\delta\hat{\beta}_i$, which pertain to the transition between inspiral and merger-ringdown. For GW151226, this stage is well inside the sensitive part of the detectors’ frequency band. Returning to Fig. 6, we see that the measurements for GW151226 are of comparable quality to GW150914, and the combined posteriors improve on the ones from either detection by itself.

Last, we look at the merger-ringdown parameters $\delta\hat{\alpha}_i$. For GW150914, this regime corresponded to frequencies of $f \in [130, 300]$ Hz, while for GW151226 it occurred at $f \gtrsim 400$ Hz. As expected, the posteriors from GW151226 are not very informative for these parameters, and the combined posteriors are essentially determined by those of GW150914.

In summary, GW151226 makes its most important contribution to the combined posteriors in the PN inspiral regime, where both offsets and statistical uncertainties have significantly decreased over the ones from GW150914, in some cases to the $\sim 10\%$ level.

An inspiral-merger-ringdown consistency test as performed on GW150914 in [41] is not meaningful for GW151226, since very little of the signal is observed in the post-merger phase. Likewise, the SNR of GW151226 is too low to allow for an analysis of residuals after subtraction of the most probable waveform. Finally, in [41], GW150914 was used to place a lower bound on the graviton Compton wavelength of 10^{13} km. Combining information from the two signals does not significantly improve on this; an updated bound must await further observations.

VI. BINARY BLACK HOLE MERGER RATES

The observations reported here enable us to constrain the rate of BBH coalescences in the local Universe more precisely

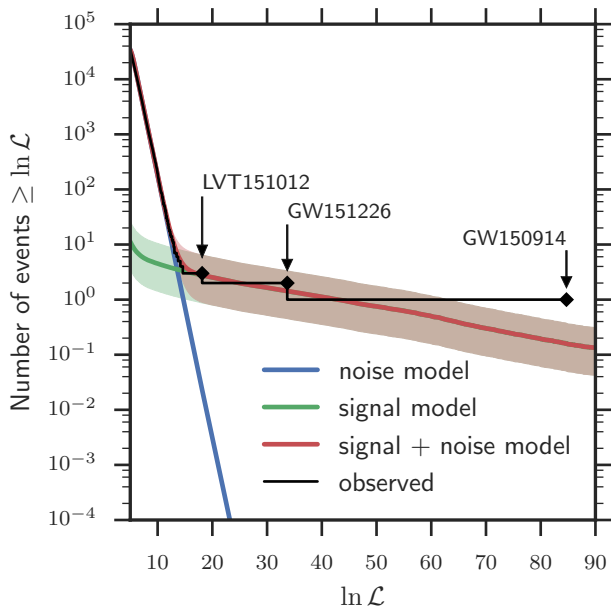


FIG. 8. The cumulative (right to left) distribution of observed triggers in the GstLAL analysis as a function of the log likelihood. The best fit signal + noise distribution, and the contributions from signal and noise are also shown. The shaded regions show 1σ uncertainties. The observations are in good agreement with the model. At low likelihood, the distribution matches the noise model, while at high likelihood it follows the signal model. Three triggers are clearly identified as being more likely to be signal than noise. GW150914 stands somewhat above the expected distribution, as it is an unusually significant event – only 6% of the astrophysical distribution of sources appearing in our search with a false rate of less than one per cent will be more significant than GW150914.

than was achieved in [42], due to the longer duration of data containing a larger number of detected signals.

To do so, we consider two classes of triggers: those whose origin is astrophysical and those whose origin is terrestrial. Terrestrial triggers are the result of either instrumental or environmental effects in the detector, and their distribution is calculated from the search background estimated by the analyses (as shown in Fig. 3). The distribution of astrophysical events is determined by performing large-scale simulations of signals drawn from astrophysical populations and added to the data set. We then use our observations to fit for the number of triggers of terrestrial and astrophysical origin, as discussed in detail in Appendix C. Figure 8 shows the inferred distributions of signal and noise triggers, as well as the combined distribution. The observations are in good agreement with the model.

It is clear from the figure that three triggers are more likely to be signal (i.e. astrophysical) than noise (terrestrial). We evaluate this probability and find that, for GW150914 and GW151226, the probability of astrophysical origin is unity to within one part in 10^6 . Meanwhile for LVT151012, it is calculated to be 0.87 and 0.86, for the PyCBC and GstLAL analyses respectively.

Given uncertainty in the formation channels of the various

| Mass distribution | $R/(\text{Gpc}^{-3}\text{yr}^{-1})$ | | |
|-------------------|-------------------------------------|----------------------|----------------------|
| | PyCBC | GstLAL | Combined |
| Event based | | | |
| GW150914 | $3.2^{+8.3}_{-2.7}$ | $3.6^{+9.1}_{-3.0}$ | $3.4^{+8.6}_{-2.8}$ |
| LVT151012 | $9.2^{+30.3}_{-8.5}$ | $9.2^{+31.4}_{-8.5}$ | $9.4^{+30.4}_{-8.7}$ |
| GW151226 | 35^{+92}_{-29} | 37^{+94}_{-31} | 37^{+92}_{-31} |
| All | 53^{+100}_{-40} | 56^{+105}_{-42} | 55^{+99}_{-41} |
| Astrophysical | | | |
| Flat in log mass | 31^{+43}_{-21} | 30^{+43}_{-21} | 30^{+43}_{-21} |
| Power Law (-2.35) | 100^{+136}_{-69} | 95^{+138}_{-67} | 99^{+138}_{-70} |

TABLE II. Rates of BBH mergers based on populations with masses matching the observed events, and astrophysically motivated mass distributions. Rates inferred from the PyCBC and GstLAL analyses independently as well as combined rates are shown. The table shows median values with 90% credible intervals.

BBH events, we calculate the inferred rates using a variety of source population parametrizations. For a given population, the rate is calculated as $R = \Lambda / \langle VT \rangle$ where Λ is the number of triggers of astrophysical origin and $\langle VT \rangle$ is the population-averaged sensitive space-time volume of the search. We use two canonical distributions for BBH masses:

- i a distribution uniform over the logarithm of component masses, $p(m_1, m_2) \propto m_1^{-1} m_2^{-1}$ and
- ii assuming a power-law distribution in the primary mass, $p(m_1) \propto m_1^{-2.35}$ with a uniform distribution on the second mass.

We require $5M_\odot \leq m_2 \leq m_1$ and $m_1 + m_2 \leq 100M_\odot$. The first distribution probably overestimates the fraction of high-mass black holes and therefore overestimates $\langle VT \rangle$ resulting in an underestimate of the true rate while the second probably overestimates the fraction of low-mass black holes and therefore underestimating $\langle VT \rangle$ and overestimating the true rate. The inferred rates for these two populations are shown in Table II and the rate distributions are plotted in Figure 10.

In addition, we calculate rates based upon the inferred properties of the three significant events observed in the data: GW150914, GW151226 and LVT151012 [140]. Since these classes are distinct, the total event rate is the sum of the individual rates: $R \equiv R_{\text{GW150914}} + R_{\text{LVT151012}} + R_{\text{GW151226}}$. Note that the total rate estimate is dominated by GW151226, as it is the least massive of the three likely signals and is therefore observable over the smallest space-time volume. The results for these population assumptions also are shown in Table II, and in Figure 9. The inferred overall rate is shown in Fig. 10. As expected, the population-based rate estimates bracket the one obtained by using the masses of the observed black hole binaries.

The inferred rates of BBH mergers are consistent with the results obtained in [42] following the observation of GW150914. The median values of the rates have decreased by approximately a factor of two, as we now have three likely

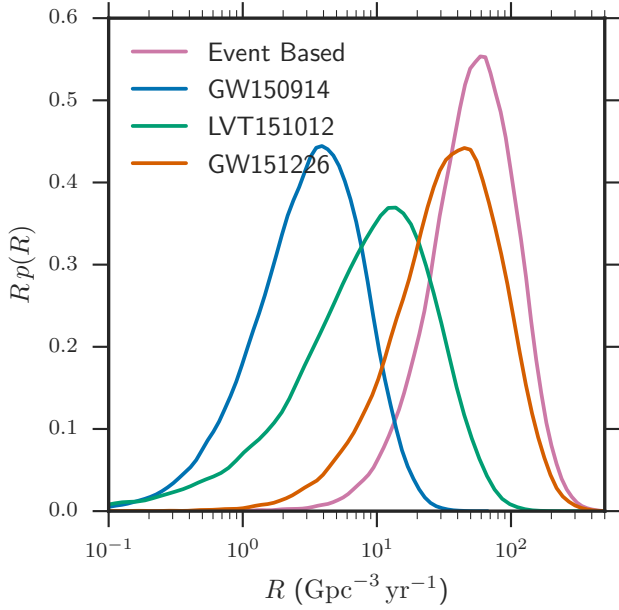


FIG. 9. The posterior density on the rate of GW150914-like BBH, LVT151012-like BBH, and GW151226-like BBH mergers. The event based rate is the sum of these. The median and 90% credible levels are given in Table II.

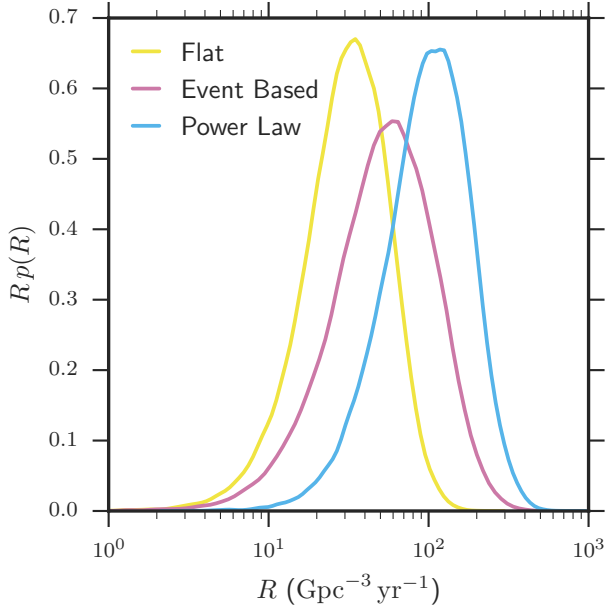


FIG. 10. The posterior density on the rate of BBH mergers. The curves represent the posterior assuming that BBH masses are distributed flat in $\log(m_1)\text{-}\log(m_2)$ (Flat), match the properties of the observed events (Event Based), or are distributed as a power law in m_1 (Power Law). The posterior median rates and symmetric 90% symmetric credible intervals are given in Table II.

signals (rather than two) in three times as much data. Further-

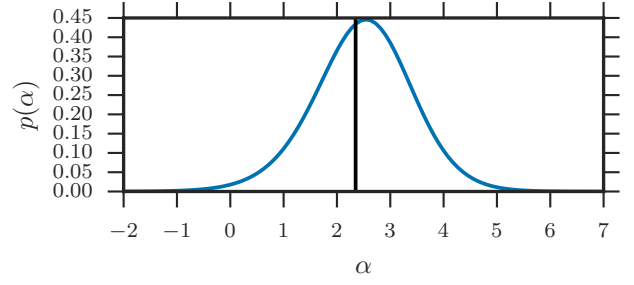


FIG. 11. The posterior distribution for α in Eq. (7) using the inferred masses for our three most significant triggers, GW150914, LVT151012, and GW151226. The vertical line indicates the value of $\alpha = 2.35$ that corresponds to the power law mass distribution used to infer the rate of BBH coalescence. This value is fully consistent with the posterior, which allows a broad range of possible values with a median and 90% credible interval of $\alpha = 2.5^{+1.5}_{-1.6}$.

more, due to the observation of an additional highly significant signal GW151226, the uncertainty in rates has reduced. In particular, the 90% range of allowed rates has been updated to $9\text{--}240\text{ Gpc}^{-3}\text{ yr}^{-1}$, where the lower limit comes from the flat in log mass population and the upper limit from the power law population distribution.

With three significant triggers, GW150914, LVT151012, and GW151226, all of astrophysical origin to high probability, we can begin to constrain the mass distribution of coalescing BBHs. Here we present a simple, parametrized fit to the mass distribution using these triggers; a non-parametric method that can fit general mass distributions will be presented in future work. Our methodology is described more fully in Appendix D.

We assume that the distribution of black hole masses in coalescing binaries follows

$$p(m_1) \propto m_1^{-\alpha}, \quad (7)$$

with $M_{\min} \leq m_2 \leq m_1$ and $m_1 + m_2 \leq 100M_{\odot}$, and a uniform distribution on the secondary mass between $M_{\min} = 5M_{\odot}$ and m_1 . With $\alpha = 2.35$, this mass distribution is the power law distribution used in our rate estimation. Our choice of M_{\min} is driven by a desire to incorporate nearly all the posterior samples from GW151226 and because there is some evidence from electromagnetic observations for a minimum black hole (BH) mass near $5M_{\odot}$ [82, 141] (but see [84]).

We use a hierarchical analysis [141–144] to infer α from the properties of the three significant events — GW150914, GW151226 and LVT151012 — where all three are treated equally and we properly incorporate parameter-estimation uncertainty on the masses of each system. Our inferred posterior on α is shown in Fig. 11. The value $\alpha = 2.35$, corresponding to the power law mass distribution used above to infer rates lies near the peak of the posterior, and the median and broad 90% credible interval is

$$\alpha = 2.5^{+1.5}_{-1.6}. \quad (8)$$

It is not surprising that our fit peaks near $\alpha \sim 2.5$ because the observed sample is consistent with a flat distribution and the sensitive time-volume scales roughly as $M^{15/6}$.

The mass distribution of merging black hole binaries cannot be constrained tightly with such a small number of observations. This power-law fit is sensitive to a number of arbitrary assumptions, including a flat distribution in the mass ratio and a redshift-independent merger rate and mass distribution. Most critically, the fit is sensitive to the choice of the lower mass cutoff M_{\min} : higher choices of M_{\min} lead to a preference for steeper power laws with indices different by a few.

VII. ASTROPHYSICAL IMPLICATIONS AND FUTURE PROSPECTS

In [145], we discussed the astrophysical implications of the first gravitational-wave detection, GW150914, of the merger of two black holes with masses $m_1 = 36.2^{+5.2}_{-3.8} M_{\odot}$ and $m_2 = 29.1^{+3.7}_{-4.4} M_{\odot}$. We concluded that while it demonstrated that nature produces BBHs that merge in a Hubble time, it was impossible to determine the formation channel for that event. Possible BBH formation channels include dynamical formation in a dense stellar environment [e.g., 146–150] or isolated binary evolution, either the classical variant via a common-envelope phase [e.g., 151–156], possibly from population III binaries [157, 158], or chemically homogeneous evolution in close tidally locked binaries [159, 160]. Both of these channels have been shown to be consistent with the GW150914 discovery [161–166].

GW151226 differs from GW150914 primarily in the significantly lower inferred companion masses: $m_1 = 14.2^{+8.3}_{-3.7} M_{\odot}$ and $m_2 = 7.5^{+2.3}_{-2.3} M_{\odot}$. These masses are similar to the black hole masses measured dynamically in X-ray binaries (for reviews see [82, 141]). If LVT151012 is of astrophysical origin, its inferred companion masses $m_1 = 23^{+18}_{-6} M_{\odot}$ and $m_2 = 13^{+4}_{-5} M_{\odot}$ fall between those of GW150914 and GW151226. This indicates that merging BBHs exist in a broad mass range.

GW151226 and LVT151012 could have formed from lower mass progenitor stars than GW150914 and/or in higher-metallicity environments in which progenitors lose a greater fraction of their mass to winds. Black holes with such masses can be formed at solar metallicity, e.g. [167]. The low masses of GW151226 are probably inconsistent with the chemically homogeneous evolution scenario, under which higher masses are thought to be required [159, 160]. However, the masses are still consistent with both classical isolated binary evolution and dynamical formation.

The broad power-law index range $\alpha = 2.5^{+1.5}_{-1.6}$ inferred from the fit to the merging binary black hole mass distribution attempted in Section VI demonstrates the statistical uncertainty associated with extrapolating a distribution from just three events. There are additional systematic uncertainties associated with the power-law model. In particular, while population-synthesis models of binary evolution can be consistent with power-law mass distributions over a range of masses, as in figures 8 and 9 of [168], the power law is likely to be broken over the very broad range between $M_{\min} = 5 M_{\odot}$

and a total mass of $100 M_{\odot}$. Other formation models may not be consistent with power-law distributions altogether [e.g., 169]. Similar methods have been employed to fit the population of black holes with dynamical mass measurements in X-ray binaries: Ref. [141] obtained, for a power law model, $M_{\min} \sim 5$ and power law slopes in the range $1.8 \lesssim \alpha \lesssim 5.0$ without accounting for possible selection effects.

Isolated binary evolution is thought to prefer comparable masses, with mass ratios $q < 0.5$ unlikely for the classical scenario [170] and implausible for chemically homogeneous evolution [164]. The dynamical formation channel also prefers comparable masses, but allows for more extreme mass ratios; observations of merging binary black holes with extreme mass ratios could therefore point to their dynamical origin. However, the mass ratios of GW151226, $q \geq 0.28$, and LVT151012, $q \geq 0.24$, are not well determined, and $q = 1$ cannot be ruled out for either event. Similarly, spin measurements, which point to a moderate degree of net spin alignment with the orbital angular momentum for GW151226, $\chi_{\text{eff}} = 0.21^{+0.20}_{-0.10}$, cannot be used to distinguish formation channels. On the other hand, a zero effective spin is ruled out for GW151226, so at least one of the merging black holes must have been spinning; the data indicate that at least one of the merging black holes must have been spinning with $a > 0.2$ at the 99% credible level.

The inferred GW151226 merger luminosity distance of $D_L = 440^{+180}_{-190}$ Mpc, corresponding to a merger redshift of $z = 0.09^{+0.03}_{-0.04}$, is similar to that of GW150914; in contrast, LVT151012 merged about a factor of two further away, at $D_L = 1000^{+500}_{-500}$ Mpc, or $z = 0.20^{+0.09}_{-0.09}$. Both are consistent with either a relatively recent formation followed by a prompt merger, or formation in the early Universe with a significant time delay between formation and merger.

The BBH merger rate inferred from the full analysis of all O1 triggers, $R = 9\text{--}240 \text{ Gpc}^{-3} \text{ yr}^{-1}$, is consistent with the rate inferred from the first 16 days of the O1 run [42]. The full O1 merger rate can be used to update the estimate of the energy density Ω_{gw} in the stochastic gravitational-wave background from unresolvable BBH mergers, improving on early results in [171]. Using the event-based, log-flat, and power-law mass distributions presented in Section VI and the corresponding combined rates in Table III, and employing the other ‘‘Fiducial’’ model assumptions from [171], we obtain 90% credible intervals on Ω_{gw} . The three models agree at frequencies below 100 Hz where $\Omega_{\text{gw}}(f) \sim f^{2/3}$ and which contain more than 99% of the signal-to-noise ratio for stochastic backgrounds, with $\Omega_{\text{gw}}(f = 25 \text{ Hz}) \sim 1.2^{+1.9}_{-0.9} \times 10^{-9}$. These predictions do not significantly change the median value of Ω_{gw} from [171] while slightly decreasing the range; we still conclude that this background is potentially measurable by the Advanced LIGO/Virgo detectors operating at their projected design sensitivity.

Despite the uncertainty in the merger rate, its lower limit can be used to rule out some corners of the parameter space if a single formation channel is assumed for all BBHs. For example, if all merging BBHs arise from dynamical formation in globular clusters, then the lower limit on the merger rate disfavors low-mass clusters [150]. On the other hand, if all

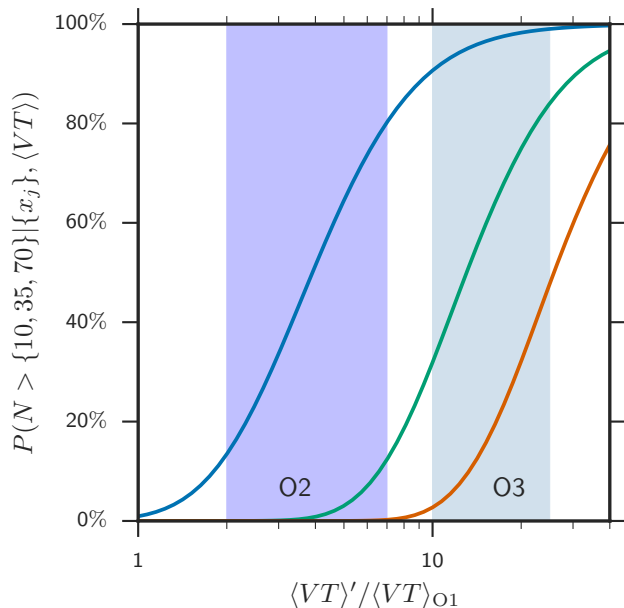


FIG. 12. The probability of observing $N > 10$, $N > 35$, and $N > 70$ highly significant events, as a function of surveyed time-volume. The vertical line and bands show, from left to right, the expected sensitive time-volume for the second (O2) and third (O3) advanced detector observing runs.

merging BBHs arise from isolated binaries evolving via the common-envelope phase, the lower limit on the merger rate disfavors a combination of very low common envelope binding energy with a high efficiency of common envelope ejection [170] (high values of $\alpha \times \lambda$, as defined in [172–174]), or very high black hole natal kicks of several hundred km/s [175]. However, since population synthesis studies have typically varied one parameter at a time, individual parameter values cannot be ruled out until the full parameter space is explored [e.g., 176].

It is likely, however, that multiple formation channels are in operation simultaneously, and GW150914, LVT151012, and GW151226 could have been formed through different channels or in different environments. A lower limit on the merger rate cannot be used to rule out evolutionary parameters if multiple channels contribute. Future observations will be required to test whether binaries can be classified into distinct clusters arising from different formation channels [177], or to compare the population to specific evolutionary models [178–181]. Such observations will make it possible to further probe the underlying mass distribution of merging BBHs and the dependence of the merger rate on redshift. Meanwhile, space-borne detectors such as eLISA could observe heavy BBHs several years before merger; multi-spectrum observations with ground-based and space-borne observatories would aid in measuring binary parameters, including location, and determining the formation channel by measuring the eccentricity at lower frequencies [182–184].

We can use the inferred rates to estimate the number of

BBH mergers expected in future observing runs. We make use of the future observing plans laid out in [128] to predict the expected rate of signals in the second and third advanced LIGO and Virgo observing runs. To do so, we restrict attention to those signals which will be observed with a false alarm rate smaller than 1/100yr. In the simulations used to estimate sensitive time-volumes, 61% of the events above the low threshold used in the PyCBC rates calculation are found with a search false alarm rate lower than one per century. The expected number of observed events will then scale linearly with the sensitive time-volume $\langle VT \rangle$ of a future search. The improvement in sensitivity in future runs will vary across the frequency band of the detectors and will therefore have a different impact for binaries of different mass. For concreteness, we use a fiducial BBH system with total mass $60M_{\odot}$ and mass ratio $q = 1$ [145], to estimate a range of sensitive time-volumes for future observing runs. The second observing run (O2) is anticipated to begin in late 2016 and last six months, and the third run (O3) to begin in 2017 and last nine months. We show the predictions for the probability of obtaining N or more high-significance events as a function of $\langle VT \rangle$ (in units of the time-volume surveyed during O1) in Fig. 12. Current projections for O2 suggest that the sensitivity will be consistent with the lower end of the band indicated in Figure 12.

VIII. CONCLUSION

During its first observing run Advanced LIGO has observed gravitational waves from the coalescence of two stellar-mass BBHs GW150914 and GW151226 with a third candidate LVT151012 also likely to be a BBH system. Our modeled binary coalescence search detects both GW150914 and GW151226 with a significance of greater than 5.3σ , while LVT151012 is found with a significance 1.7σ . The component masses of these systems span a range from the heaviest black hole in GW150914 with a mass of $36.2^{+5.2}_{-3.8}M_{\odot}$, to $7.5^{+2.3}_{-2.3}M_{\odot}$, the lightest black hole of GW151226. The spins of the individual coalescing black holes are weakly constrained, but we can rule out two non-spinning components for GW151226 at 99% credible level. All our observations are consistent with the predictions of general relativity, and the final black holes formed after merger are all predicted to have high spin values with masses that are larger than any black hole measured in x-ray binaries. The inferred rate of BBH mergers based on our observations is $9\text{--}240\text{Gpc}^{-3}\text{yr}^{-1}$ which gives confidence that future observing runs will observe many more BBHs.

ACKNOWLEDGMENTS

The authors gratefully acknowledge the support of the United States National Science Foundation (NSF) for the construction and operation of the LIGO Laboratory and Advanced LIGO as well as the Science and Technology Facilities Council (STFC) of the United Kingdom, the Max-Planck-Society (MPS), and the State of Niedersachsen/Germany for support

of the construction of Advanced LIGO and construction and operation of the GEO600 detector. Additional support for Advanced LIGO was provided by the Australian Research Council. The authors gratefully acknowledge the Italian Istituto Nazionale di Fisica Nucleare (INFN), the French Centre National de la Recherche Scientifique (CNRS) and the Foundation for Fundamental Research on Matter supported by the Netherlands Organisation for Scientific Research, for the construction and operation of the Virgo detector and the creation and support of the EGO consortium. The authors also gratefully acknowledge research support from these agencies as well as by the Council of Scientific and Industrial Research of India, Department of Science and Technology, India, Science & Engineering Research Board (SERB), India, Ministry of Human Resource Development, India, the Spanish Ministerio de Economía y Competitividad, the Conselleria d'Economia i Competitivitat and Conselleria d'Educació, Cultura i Universitats of the Govern de les Illes Balears, the National Science Centre of Poland, the European Commission, the Royal Society, the Scottish Funding Council, the Scottish Universities Physics Alliance, the Hungarian Scientific Research Fund (OTKA), the Lyon Institute of Origins (LIO), the National Research Foundation of Korea, Industry Canada and the Province of Ontario through the Ministry of Economic Development and Innovation, the Natural Science and Engineering Research Council Canada, Canadian Institute for Advanced Research, the Brazilian Ministry of Science, Technology, and Innovation, Fundação de Amparo à Pesquisa do Estado de São Paulo (FAPESP), Russian Foundation for Basic Research, the Leverhulme Trust, the Research Corporation, Ministry of Science and Technology (MOST), Taiwan and the Kavli Foundation. The authors gratefully acknowledge the support of the NSF, STFC, MPS, INFN, CNRS and the State of Niedersachsen/Germany for provision of computational resources.

Appendix A: Search Description

In this appendix we give further details of the two analyses, PyCBC and GstLAL used in the search. Both analyses separately correlate the data from each detector with template waveforms that model the expected signal. The analyses identify candidate events that are detected at both the Hanford and Livingston observatories consistent with the 10 ms inter-site propagation time. Additional signal consistency tests are performed to mitigate the effects of non-stationary transients in the data. Events are assigned a detection-statistic value that ranks their likelihood of being a gravitational-wave signal. This detection statistic is compared to the estimated detector noise background to determine, for each candidate event, the probability that detector noise would give rise to at least one equally significant event.

The choice of parameters for the templates depends on the shape of the power spectrum of the detector noise. The average noise power spectral density of the LIGO detectors was measured over the period September 12 to September 26, 2015. The harmonic mean of these noise spectra from the two detectors was used to place a single template bank that

was used for the duration of the search [3].

The matched filter SNR ρ for each template waveform and each detector's data as a function of time is calculated according to [11, 185]

$$\rho^2(t) \equiv [\langle s|h_c \rangle^2(t) + \langle s|h_s \rangle^2(t)], \quad (\text{A1})$$

where the correlation is defined by

$$\langle s|h \rangle(t) = 4\text{Re} \int_0^\infty \frac{\tilde{s}(f)\tilde{h}^*(f)}{S_n(f)} e^{2\pi ift} df, \quad (\text{A2})$$

h_c and h_s are the normalized orthogonal sine and cosine parts of the template and $\tilde{a}(f)$ is used to denote the Fourier transform of the time domain quantity $a(t)$. $S_n(f)$ denotes the one-sided average power spectral density of the detector noise. The waveform components h_c and h_s are normalized such that the expected value of $\langle s|h_{s,c} \rangle^2(t)$ in stationary, Gaussian noise is unity [93]. The analyses identify times when the matched filter SNR achieves a local maximum and stores them as triggers. The analyses search only stretches of data longer than a minimum duration, to ensure that the detectors are operating stably. The choice is different in the two analyses and reduces the available data of 48.6 days to 46.1 days for the PyCBC analysis and 48.3 days for the GstLAL analysis.

To suppress large SNR values caused by non-Gaussian detector noise, the analyses perform additional tests to quantify the agreement between the data and the template. These tests are different in the two analyses and are discussed in their respective subsections below. Both analyses enforce coincidence between detectors by selecting trigger pairs that occur within a 15 ms window and come from the same template. The 15 ms window is determined by the 10 ms inter-site propagation time plus 5 ms for uncertainty in determining accurately the measured arrival time of weak signals. A detection statistic for each coincident event is derived as a function of the SNR observed in each detector, the value of the signal consistency tests and details of the template.

The significance of a candidate event is determined by comparing it to the search background. From this, we are able to determine the rate at which detector noise produces events with a detection-statistic value equal to or higher than the candidate event (the FAR). Estimating this background is challenging for two reasons: the detector noise is non-stationary and non-Gaussian, therefore its properties must be empirically determined; and it is not possible to shield the detector from gravitational waves to directly measure a signal-free background. The specific procedure used to estimate the background is different for the two analyses, as described in detail below.

The results of the independent analyses are two separate lists of candidate events, with each candidate event assigned a p-value and FAR. Candidate events with low FARs are identified as possible gravitational wave signals for further investigation.

1. PyCBC Analysis

The PyCBC analysis is described in detail in [2–4], and the configuration used to analyze the first 16 days of O1 data, containing GW150914, is described in Ref. [43]. Following the observation of GW150914, some improvements were made to the analysis, as we better understood the Advanced LIGO data. All changes were tested and tuned only on background data, prior to being incorporated into the analysis. These changes do not affect the significance of GW150914. Consequently, we chose to present the full results, on the final calibrated data, using the improved analysis. Here, we provide a brief overview of the analysis, including details of changes made following the discovery of GW150914.

In the PyCBC analysis, a trigger is stored when the maximum of the SNR time series is above the threshold of 5.5 (chosen as a compromise between a manageable trigger rate and assurance that no real event will be missed), with a maximum of one trigger stored in a 1 second window (reduced from 4s in the previous analysis). A χ^2 statistic is computed to distinguish between astrophysical signals and noise transients. This tests whether the signal power in a number of non-overlapping frequency bands is consistent with that expected from the waveform template [14]. The χ^2 test is written explicitly as

$$\chi_r^2 = \frac{p}{2p-2} \sum_{i=1}^p \left(\rho_i - \frac{\rho}{p} \right)^2, \quad (\text{A3})$$

where p denotes the number of frequency bands—constructed such that the expected signal power in each band is equal—and ρ_i is the matched-filter SNR in the i -th frequency band. For data containing only Gaussian noise, or Gaussian noise and a signal exactly matching the template waveform, the expected value of this statistic will be 1. For data containing non-Gaussian artefacts, or a signal not matching well with the template waveform, this value will be elevated. Each trigger is then ranked according to a combination of the SNR and the χ^2 test, namely

$$\hat{\rho} = \begin{cases} \rho [(1 + (\chi_r^2)^3)/2]^{-1/6}, & \text{if } \chi_r^2 > 1, \\ \rho, & \text{if } \chi_r^2 \leq 1. \end{cases} \quad (\text{A4})$$

The number of frequency bands p used to compute the χ^2 signal-based veto [14] was optimized using data from the first month of O1. An improved background rejection was found when adopting the following, template-dependent expression for the number of χ^2 bands,

$$p = 1.75 \times \left(\frac{f_{\text{peak}}}{1 \text{ Hz}} - 60 \right)^{1/2} \quad (\text{A5})$$

where f_{peak} is the frequency corresponding to the maximum amplitude of the template waveform using the models described in Ref. [8], and p is rounded to the nearest integer. This choice was adopted for the full O1 analysis presented here where all waveforms have peak frequencies greater than 60Hz.

Loud and short instrumental transients are identified and excised from the data, as part of the data conditioning prior to SNR computation. In this analysis, we compute a whitened time series of the strain data and compare the magnitude of each sample against a threshold value of 100. Samples above threshold and within a time window of ± 0.5 s are clustered together, and a gating window is placed at the time of the loudest sample in the cluster.⁹ The threshold value of 100 is chosen to be much larger than the typical value of the magnitude in Gaussian noise and also larger than the value expected from any gravitational-wave signal from binaries at astrophysical distances and with intrinsic parameters within our search space.

Coincident triggers are formed when a trigger exists in both observatories, associated with the same template waveform and with arrival times within 15 ms. Each coincidence is ranked with a network statistic, $\hat{\rho}_c$, defined as the quadrature sum of the $\hat{\rho}$ in each observatory. The rate of background events, as a function of network statistic, is estimated from the data itself by repeating the analysis after artificially time-shifting the triggers from one detector relative to the other. Time shifts in multiples of 100 ms are performed, leading to a total of $T_b = 5.0 \times 10^6$ years of background time analyzed.

The distribution of background noise events over $\hat{\rho}_c$ can vary strongly as a function of the template waveform; to account for this variation, the parameter space is divided into a number of regions which are treated as independent searches [43]. Each coincident trigger is assigned a FAR based on the background distribution in the region containing the coincidence and incorporating a trials factor equal to the number of regions. Studies of the background distribution as a function of the template parameters, and a reduced rate of noise events in O1 data, compared to the engineering run data previously used in tuning the search configuration [187], motivated a re-definition of the regions used to divide the search space. In the current analysis, we split the parameter space into three regions, defined by: (i) $\mathcal{M} < 1.74 M_\odot$; (ii) $\mathcal{M} \geq 1.74 M_\odot$ and $f_{\text{peak}} \geq 100$ Hz; (iii) $\mathcal{M} \geq 1.74 M_\odot$ and $f_{\text{peak}} < 100$ Hz. In the GW150914 analysis, the boundary between regions (ii) and (iii) was set at 220 Hz. By reducing this frequency, we significantly reduce the number of templates assigned to region (iii), which is dominated by short templates that are most affected by noise transients.

2. GstLAL Analysis

The GstLAL [188] analysis method is a low-latency, multi-detector matched filtering search for gravitational waves emitted by the coalescence of compact objects. The analysis exploits time-domain operations [5] that give it latency of seconds after the acquisition of gravitational-wave data. This allows the GstLAL analysis to run in both low latency mode to

⁹ In the GW150914 analysis a transient detection pipeline based on a time-frequency decomposition of the data via sine-Gaussian basis functions was used to identify times to be excised [186].

provide rapid identification of signals and in offline mode on data that have been conditioned with data quality vetoes [13]. The results presented here are for the offline mode. No changes were made to the GstLAL analysis relative to the results presented in [43].

For the offline analysis, the data $s(t)$ are partitioned into chunks and, along with the templates $h(t)$, the data $s(t)$ are then whitened in the frequency domain. The analysis splits the template bank into sub-banks containing waveforms that have morphological similarities. The templates are binned in a two-dimensional space by effective spin parameter χ_{eff} and chirp mass \mathcal{M} , as these parameters can be used to effectively describe a binary system in which the spins are aligned with the binary's orbital angular momentum. Templates are allowed to overlap in adjacent bins to mitigate boundary effects, although no redundant waveforms are filtered.

An orthonormal basis of filters $\hat{h}(t)$ are then constructed using singular value decomposition [5]. This basis is significantly smaller than the number of input waveforms and allows for a significant reduction in the time-domain filtering cost. The set of filters $\hat{h}(t)$ in each bin are convolved with the whitened data, producing a time series; the matched-filter SNR time series ρ for each template can then be constructed using linear combinations of the convolution time series. A trigger is stored when the maximum of the SNR time series crosses a predetermined threshold of 4. A maximum of one coincident trigger per template is stored in each second.

A signal consistency test is performed by comparing the SNR time series of data to the SNR time series *expected* from a real signal using the autocorrelation function of the template at its time of peak amplitude, $R(t)$. A consistency test value ξ_{ac}^2 is determined for each trigger using the SNR time series $\rho(t)$, the peak SNR ρ_p , and the autocorrelation function $R(t)$ in some window of time δt (corresponding to ρ_p) around the trigger:

$$\xi_{\text{ac}}^2 = \frac{1}{\mu} \int_{t_p - \delta t}^{t_p + \delta t} dt |\rho(t) - \rho_p R(t)|^2. \quad (\text{A6})$$

where the factor μ ensures that a well-fit signal has an expectation value of one [43]. The window δt is a tuneable parameter that has been chosen based on Monte Carlo simulations in real data and finding the value that (on average) best rejected glitches.

Triggers that survive consistency checks are assigned a ranking based upon their SNR, ξ_{ac}^2 value, and the instantaneous horizon distance values at each detector, $\{D_{\text{H1}}, D_{\text{L1}}\}$, which encode the detector sensitivity [15, 189].

A likelihood ratio is constructed to rank candidate events by the ratio of the probability of observing matched-filter SNR and ξ^2 from signals, \mathbf{h} , versus obtaining the same parameters from noise, \mathbf{n} . The templates have already been grouped into regions that contain high overlap, so it is likely that templates within each group will respond similarly to noise; in fact the template group itself is used as a parameter in the likelihood ratio to qualitatively establish how different regions of the parameter space are affected by noise. The likelihood ratio can

thus be written as

$$\mathcal{L} = \frac{p(\mathbf{x}_{\text{H}}, \mathbf{x}_{\text{L}}, D_{\text{H}}, D_{\text{L}} | \theta_i, \mathbf{h})}{p(\mathbf{x}_{\text{H}} | \theta_i, \mathbf{n}) p(\mathbf{x}_{\text{L}} | \theta_i, \mathbf{n})}, \quad (\text{A7})$$

where $\mathbf{x}_d = \{\rho_d, \xi_d^2\}$ are the matched-filter SNR and ξ^2 in each detector, θ_i corresponds to the template group, and D_d is the horizon distance of the given detector at the time of the trigger. The signal distribution in the numerator is calculated using an astrophysical model of signals distributed isotropically in the nearby universe. The denominator is calculated under the assumption that the noise in each detector is independent. It can then be calculated from the distribution of triggers in each template bin observed in each detector. In the case that multiple high-likelihood events are produced at the same time, a clustering process is used to remove events with lower likelihoods within a 4 second window so that only the event with the highest likelihood is retained.

In a typical search, the majority of events found in coincidence correspond to noise and not an actual signal. To accurately distill signals from the data, the false-alarm probability at the value of \mathcal{L} for each event is ascertained; the false-alarm probability describes the probability of observing the event's \mathcal{L} or greater in noise alone. The GstLAL method determines the false-alarm probability by taking the probability density functions of parameters in Eq. A7 obtained from triggers that are noise-like in nature [190].

Appendix B: Parameter Estimation Description

To extract information from the signal, we perform a coherent Bayesian analysis of the data from the two instruments using `LALInference` [45].¹⁰ The properties of the source leave imprints on the signal from which we can infer their values [38]. We match the measured strain to model waveforms and use the agreement to define probability distributions for the parameters which describe the signal. A summary of results for the three events is given in Table IV.

The result of our analysis is the posterior probability distribution for parameters describing the source. The posterior is computed from Bayes' theorem [191, 192]: it is proportional to the product of the likelihood of the data given the parameters and the prior for the parameters. The likelihood is calculated using a noise-weighted inner product between the data and the model waveform [93]. This depends upon the waveform and the noise spectral density at the time of event, and both could potentially be sources of systematic error. We incorporate the effects of uncertainty in the detectors' calibration using a frequency-dependent model [193]. The posterior probability density is mapped out using stochastic sampling algorithms, and our parameter estimates are constructed from the distribution of samples.

¹⁰ The `LALInference` package of the LIGO Algorithm Library (LAL) software suite available from <https://wiki.ligo.org/DASWG/LALSuite>.

The analysis makes use of two inspiral–merger–ringdown waveform models, a reduced-order model of the double aligned spin EOB waveform used for the detection analyses, which we refer to as EOBNR [8, 9], and an effective precessing spin model, which we refer to as IMRPhenom [35–37]. An analysis using a fully precessing EOBNR waveform [194], as done in [39], will be reported in the future; this is currently too computationally expensive for results to be presented now.¹¹ For all events, the results from the EOBNR and IMRPhenom waveforms are similar.

To compare how well the different waveform models match the data, we use the Bayes factor $\mathcal{B}_{s/n}$ and the deviance information criterion (DIC). The Bayes factor is the ratio of the evidence (the marginalised likelihood) for a coherent signal hypothesis to that for Gaussian noise [195]. A larger Bayes factor indicates that there is more support for the signal model [196]. The DIC is a measure of the goodness-of-fit of a model, defined as an average log-likelihood plus a penalty factor for higher dimensional models [197–199]. A smaller value of the DIC indicates a greater expectation that the model would predict data similar to that being analysed, and hence that it is a better fit. The values for both quantities are similar for all three events. The data do not allow us to conclusively prefer one waveform model over the other; therefore, in the column titled Overall, results are constructed by averaging the two, marginalizing over our choice of waveform.

Inaccuracies in the waveform models could be a source of systematic error in the parameter estimates [200–202]. However, an alternative analysis of GW150914 using a set of waveforms from numerical-relativity simulations yielded results consistent with those using the EOBNR and IMRPhenom approximants [203]. For our results, we use the difference between results from the two waveform models as a proxy for the theoretical error from waveform modelling, although some known physics such as higher modes and eccentricity are missing from both these waveform families. For each parameter, we quote systematic errors on the boundaries of the 90% credible intervals; these are the 90% range of a normal distribution estimated from the variance of results from the different models [38]. For parameters with bounded ranges, like the spins or mass ratio, the normal distributions should be truncated, but for simplicity, we still quote the 90% range of the uncut distributions. More sophisticated means of incorporating waveform uncertainty in to the analysis, such as Gaussian process regression [204], may be used in the future. For all three events, we find that the theoretical uncertainty from waveform modelling is less significant than statistical uncertainty from the finite SNR of the events.

The calibration error is modelled using a cubic spline polynomial [38, 193], and we marginalise over uncertainty in the calibration. Each analysis assumes a prior for the calibration

TABLE III. The standard deviations used for the (zero-mean) Gaussian priors on calibration uncertainty for each of the three events. The calibration of each of the two detectors has been independently assessed [47]. These priors set the expected variation for the frequency-dependent spline model used to incorporate the effects of calibration uncertainty [193].

| Event | Amplitude | | Phase | |
|-----------|-----------|------------|---------|------------|
| | Hanford | Livingston | Hanford | Livingston |
| GW150914 | 4.8% | 8.2% | 3.2 deg | 4.2 deg |
| LVT151012 | 4.2% | 8.3% | 2.7 deg | 4.3 deg |
| GW151226 | 4.2% | 6.9% | 2.7 deg | 3.6 deg |

uncertainty which is specific for each detector at the time of that signal. Standard deviations of the prior distributions for the amplitude and phase uncertainty are given in Table III. The updated calibration uncertainty is better than the original 10% in amplitude and 10 deg in phase [47] used for the first results.

Aside from the difference in calibration, the analysis of GW150914 follows the specification in [38]. We analyse 8 s of data centred on the time reported by the detection analyses [43], using the frequency range between 20 Hz and 1024 Hz. For quantities subject to change because of precession, we quote values at a reference GW frequency of $f_{\text{ref}} = 20$ Hz. We assume uninformative prior distributions for the parameters (uniform distributions for the time and phase of coalescence, uniform distribution of sources in volume, isotropic orientations for the binary and the two spins, uniform distribution of spin magnitudes, and uniform distribution of component masses $m_{1,2} \in [10, 80] M_{\odot}$). There are small differences in the source’s parameters compared to the runs on the older calibration, but these are well within the total uncertainty; the greatest difference is in the sky area, where the reduced calibration uncertainty improves the localization area by a factor of ~ 2 –3.

There are two differences in the configuration of the analysis of LVT151012 from that for GW150914: the prior on the component masses was set to be uniform over the range $m_{1,2} \in [5, 80] M_{\odot}$, and the length of data analysed was $T = 22$ s. We find that LVT151012 is consistent with a lower mass source, which necessitates a lower prior bound on the component masses and requires us to analyse a longer stretch since the signal is in-band for longer.

GW151226 is also consistent with being a lower mass source. However, we can still consider just 8 s of data by confining the component masses such that the chirp mass is $\mathcal{M} \in [9.5, 10.5] M_{\odot}$ and the mass ratio is $q \in [1/18, 1]$. Preliminary analyses found no support outside of these ranges and the final posteriors lie safely within this region. This choice of segment length limits the computational expense of the analysis.

¹¹ In LAL and in some technical publications, the aligned spin EOB model and its reduced-order model are called `SEOBNRv2` and `SEOBNRv2_ROM_DoubleSpin` respectively, the fully precessing EOB model is called `SEOBNRv2`, and the precessing IMRPhenom model is called `IMRPhenomPv2`.

TABLE IV. Parameters that characterise GW150914, GW151226 and LVT151012. For model parameters we report the median value with the range of the symmetric 90% credible interval [205]; we also quote selected 90% credible bounds. For the logarithm of the Bayes factor for a signal compared to Gaussian noise we report the mean and its 90% standard error from 4 parallel runs with a nested sampling algorithm [195], and for the deviance information criterion we report the mean and its 90% standard error from a Markov-chain Monte Carlo and a nested sampling run. The source redshift and source-frame masses assume standard cosmology [40]. Results are given for spin-aligned EOBNR and precessing IMRPhenom waveform models. The Overall results are computed by averaging the posteriors for the two models. For the Overall results we quote both the 90% credible interval or bound and an estimate for the 90% range of systematic error on this determined from the variance between waveform models. Further explanation of the parameters are given in [38].

| | GW150914 | | | GW151226 | | | LVT151012 | | |
|--|---------------------------|---------------------------|---|---------------------------|---------------------------|---|---------------------------|---------------------------|---|
| | EOBNR | IMRPhenom | Overall | EOBNR | IMRPhenom | Overall | EOBNR | IMRPhenom | Overall |
| Detector frame | | | | | | | | | |
| Total mass M/M_\odot | $71.0^{+4.6}_{-4.0}$ | $71.2^{+3.5}_{-3.2}$ | $71.1^{+4.1\pm 0.7}_{-3.6\pm 0.8}$ | $23.6^{+8.0}_{-1.3}$ | $23.8^{+5.1}_{-1.5}$ | $23.7^{+6.5\pm 2.2}_{-1.4\pm 0.1}$ | 45^{+17}_{-4} | 44^{+12}_{-3} | $44^{+16\pm 5}_{-3\pm 0}$ |
| Chirp mass \mathcal{M}/M_\odot | $30.4^{+2.3}_{-1.6}$ | $30.7^{+1.5}_{-1.5}$ | $30.6^{+1.9\pm 0.3}_{-1.6\pm 0.4}$ | $9.71^{+0.08}_{-0.07}$ | $9.72^{+0.06}_{-0.06}$ | $9.72^{+0.07\pm 0.01}_{-0.06\pm 0.01}$ | $18.1^{+1.3}_{-0.9}$ | $18.1^{+0.8}_{-0.8}$ | $18.1^{+1.0\pm 0.5}_{-0.8\pm 0.1}$ |
| Primary mass m_1/M_\odot | $40.2^{+5.2}_{-4.8}$ | $38.5^{+5.4}_{-3.3}$ | $39.4^{+5.4\pm 1.3}_{-4.1\pm 0.2}$ | $15.3^{+10.8}_{-3.8}$ | $15.8^{+7.2}_{-4.0}$ | $15.6^{+9.0\pm 2.6}_{-4.0\pm 0.2}$ | 29^{+23}_{-8} | 27^{+19}_{-6} | $28^{+21\pm 5}_{-7\pm 0}$ |
| Secondary mass m_2/M_\odot | $30.6^{+5.1}_{-4.2}$ | $32.7^{+3.1}_{-4.9}$ | $31.7^{+4.0\pm 0.1}_{-4.9\pm 1.2}$ | $8.3^{+2.5}_{-2.9}$ | $8.1^{+2.5}_{-2.1}$ | $8.2^{+2.6\pm 0.2}_{-2.5\pm 0.5}$ | 15^{+5}_{-6} | 16^{+4}_{-6} | $16^{+5\pm 0}_{-6\pm 1}$ |
| Final mass M_f/M_\odot | $67.8^{+4.0}_{-3.6}$ | $67.9^{+3.2}_{-2.9}$ | $67.8^{+3.7\pm 0.6}_{-3.3\pm 0.7}$ | $22.5^{+8.2}_{-1.4}$ | $22.8^{+5.3}_{-1.6}$ | $22.6^{+6.7\pm 2.2}_{-1.5\pm 0.1}$ | 43^{+17}_{-4} | 42^{+13}_{-2} | $42^{+16\pm 5}_{-3\pm 0}$ |
| Source frame | | | | | | | | | |
| Total mass $M^{\text{source}}/M_\odot$ | $65.5^{+4.4}_{-3.9}$ | $65.1^{+3.6}_{-3.1}$ | $65.3^{+4.1\pm 1.0}_{-3.4\pm 0.3}$ | $21.6^{+7.4}_{-1.6}$ | $21.9^{+4.7}_{-1.7}$ | $21.8^{+5.9\pm 2.0}_{-1.7\pm 0.1}$ | 38^{+15}_{-5} | 37^{+11}_{-4} | $37^{+13\pm 4}_{-4\pm 0}$ |
| Chirp mass $\mathcal{M}^{\text{source}}/M_\odot$ | $28.1^{+2.1}_{-1.6}$ | $28.1^{+1.6}_{-1.4}$ | $28.1^{+1.8\pm 0.4}_{-1.5\pm 0.2}$ | $8.87^{+0.35}_{-0.28}$ | $8.90^{+0.31}_{-0.27}$ | $8.88^{+0.33\pm 0.01}_{-0.28\pm 0.04}$ | $15.2^{+1.5}_{-1.1}$ | $15.0^{+1.3}_{-1.0}$ | $15.1^{+1.4\pm 0.3}_{-1.1\pm 0.0}$ |
| Primary mass $m_1^{\text{source}}/M_\odot$ | $37.0^{+4.9}_{-4.4}$ | $35.3^{+5.1}_{-3.1}$ | $36.2^{+5.2\pm 1.4}_{-3.8\pm 0.4}$ | $14.0^{+10.0}_{-3.5}$ | $14.5^{+6.6}_{-3.7}$ | $14.2^{+8.3\pm 2.4}_{-3.7\pm 0.2}$ | 24^{+19}_{-5} | 23^{+16}_{-5} | $23^{+18\pm 5}_{-6\pm 0}$ |
| Secondary mass $m_2^{\text{source}}/M_\odot$ | $28.3^{+4.6}_{-3.9}$ | $29.9^{+3.0}_{-4.5}$ | $29.1^{+3.7\pm 0.0}_{-4.4\pm 0.9}$ | $7.5^{+2.3}_{-2.6}$ | $7.4^{+2.3}_{-2.0}$ | $7.5^{+2.3\pm 0.2}_{-2.3\pm 0.4}$ | 13^{+4}_{-5} | 14^{+4}_{-5} | $13^{+4\pm 0}_{-5\pm 0}$ |
| Final mass $M_f^{\text{source}}/M_\odot$ | $62.5^{+3.9}_{-3.5}$ | $62.1^{+3.3}_{-2.8}$ | $62.3^{+3.7\pm 0.9}_{-3.1\pm 0.2}$ | $20.6^{+7.6}_{-1.6}$ | $20.9^{+4.8}_{-1.8}$ | $20.8^{+6.1\pm 2.0}_{-1.7\pm 0.1}$ | 36^{+15}_{-4} | 35^{+11}_{-3} | $35^{+14\pm 4}_{-4\pm 0}$ |
| Energy radiated $E_{\text{rad}}/(M_\odot c^2)$ | $2.98^{+0.55}_{-0.40}$ | $3.02^{+0.36}_{-0.36}$ | $3.00^{+0.47\pm 0.13}_{-0.39\pm 0.07}$ | $1.02^{+0.09}_{-0.24}$ | $0.99^{+0.11}_{-0.17}$ | $1.00^{+0.10\pm 0.01}_{-0.20\pm 0.03}$ | $1.48^{+0.39}_{-0.41}$ | $1.51^{+0.29}_{-0.44}$ | $1.50^{+0.33\pm 0.05}_{-0.43\pm 0.01}$ |
| Mass ratio q | $0.77^{+0.20}_{-0.18}$ | $0.85^{+0.13}_{-0.21}$ | $0.81^{+0.17\pm 0.02}_{-0.20\pm 0.04}$ | $0.54^{+0.40}_{-0.33}$ | $0.51^{+0.39}_{-0.25}$ | $0.52^{+0.40\pm 0.03}_{-0.29\pm 0.04}$ | $0.53^{+0.42}_{-0.34}$ | $0.60^{+0.35}_{-0.37}$ | $0.57^{+0.38\pm 0.01}_{-0.37\pm 0.04}$ |
| Effective inspiral spin χ_{eff} | $-0.08^{+0.17}_{-0.14}$ | $-0.05^{+0.11}_{-0.12}$ | $-0.06^{+0.14\pm 0.02}_{-0.14\pm 0.04}$ | $0.21^{+0.24}_{-0.11}$ | $0.22^{+0.15}_{-0.18}$ | $0.21^{+0.20\pm 0.07}_{-0.10\pm 0.03}$ | $0.06^{+0.31}_{-0.24}$ | $0.01^{+0.26}_{-0.17}$ | $0.03^{+0.31\pm 0.08}_{-0.20\pm 0.02}$ |
| Primary spin magnitude a_1 | $0.33^{+0.39}_{-0.29}$ | $0.30^{+0.54}_{-0.27}$ | $0.32^{+0.47\pm 0.10}_{-0.29\pm 0.01}$ | $0.42^{+0.35}_{-0.37}$ | $0.55^{+0.35}_{-0.42}$ | $0.49^{+0.37\pm 0.11}_{-0.42\pm 0.07}$ | $0.31^{+0.46}_{-0.27}$ | $0.31^{+0.50}_{-0.28}$ | $0.31^{+0.48\pm 0.03}_{-0.28\pm 0.00}$ |
| Secondary spin magnitude a_2 | $0.62^{+0.35}_{-0.54}$ | $0.36^{+0.53}_{-0.33}$ | $0.48^{+0.47\pm 0.08}_{-0.43\pm 0.03}$ | $0.51^{+0.44}_{-0.46}$ | $0.52^{+0.42}_{-0.47}$ | $0.52^{+0.43\pm 0.01}_{-0.47\pm 0.00}$ | $0.49^{+0.45}_{-0.44}$ | $0.42^{+0.50}_{-0.38}$ | $0.45^{+0.48\pm 0.02}_{-0.41\pm 0.01}$ |
| Final spin a_f | $0.68^{+0.05}_{-0.07}$ | $0.68^{+0.06}_{-0.05}$ | $0.68^{+0.05\pm 0.01}_{-0.06\pm 0.02}$ | $0.73^{+0.05}_{-0.06}$ | $0.75^{+0.07}_{-0.05}$ | $0.74^{+0.06\pm 0.03}_{-0.06\pm 0.03}$ | $0.65^{+0.09}_{-0.10}$ | $0.66^{+0.08}_{-0.10}$ | $0.66^{+0.09\pm 0.00}_{-0.10\pm 0.02}$ |
| Luminosity distance D_L/Mpc | 400^{+160}_{-180} | 440^{+170}_{-140} | $420^{+150\pm 20}_{-180\pm 40}$ | 450^{+180}_{-210} | 440^{+170}_{-180} | $440^{+180\pm 20}_{-190\pm 10}$ | 1000^{+540}_{-490} | 1030^{+480}_{-480} | $1020^{+500\pm 20}_{-490\pm 40}$ |
| Source redshift z | $0.086^{+0.031}_{-0.036}$ | $0.094^{+0.027}_{-0.034}$ | $0.090^{+0.029\pm 0.003}_{-0.036\pm 0.008}$ | $0.096^{+0.035}_{-0.042}$ | $0.092^{+0.033}_{-0.037}$ | $0.094^{+0.035\pm 0.004}_{-0.039\pm 0.001}$ | $0.198^{+0.091}_{-0.092}$ | $0.204^{+0.082}_{-0.088}$ | $0.201^{+0.086\pm 0.003}_{-0.091\pm 0.008}$ |
| Upper bound | | | | | | | | | |
| Primary spin magnitude a_1 | 0.62 | 0.73 | 0.67 ± 0.09 | 0.68 | 0.83 | 0.77 ± 0.12 | 0.64 | 0.69 | 0.67 ± 0.04 |
| Secondary spin magnitude a_2 | 0.93 | 0.80 | 0.90 ± 0.12 | 0.90 | 0.89 | 0.90 ± 0.01 | 0.89 | 0.85 | 0.87 ± 0.04 |
| Lower bound | | | | | | | | | |
| Mass ratio q | 0.62 | 0.68 | 0.65 ± 0.05 | 0.25 | 0.30 | 0.28 ± 0.04 | 0.22 | 0.28 | 0.24 ± 0.05 |
| Log Bayes factor $\ln \mathcal{B}_s/n$ | 287.7 ± 0.1 | 289.8 ± 0.3 | — | 59.5 ± 0.1 | 60.2 ± 0.2 | — | 22.8 ± 0.2 | 23.0 ± 0.1 | — |
| Information criterion DIC | 32977.2 ± 0.3 | 32973.1 ± 0.1 | — | 34296.4 ± 0.2 | 34295.1 ± 0.1 | — | 94695.8 ± 0.0 | 94692.9 ± 0.0 | — |

Appendix C: Rates Calculation Description

The framework of [206] considers two classes of triggers (coincident search events): those whose origin is astrophysical and those whose origin is terrestrial. Terrestrial triggers are the result of either instrumental or environmental effects in the detector. In order to calculate the rate of astrophysical triggers, we first seek to determine the probability that any given trigger arises from either class. The two classes of source produce triggers with different densities as a function of the detection statistic used in the analysis, which we denote as x . Triggers appear in a Poisson process with number density

$$\frac{dN}{dx} = \Lambda_1 p_1(x) + \Lambda_0 p_0(x), \quad (\text{C1})$$

where Λ_1 and Λ_0 are the Poisson mean numbers of triggers of astrophysical and terrestrial origin, respectively. Λ_1 is related to the merger rate density through

$$\Lambda_1 = R \langle VT \rangle, \quad (\text{C2})$$

where $\langle VT \rangle$ is the population-averaged sensitive space-time volume of the search [42]

$$\langle VT \rangle = T \int dz d\theta \frac{dV_c}{dz} \frac{1}{1+z} s(\theta) f(z, \theta), \quad (\text{C3})$$

where V_c is the comoving volume [207], θ describes the population parameters, $s(\theta)$ is the distribution function for the astrophysical population in question, and $0 \leq f(z, \theta) \leq 1$ is the selection function giving the probability of detecting a source with parameters θ at redshift z . Because the distribution of astrophysical triggers is independent of source parameters without parameter estimation (PE) followup we must *assume* an astrophysical distribution of sources and the rate enters the likelihood only in the form $\Lambda_1 = R \langle VT \rangle$. We also marginalize over a calibration uncertainty of 6% on the recovered luminosity distances (18% uncertainty on $\langle VT \rangle$) when computing the rates.

The distribution of terrestrial triggers is calculated from the search background estimated by the analyses (as shown in Fig. 3). The distribution of astrophysical events is determined by performing large-scale simulations of signals drawn from the various astrophysical populations added to the O1 data set and using the distribution of triggers recovered by our detection analyses applied to this data set. This method correctly accounts for various thresholds applied in the analyses. Note that the observed distribution of astrophysical triggers over the detection statistic will be essentially independent of the astrophysical population used: all populations are assumed to be distributed uniformly in co-moving volume, thus to a good approximation the measured SNRs and other detection statistics follow the flat space, volumetric density [125] $p_1(\rho) \propto \rho^{-4}$.

The likelihood for a search result containing M triggers with detection statistic values $\{x_j | j = 1, \dots, M\}$ is [206]

$$\begin{aligned} \mathcal{L}(\{x_j | j = 1, \dots, M\} | \Lambda_1, \Lambda_0) \\ = \left\{ \prod_{j=1}^M [\Lambda_1 p_1(x_j) + \Lambda_0 p_0(x_j)] \right\} \exp[-\Lambda_1 - \Lambda_0]. \quad (\text{C4}) \end{aligned}$$

The posterior over Λ_1 and Λ_0 is then obtained by multiplying the likelihood in Eq. (C4) by a Jeffreys prior and marginalizing over the x_j to obtain $p(\Lambda_0, \Lambda_1)$. For a trigger with statistic value x , the probability that it is of astrophysical origin is

$$\begin{aligned} P_1(x | \{x_j | j = 1, \dots, M\}) \equiv \int d\Lambda_0 d\Lambda_1 \frac{\Lambda_1 p_1(x)}{\Lambda_0 p_0(x) + \Lambda_1 p_1(x)} \\ \times p(\Lambda_1, \Lambda_0 | \{x_j | j = 1, \dots, M\}). \quad (\text{C5}) \end{aligned}$$

Finally, we evaluate the rate assuming a population containing only BBH mergers with mass and spin parameters matching the three triggers for which $P_1 > 0.5$, i.e. astrophysical origin is more likely than terrestrial. To do so, we must generalise the formalism presented above to account for three different astrophysical populations, each having a different mean number of triggers Λ_i . The distributions of detection statistic values $p_i(x)$ are identical across the different signal populations, as discussed above. Then the likelihood of Eq. (C4) is generalized to allow for each trigger to arise from one of the astrophysical classes, or be of terrestrial origin. In this case, we also change the prior distribution to account for the number of astrophysical trigger classes via

$$p(\{\Lambda_i\}, \Lambda_0) \propto \left(\sum_i^{N_c} \Lambda_i \right)^{-N_c+1/2} \Lambda_0^{-1/2}, \quad (\text{C6})$$

where $N_c = 3$ is the number of different classes of astrophysical triggers. This functional form is chosen to prevent the posterior expectation of the total count of astrophysical events, $\sum_i^{N_c} \Lambda_i$, from growing without limit as more classes are considered in the calculation.

The three triggers associated to GW150914, GW151226 and LVT151012 are restricted to originate either from their specific class, or be of terrestrial origin. Thus, for instance, we neglect any probability of GW150914 arising from the class containing GW151226. We justify this by noting that the probability distributions for the component masses of the three likely signals are disjoint from one another at high confidence.

Multiplying this prior by the generalization of the likelihood, Eq. (C4), we obtain the posterior distribution on Λ_i , the number of astrophysical triggers in each class. We again calculate the sensitive $\langle VT \rangle$ for each of the classes of signals, and thus infer merger rates for each class. Figure 13 shows how the sensitive $\langle VT \rangle$ is accumulated as a function of redshift. For the less massive GW151226, the peak occurs at $z \sim 0.1$ while for GW150914 it occurs at $z \approx 0.2$, with the search being sensitive to some signals with redshifts as high as 0.6.

Appendix D: Mass Distribution Calculation Description

Here we describe the details of the analysis of the mass distribution that appears in Section VI. Further details on population analysis in the context of measurement uncertainty and selection effects are given in [208]. Useful references for hierarchical analysis in astronomy include [141–144].

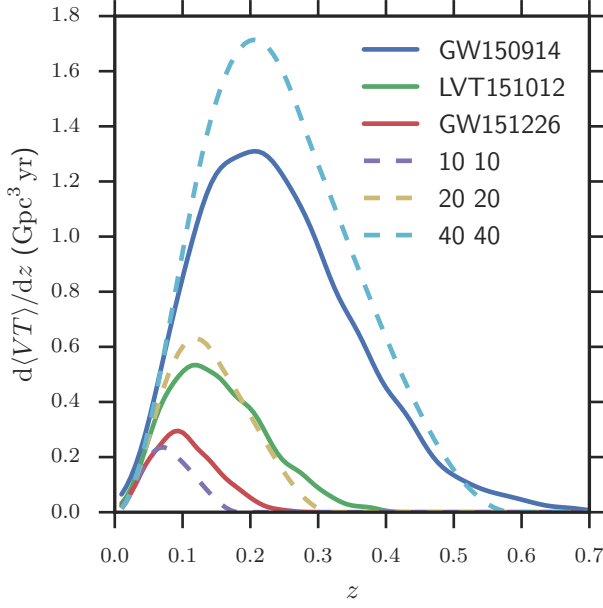


FIG. 13. The rate at which sensitive time-volume accumulates with redshift. Curves labeled by component masses in M_{\odot} are computed using an approximate prescription described in [42], assuming sources with fixed masses in the comoving frame and with zero component spins; the GW150914, GW151226 and LVT151012 curves are determined from the Monte-Carlo injection campaign described in Section VI.

We assume that the distribution of black hole masses in coalescing binaries follows (see equation 7)

$$p(m_1) \propto m_1^{-\alpha}, \quad (\text{D1})$$

and

$$p(m_2 | m_1) = \frac{1}{m_1 - M_{\min}}, \quad (\text{D2})$$

with $M_{\min} = 5 M_{\odot}$ the minimum black hole mass we consider, as in the models of the mass distributions used to infer rates. The joint population distribution on m_1 and m_2 therefore follows

$$p(m_1, m_2 | \alpha) \propto \frac{m_1^{-\alpha}}{m_1 - M_{\min}}. \quad (\text{D3})$$

Here we take all masses to be source-frame masses. The distribution of masses observed in our experiment will differ from the population distribution because our detector sensitivity is a strong function of system mass.

A simplified model of our detection pipeline is that it is a deterministic function of the data, $f(d)$, such that when $f(d) > f_0$ for some threshold f_0 we detect a trigger. Given our population parameter, α , the joint distribution of system parameters and data for a single *detected* trigger with data d is

$$p(d, m_1, m_2 | \alpha) = \frac{p(d | m_1, m_2) p(m_1, m_2 | \alpha)}{\beta(\alpha)}, \quad (\text{D4})$$

where the first term in the numerator is the standard (unnormalised) likelihood function used in our parameter-estimation analysis, the second term is the population distribution in Eq. (D3) and plays a role of a prior in our hierarchical analysis, and $\beta(\alpha)$ is a normalisation factor, ensuring that the joint distribution is properly normalised. This factor is

$$\beta(\alpha) = \int dm_1 dm_2 dd p(d | m_1, m_2) p(m_1, m_2 | \alpha), \quad (\text{D5})$$

where the integral is taken over all allowed masses and the set of data producing a detected trigger $\{d | f(d) > f_0\}$.

Consider first the integral over d . This is

$$\int_{\{d | f(d) > f_0\}} dd p(d | m_1, m_2) p(m_1, m_2 | \alpha) = p(m_1, m_2 | \alpha) P_{\text{det}}(m_1, m_2), \quad (\text{D6})$$

where we have defined the detection probability as a function of mass

$$P_{\text{det}}(m_1, m_2) \equiv \int_{\{d | f(d) > f_0\}} dd p(d | m_1, m_2). \quad (\text{D7})$$

This quantity is proportional to the $\langle VT \rangle$ defined in Eq. (C3) evaluated with a source distribution that fixes the source masses:

$$P_{\text{det}}(m_1, m_2) \propto \langle VT \rangle |_{m_1, m_2}. \quad (\text{D8})$$

To evaluate this factor, we use the approximate recipe from Ref. [42]. Thus

$$\beta(\alpha) \propto \int dm_1 dm_2 p(m_1, m_2 | \alpha) \langle VT \rangle |_{m_1, m_2}. \quad (\text{D9})$$

This normalisation factor accounts for the selection effects of our searches on the observed distribution of masses.

Here we are interested only in the population parameters not in re-analysing the system masses, so we can integrate the masses out of the joint distribution in Eq. (D4) to obtain

$$p(d | \alpha) = \frac{1}{\beta(\alpha)} \int dm_1 dm_2 p(d | m_1, m_2) p(m_1, m_2 | \alpha) \propto \frac{1}{\beta(\alpha)} \langle p(m_1, m_2 | \alpha) \rangle \quad (\text{D10})$$

where the notation $\langle \dots \rangle$ refers to an average over posterior samples (properly re-weighted to correspond to a flat prior in m_1 and m_2) [208].

With multiple triggers analysed, the likelihood is a product of single-event likelihoods from Eq. (D10). We impose a flat prior on α . The posterior from an analysis using GW150914, LVT151012, and GW151226 appears in Figure 11.

- [1] B. P. Abbott, R. Abbott, T. D. Abbott, *et al.* (LIGO Scientific Collaboration, Virgo Collaboration), *Phys. Rev. Lett.* **116**, 131103 (2016), arXiv:1602.03838 [gr-qc].
- [2] T. Dal Canton *et al.*, *Phys. Rev.* **D90**, 082004 (2014), arXiv:1405.6731 [gr-qc].
- [3] S. A. Usman *et al.*, (2015), arXiv:1508.02357 [gr-qc].
- [4] A. H. Nitz, I. W. Harry, J. L. Willis, C. M. Biwer, D. A. Brown, L. P. Pekowsky, T. Dal Canton, A. R. Williamson, T. Dent, C. D. Capano, T. T. Massinger, A. K. Lenon, A. B. Nielsen, and M. Cabero, “PyCBC Software,” <https://github.com/ligo-cbc/pycbc> (2016).
- [5] K. Cannon, R. Cariou, A. Chapman, M. Crispin-Ortuzar, N. Fotopoulos, *et al.*, *Astrophys.J.* **748**, 136 (2012), arXiv:1107.2665 [astro-ph.IM].
- [6] S. Privitera, S. R. P. Mohapatra, P. Ajith, K. Cannon, N. Fotopoulos, M. A. Frei, C. Hanna, A. J. Weinstein, and J. T. Whelan, *Phys. Rev.* **D89**, 024003 (2014), arXiv:1310.5633 [gr-qc].
- [7] C. Messick, K. Blackburn, P. Brady, P. Brockill, K. Cannon, S. Caudill, S. J. Chamberlin, J. D. E. Creighton, R. Everett, C. Hanna, R. N. Lang, T. G. F. Li, D. Meacher, C. Pankow, S. Privitera, H. Qi, S. Sachdev, L. Sadeghian, B. Sathyaprakash, L. Singer, E. G. Thomas, L. Wade, M. Wade, and A. Weinstein, (2016), arXiv:1604.04324 [astro-ph.IM].
- [8] A. Taracchini, A. Buonanno, Y. Pan, T. Hinderer, M. Boyle, *et al.*, *Phys.Rev.* **D89**, 061502 (2014), arXiv:1311.2544 [gr-qc].
- [9] M. Pürrer, *Phys. Rev. D* **93**, 064041 (2016), arXiv:1512.02248 [gr-qc].
- [10] C. Capano, I. Harry, S. Privitera, and A. Buonanno, *Phys. Rev.* **D93**, 124007 (2016), arXiv:1602.03509 [gr-qc].
- [11] B. Allen, W. G. Anderson, P. R. Brady, D. A. Brown, and J. D. E. Creighton, *Phys. Rev. D* **85**, 122006 (2012), arXiv:0509116 [gr-qc].
- [12] K. Cannon, A. Chapman, C. Hanna, D. Keppel, A. C. Searle, and A. J. Weinstein, *Phys. Rev. D* **82**, 044025 (2010), arXiv:1005.0012 [gr-qc].
- [13] B. P. Abbott, R. Abbott, T. D. Abbott, *et al.* (LIGO Scientific Collaboration, Virgo Collaboration), *Class. Quantum Grav.* **33**, 134001 (2016), arXiv:1602.03844 [gr-qc].
- [14] B. Allen, *Phys. Rev. D* **71**, 062001 (2005), arXiv:gr-qc/0405045 [gr-qc].
- [15] K. Cannon, C. Hanna, and J. Peoples, (2015), arXiv:1504.04632 [astro-ph.IM].
- [16] B. P. Abbott, R. Abbott, T. D. Abbott, *et al.* (LIGO Scientific Collaboration, Virgo Collaboration), *Phys. Rev. Lett.* **116**, 061102 (2016), arXiv:1602.03837 [gr-qc].
- [17] B. P. Abbott *et al.* (LIGO Scientific Collaboration, Virgo Collaboration), (2016), <https://dcc.ligo.org/LIGO-P151226/public>.
- [18] L. Blanchet, T. Damour, B. R. Iyer, C. M. Will, and A. G. Wiseman, *Phys. Rev. Lett* **74**, 3515 (1995), arXiv:9501027 [gr-qc].
- [19] L. Blanchet, T. Damour, G. Esposito-Farèse, and B. R. Iyer, *Phys. Rev. Lett* **93**, 091101 (2004), arXiv:0406012 [gr-qc].
- [20] T. Damour, P. Jaranowski, and G. Schafer, *Phys. Lett.* **B513**, 147 (2001), arXiv:gr-qc/0105038 [gr-qc].
- [21] L. Blanchet, G. Faye, B. R. Iyer, and S. Sinha, *Class. Quantum Grav.* **25**, 165003 (2008), arXiv:arXiv:0802.1249 [gr-qc].
- [22] T. Damour, B. R. Iyer, and A. Nagar, *Phys. Rev. D* **79**, 064004 (2009).
- [23] L. Blanchet, *Living Rev. Rel.* **17**, 2 (2014), arXiv:1310.1528 [gr-qc].
- [24] A. Buonanno and T. Damour, *Phys. Rev. D* **62**, 064015 (2000), arXiv:gr-qc/0001013 [gr-qc].
- [25] A. Buonanno and T. Damour, *Phys. Rev. D* **59**, 084006 (1999), arXiv:gr-qc/9811091 [gr-qc].
- [26] T. Damour, P. Jaranowski, and G. Schafer, *Phys. Rev. D* **78**, 024009 (2008), arXiv:0803.0915 [gr-qc].
- [27] T. Damour and A. Nagar, *Phys. Rev. D* **79**, 081503 (2009), arXiv:0902.0136 [gr-qc].
- [28] E. Barausse and A. Buonanno, *Phys. Rev. D* **81**, 084024 (2010), arXiv:0912.3517 [gr-qc].
- [29] F. Pretorius, *Phys. Rev. Lett* **95**, 121101 (2005), arXiv:0507014 [gr-qc].
- [30] M. Campanelli, C. O. Lousto, P. Marronetti, and Y. Zlochower, *Phys. Rev. Lett* **96**, 111101 (2006), arXiv:0511048 [gr-qc].
- [31] J. G. Baker, J. Centrella, D.-I. Choi, M. Koppitz, and J. van Meter, *Phys. Rev. Lett* **96**, 111102 (2006), arXiv:gr-qc/0511103.
- [32] J. G. Baker, J. R. van Meter, S. T. McWilliams, J. Centrella, and B. J. Kelly, *Phys. Rev. Lett* **99**, 181101 (2007), arXiv:0612024 [gr-qc].
- [33] I. Hinder *et al.*, *Class. Quantum Grav.* **31**, 025012 (2014), arXiv:1307.5307 [gr-qc].
- [34] A. H. Mroué *et al.*, *Phys. Rev. Lett.* **111**, 241104 (2013), arXiv:1304.6077 [gr-qc].
- [35] S. Husa, S. Khan, M. Hannam, M. Pürrer, F. Ohme, X. J. Forteza, and A. Bohé, *Phys. Rev. D* **93**, 044006 (2016), arXiv:1508.07250 [gr-qc].
- [36] S. Khan, S. Husa, M. Hannam, F. Ohme, M. Prerer, X. J. Forteza, and A. Boh, *Phys. Rev. D* **93**, 044007 (2016), arXiv:1508.07253 [gr-qc].
- [37] M. Hannam, P. Schmidt, A. Bohé, L. Haegel, S. Husa, F. Ohme, G. Pratten, and M. Pürrer, *Phys. Rev. Lett.* **113**, 151101 (2014), arXiv:1308.3271 [gr-qc].
- [38] B. P. Abbott, R. Abbott, T. D. Abbott, *et al.* (LIGO Scientific Collaboration, Virgo Collaboration), *Phys. Rev. Lett.* **116**, 241102 (2016), <https://dcc.ligo.org/LIGO-P1500218/public/main>, arXiv:1602.03840 [gr-qc].
- [39] B. P. Abbott, R. Abbott, T. D. Abbott, *et al.* (LIGO Scientific Collaboration, Virgo Collaboration), (2016), arXiv:1606.01210 [gr-qc].
- [40] P. A. R. Ade *et al.* (Planck Collaboration), (2015), arXiv:1502.01589 [astro-ph.CO].
- [41] B. P. Abbott, R. Abbott, T. D. Abbott, *et al.* (LIGO Scientific Collaboration, Virgo Collaboration), *Phys. Rev. Lett.* **116**, 221101 (2016), arXiv:1602.03841 [gr-qc].
- [42] B. P. Abbott, R. Abbott, T. D. Abbott, *et al.* (LIGO Scientific Collaboration, Virgo Collaboration), (2016), <https://dcc.ligo.org/LIGO-P1500217/public/main>, arXiv:1602.03842 [astro-ph.HE].
- [43] B. P. Abbott, R. Abbott, T. D. Abbott, *et al.* (LIGO Scientific Collaboration, Virgo Collaboration), *Phys. Rev. D* **93**, 122003 (2016), arXiv:1602.03839 [gr-qc].
- [44] J. Aasi *et al.* (LIGO Scientific Collaboration), *Class. Quantum Grav.* **32**, 074001 (2015), arXiv:1411.4547 [gr-qc].
- [45] J. Veitch, V. Raymond, B. Farr, W. Farr, P. Graff, S. Vitale, B. Aylott, K. Blackburn, N. Christensen, M. Coughlin,

- W. Del Pozzo, F. Feroz, J. Gair, C.-J. Haster, V. Kalogera, T. Littenberg, I. Mandel, R. O’Shaughnessy, M. Pitkin, C. Rodriguez, C. Röver, T. Sidery, R. Smith, M. Van Der Sluys, A. Vecchio, W. Voudsen, and L. Wade, *Phys. Rev. D* **91**, 042003 (2015), arXiv:1409.7215 [gr-qc].
- [46] D. V. Martynov, E. D. Hall, *et al.*, *Phys. Rev. D* **93**, 112004 (2016).
- [47] B. P. Abbott, R. Abbott, T. D. Abbott, *et al.* (LIGO Scientific Collaboration), (2016), <https://dcc.ligo.org/LIGO-P1500248/public/main>, arXiv:1602.03845 [gr-qc].
- [48] L. K. Nuttall *et al.*, *Class. Quantum Grav.* **32**, 245005 (2015), arXiv:1508.07316 [gr-qc].
- [49] A. Effler, R. M. S. Schofield, V. V. Frolov, G. Gonzalez, K. Kawabe, J. R. Smith, J. Birch, and R. McCarthy, *Class. Quantum Grav.* **32**, 035017 (2015), arXiv:1409.5160 [astro-ph.IM].
- [50] B. P. Abbott *et al.* (LIGO Scientific Collaboration, Virgo Collaboration), .
- [51] L. A. Wainstein and V. D. Zubakov, *Extraction of signals from noise* (Prentice-Hall, Englewood Cliffs, NJ, 1962).
- [52] K. S. Thorne, in *Three hundred years of gravitation*, edited by S. W. Hawking and W. Israel (Cambridge University Press, Cambridge, 1987) Chap. 9, pp. 330–458.
- [53] B. S. Sathyaprakash and S. V. Dhurandhar, *Phys. Rev. D* **44**, 3819 (1991).
- [54] C. Cutler *et al.*, *Phys. Rev. Lett* **70**, 2984 (1993), arXiv:9208005 [astro-ph].
- [55] L. S. Finn, *Phys. Rev.* **D46**, 5236 (1992), arXiv:gr-qc/9209010 [gr-qc].
- [56] L. S. Finn and D. F. Chernoff, *Phys. Rev. D* **47**, 2198 (1993), arXiv:9301003 [gr-qc].
- [57] S. V. Dhurandhar and B. S. Sathyaprakash, *Phys. Rev.* **D49**, 1707 (1994).
- [58] R. Balasubramanian, B. S. Sathyaprakash, and S. V. Dhurandhar, *Phys. Rev. D* **53**, 3033 (1996), arXiv:gr-qc/9508011.
- [59] E. E. Flanagan and S. A. Hughes, *Phys. Rev. D* **57**, 4535 (1998), arXiv:9701039 [gr-qc].
- [60] B. P. Abbott, R. Abbott, T. D. Abbott, *et al.* (LIGO Scientific Collaboration, Virgo Collaboration), *Phys. Rev. D* **93**, 122004 (2016), arXiv:1602.03843 [gr-qc].
- [61] B. J. Owen, *Phys. Rev.* **D53**, 6749 (1996), arXiv:gr-qc/9511032 [gr-qc].
- [62] B. J. Owen and B. S. Sathyaprakash, *Phys. Rev. D* **60**, 022002 (1999), arXiv:9808076 [gr-qc].
- [63] S. Babak, R. Balasubramanian, D. Churches, T. Cokelaer, and B. S. Sathyaprakash, *Class. Quantum Grav.* **23**, 5477 (2006).
- [64] T. Cokelaer, *Phys. Rev. D* **76**, 102004 (2007), arXiv:0706.4437 [gr-qc].
- [65] L. E. Kidder, C. M. Will, and A. G. Wiseman, *Phys. Rev.* **D47**, 4183 (1993), arXiv:gr-qc/9211025 [gr-qc].
- [66] L. E. Kidder, *Phys. Rev.* **D52**, 821 (1995), arXiv:gr-qc/9506022 [gr-qc].
- [67] P. C. Peters and J. Mathews, *Phys. Rev.* **131**, 435 (1963).
- [68] P. C. Peters, *Phys. Rev.* **136**, B1224 (1964).
- [69] L. Blanchet, B. R. Iyer, C. M. Will, and A. G. Wiseman, *Class. Quantum Grav.* **13**, 575 (1996), arXiv:gr-qc/9602024 [gr-qc].
- [70] T. Damour, *Phys. Rev. D* **64**, 124013 (2001).
- [71] E. Racine, *Phys. Rev.* **D78**, 044021 (2008), arXiv:0803.1820 [gr-qc].
- [72] P. Ajith, M. Hannam, S. Husa, Y. Chen, B. Brügmann, N. Dorband, D. Müller, F. Ohme, D. Pollney, C. Reisswig, L. Santamaría, and J. Seiler, *Phys. Rev. Lett.* **106**, 241101 (2011), arXiv:0909.2867 [gr-qc].
- [73] L. Santamaría, F. Ohme, P. Ajith, B. Brügmann, N. Dorband, M. Hannam, S. Husa, P. Moesta, D. Pollney, C. Reisswig, E. L. Robinson, J. Seiler, and B. Krishnan, *Phys. Rev. D* **82**, 064016 (2010), arXiv:1005.3306 [gr-qc].
- [74] E. Poisson and C. M. Will, *Phys. Rev. D* **52**, 848 (1995), arXiv:gr-qc/9502040.
- [75] A. Królak, K. D. Kokkotas, and G. Schäfer, *Phys. Rev. D* **52**, 2089 (1995).
- [76] A. B. Nielsen, *Class. Quant. Grav.* **30**, 075023 (2013), arXiv:1203.6603 [gr-qc].
- [77] F. Ohme, A. B. Nielsen, D. Keppel, and A. Lundgren, *Phys. Rev.* **D88**, 042002 (2013), arXiv:1304.7017 [gr-qc].
- [78] J. Antoniadis, P. C. Freire, N. Wex, T. M. Tauris, R. S. Lynch, *et al.*, *Science* **340**, 1233232 (2013), arXiv:1304.6875 [astro-ph.HE].
- [79] K. Belczynski, A. Buonanno, M. Cantiello, C. L. Fryer, D. E. Holz, I. Mandel, M. C. Miller, and M. Walczak, *Astrophys. J.* **789**, 120 (2014), arXiv:1403.0677 [astro-ph.HE].
- [80] C. E. Rhoades, Jr. and R. Ruffini, *Phys. Rev. Lett.* **32**, 324 (1974).
- [81] V. Kalogera and G. Baym, *Astrophys. J.* **470**, L61 (1996), arXiv:astro-ph/9608059 [astro-ph].
- [82] F. Ozel, D. Psaltis, R. Narayan, and J. E. McClintock, *Astrophysical Journal* **725**, 1918 (2010), arXiv:1006.2834 [astro-ph.GA].
- [83] W. M. Farr, N. Sravan, A. Cantrell, L. Kreidberg, C. D. Bailyn, *et al.*, *Astrophys. J.* **741**, 103 (2011), arXiv:1011.1459 [astro-ph.GA].
- [84] L. Kreidberg, C. D. Bailyn, W. M. Farr, and V. Kalogera, *Astrophys. J.* **757**, 36 (2012), arXiv:1205.1805 [astro-ph.HE].
- [85] J. Casares and P. G. Jonker, *Space Sci. Rev.* **183**, 223 (2014), arXiv:1311.5118 [astro-ph.HE].
- [86] J. M. Corral-Santana, J. Casares, T. Munoz-Darias, F. E. Bauer, I. G. Martinez-Pais, and D. M. Russell, *Astron. Astrophys.* **587**, A61 (2016), arXiv:1510.08869 [astro-ph.HE].
- [87] B. E. Tetarenko, G. R. Sivakoff, C. O. Heinke, and J. C. Gladstone, *Astrophys. J. Suppl.* **222**, 15 (2016), arXiv:1512.00778 [astro-ph.HE].
- [88] L. S. Finn and D. F. Chernoff, *Phys. Rev. D* **47**, 2198 (1993), arXiv:gr-qc/9301003.
- [89] E. Berti, V. Cardoso, and C. M. Will, *Phys. Rev. D* **73**, 064030 (2006).
- [90] J. Veitch, M. Prerer, and I. Mandel, *Phys. Rev. Lett.* **115**, 141101 (2015), arXiv:1503.05953 [astro-ph.HE].
- [91] P. B. Graff, A. Buonanno, and B. Sathyaprakash, *Phys. Rev.* **D92**, 022002 (2015), arXiv:1504.04766 [gr-qc].
- [92] C.-J. Haster, Z. Wang, C. P. L. Berry, S. Stevenson, J. Veitch, and I. Mandel, (2015), 10.1093/mnras/stw233, arXiv:1511.01431 [astro-ph.HE].
- [93] C. Cutler and E. Flanagan, *Phys. Rev. D* **49**, 2658 (1994).
- [94] E. Baird, S. Fairhurst, M. Hannam, and P. Murphy, *Phys. Rev.* **D87**, 024035 (2013), arXiv:1211.0546 [gr-qc].
- [95] A. Vecchio, *Phys. Rev.* **D70**, 042001 (2004), arXiv:astro-ph/0304051 [astro-ph].
- [96] S. Vitale, R. Lynch, J. Veitch, V. Raymond, and R. Sturani, *Phys. Rev. Lett.* **112**, 251101 (2014), arXiv:1403.0129 [gr-qc].
- [97] K. Chatziioannou, N. Cornish, A. Klein, and N. Yunes, *Astrophys. J.* **798**, L17 (2015), arXiv:1402.3581 [gr-qc].
- [98] J. Healy, C. O. Lousto, and Y. Zlochower, *Phys. Rev. D* **90**, 104004 (2014), arXiv:1406.7295 [gr-qc].
- [99] J. G. Baker, W. D. Boggs, J. Centrella, B. J. Kelly, S. T. McWilliams, *et al.*, *Phys. Rev.* **D78**, 044046 (2008), arXiv:0805.1428 [gr-qc].
- [100] C. Reisswig, S. Husa, L. Rezzolla, E. N. Dorband, D. Poll-

- ney, and J. Seiler, Phys. Rev. **D80**, 124026 (2009), arXiv:0907.0462 [gr-qc].
- [101] X. Jiménez Forteza *et al.*, *Phenomenological fit of the peak luminosity from non-precessing binary-black-hole coalescences*, Tech. Rep. LIGO-T1600018 (LIGO Project, 2016).
- [102] J. B. Hartle, *Gravity / James B. Hartle. San Francisco, CA, USA: Addison Wesley, ISBN 0-8053-8662-9, 2003, XXII + 582 pp.* (2003).
- [103] W. Israel, Phys. Rev. **164**, 1776 (1967).
- [104] W. Israel, Commun. Math. Phys. **8**, 245 (1968).
- [105] B. Carter, Phys. Rev. Lett. **26**, 331 (1971).
- [106] D. C. Robinson, Phys. Rev. Lett. **34**, 905 (1975).
- [107] G. W. Gibbons, Commun. Math. Phys. **44**, 245 (1975).
- [108] R. D. Blandford and R. L. Znajek, Mon. Not. Roy. Astron. Soc. **179**, 433 (1977).
- [109] R. S. Hanni, Physical Review D **25**, 2509 (1982).
- [110] M. Campanelli, C. O. Lousto, and Y. Zlochower, Phys. Rev. D **74**, 041501 (2006), arXiv:gr-qc/0604012 [gr-qc].
- [111] J. A. Gonzalez, U. Sperhake, B. Brügmann, M. Hannam, and S. Husa, Phys. Rev. Lett **98**, 091101 (2007), arXiv:gr-qc/0610154.
- [112] E. Berti *et al.*, Phys. Rev. D **76**, 064034 (2007), arXiv:gr-qc/0703053.
- [113] N. K. Johnson-McDaniel *et al.*, *Determining the final spin of a binary black hole system including in-plane spins: Method and checks of accuracy*, Tech. Rep. LIGO-T1600168 (LIGO Project, 2016).
- [114] A. Krolak and B. F. Schutz, General Relativity and Gravitation **19**, 1163 (1987).
- [115] S. Nissanke, D. E. Holz, S. A. Hughes, N. Dalal, and J. L. Sievers, Astrophys. J. **725**, 496 (2010), arXiv:0904.1017 [astro-ph.CO].
- [116] B. Farr *et al.*, (2015), arXiv:1508.05336 [astro-ph.HE].
- [117] M. V. van der Sluys, C. Roever, A. Stroeer, N. Christensen, V. Kalogera, R. Meyer, and A. Vecchio, Astrophys. J. **688**, L61 (2008), arXiv:0710.1897 [astro-ph].
- [118] S. Fairhurst, New J.Phys. **11**, 123006 (2009), arXiv:0908.2356 [gr-qc].
- [119] K. Grover, S. Fairhurst, B. F. Farr, I. Mandel, C. Rodriguez, *et al.*, Phys.Rev. **D89**, 042004 (2014), arXiv:1310.7454 [gr-qc].
- [120] L. P. Singer and L. R. Price, Phys. Rev. **D93**, 024013 (2016), arXiv:1508.03634 [gr-qc].
- [121] M. M. Kasliwal and S. Nissanke, Astrophys. J. **789**, L5 (2014), arXiv:1309.1554 [astro-ph.HE].
- [122] L. P. Singer, L. R. Price, B. Farr, A. L. Urban, C. Pankow, *et al.*, Astrophys.J. **795**, 105 (2014), arXiv:1404.5623 [astro-ph.HE].
- [123] R. Essick, S. Vitale, E. Katsavounidis, G. Vedovato, and S. Klimenko, Astrophys. J. **800**, 81 (2015), arXiv:1409.2435 [astro-ph.HE].
- [124] C. P. L. Berry *et al.*, Astrophys. J. **804**, 114 (2015), arXiv:1411.6934 [astro-ph.HE].
- [125] B. F. Schutz, Class. Quantum Grav. **28**, 125023 (2011), arXiv:1102.5421 [astro-ph.IM].
- [126] J. Veitch, I. Mandel, B. Aylott, B. Farr, V. Raymond, C. Rodriguez, M. van der Sluys, V. Kalogera, and A. Vecchio, Phys. Rev. D **85**, 104045 (2012), arXiv:1201.1195 [astro-ph.HE].
- [127] C. L. Rodriguez, B. Farr, V. Raymond, W. M. Farr, T. B. Littenberg, *et al.*, Astrophys.J. **784**, 119 (2014), arXiv:1309.3273 [astro-ph.HE].
- [128] B. P. Abbott *et al.* (LIGO Scientific Collaboration, Virgo Collaboration), Living Rev. Relat. **19**, 1 (2016), arXiv:1304.0670 [gr-qc].
- [129] S. Fairhurst, Class. Quantum Grav. **28**, 105021 (2011), arXiv:1010.6192 [gr-qc].
- [130] A. Ghosh *et al.*, (2016), arXiv:1602.02453 [gr-qc].
- [131] L. Blanchet and B. S. Sathyaprakash, Physical Review Letters **74**, 1067 (1995).
- [132] K. G. Arun, B. R. Iyer, M. S. S. Qusailah, and B. S. Sathyaprakash, Phys. Rev. **D74**, 024006 (2006), arXiv:gr-qc/0604067 [gr-qc].
- [133] C. K. Mishra, K. G. Arun, B. R. Iyer, and B. S. Sathyaprakash, Phys. Rev. **D82**, 064010 (2010), arXiv:1005.0304 [gr-qc].
- [134] N. Yunes and F. Pretorius, Phys. Rev. D **80**, 122003 (2009), arXiv:0909.3328 [gr-qc].
- [135] T. Li, W. Del Pozzo, S. Vitale, C. Van Den Broeck, M. Agathos, *et al.*, Phys.Rev. **D85**, 082003 (2012), arXiv:1110.0530 [gr-qc].
- [136] M. Agathos, W. Del Pozzo, T. G. F. Li, C. Van Den Broeck, J. Veitch, and S. Vitale, Phys. Rev. D **89**, 082001 (2014), arXiv:1311.0420 [gr-qc].
- [137] L. Blanchet and G. Schaefer, Class. Quantum Grav. **10**, 2699 (1993).
- [138] J. Lense and H. Thirring, Physikalische Zeitschrift **19**, 156 (1918).
- [139] B. M. Barker and R. F. O'Connell, Phys. Rev. D **12**, 329 (1975).
- [140] C. Kim, V. Kalogera, and D. R. Lorimer, Astrophysical Journal **584**, 985 (2003).
- [141] W. M. Farr, N. Sravan, A. Cantrell, L. Kreidberg, C. D. Bailyn, I. Mandel, and V. Kalogera, Astrophysical Journal **741**, 103 (2011), arXiv:1011.1459.
- [142] J. Bovy, D. W. Hogg, and S. T. Roweis, Ann. Appl. Stat. **5**, 1657 (2011), arXiv:0905.2979 [stat.ME].
- [143] I. Mandel, Phys. Rev. D **D81**, 084029 (2010), arXiv:0912.5531 [astro-ph.HE].
- [144] D. W. Hogg, A. D. Myers, and J. Bovy, Astrophys. J. **725**, 2166 (2010), arXiv:1008.4146 [astro-ph.SR].
- [145] B. P. Abbott, R. Abbott, T. D. Abbott, *et al.* (LIGO Scientific Collaboration, Virgo Collaboration), Astrophys. J. **818**, L22 (2016), arXiv:1602.03846 [astro-ph.HE].
- [146] S. Sigurdsson and L. Hernquist, Nature **364**, 423 (1993).
- [147] S. F. Portegies Zwart and S. L. W. McMillan, Astrophysical Journal **528**, L17 (2000).
- [148] M. C. Miller and V. M. Lauburg, Astrophysical Journal **692**, 917 (2009), arXiv:0804.2783.
- [149] B. M. Ziosi, M. Mapelli, M. Branchesi, and G. Tormen, MNRAS **441**, 3703 (2014), arXiv:1404.7147.
- [150] C. L. Rodriguez, M. Morscher, B. Pattabiraman, S. Chatterjee, C.-J. Haster, and F. A. Rasio, Physical Review Letters **115**, 051101 (2015), arXiv:1505.00792 [astro-ph.HE].
- [151] A. Tutukov and L. Yungelson, Nauchnye Informatsii **27**, 70 (1973).
- [152] A. V. Tutukov and L. R. Yungelson, Monthly Notices of the Royal Astronomical Society **260**, 675 (1993).
- [153] V. M. Lipunov, K. A. Postnov, and M. E. Prokhorov, MNRAS **288**, 245 (1997), astro-ph/9702060.
- [154] R. Voss and T. M. Tauris, Monthly Notices of the Royal Astronomical Society **342**, 1169 (2003).
- [155] G. Nelemans, in *Astrophysics of Gravitational Wave Sources*, American Institute of Physics Conference Series, Vol. 686, edited by J. M. Centrella (Amer. Inst. Phys., Melville, N.Y., 2003) pp. 263–272.
- [156] K. Belczynski, M. Dominik, T. Bulik, R. O'Shaughnessy, C. Fryer, and D. E. Holz, Astrophysical Journal **715**, L138 (2010), arXiv:1004.0386 [astro-ph.HE].

- [157] K. Belczynski, T. Bulik, and B. Rudak, *Astrophysical Journal* **608**, L45 (2004), arXiv:astro-ph/0403361.
- [158] T. Kinugawa, K. Inayoshi, K. Hotokezaka, D. Nakauchi, and T. Nakamura, *MNRAS* **442**, 2963 (2014), arXiv:1402.6672 [astro-ph.HE].
- [159] I. Mandel and S. E. de Mink, *MNRAS* (2016), 10.1093/mnras/stw379, arXiv:1601.00007 [astro-ph.HE].
- [160] P. Marchant, N. Langer, P. Podsiadlowski, T. M. Tauris, and T. J. Moriya, *Astron. Astrophys.* **588**, A50 (2016), arXiv:1601.03718 [astro-ph.SR].
- [161] K. Belczynski, D. E. Holz, T. Bulik, and R. O’Shaughnessy, (2016), arXiv:1602.04531 [astro-ph.HE].
- [162] J. J. Eldridge and E. R. Stanway, ArXiv e-prints (2016), arXiv:1602.03790 [astro-ph.HE].
- [163] V. M. Lipunov, V. Kornilov, E. Gorbovskoy, N. Tiurina, P. Balanutsa, and A. Kuznetsov, ArXiv e-prints (2016), arXiv:1605.01604 [astro-ph.HE].
- [164] S. E. de Mink and I. Mandel, (2016), 10.1093/mnras/stw1219, arXiv:1603.02291 [astro-ph.HE].
- [165] K. Inayoshi, K. Kashiyama, E. Visbal, and Z. Haiman, ArXiv e-prints (2016), arXiv:1603.06921.
- [166] M. Mapelli, (2016), 10.1093/mnras/stw869, arXiv:1604.03559 [astro-ph.GA].
- [167] M. Spera, M. Mapelli, and A. Bressan, *MNRAS* **451**, 4086 (2015), arXiv:1505.05201 [astro-ph.SR].
- [168] M. Dominik, K. Belczynski, C. Fryer, D. E. Holz, E. Berti, T. Bulik, I. Mandel, and R. O’Shaughnessy, *Astrophysical Journal* **779**, 72 (2013), arXiv:1308.1546 [astro-ph.HE].
- [169] C. L. Rodriguez, C.-J. Haster, S. Chatterjee, V. Kalogera, and F. A. Rasio, ArXiv e-prints (2016), arXiv:1604.04254 [astro-ph.HE].
- [170] M. Dominik, K. Belczynski, C. Fryer, D. E. Holz, E. Berti, T. Bulik, I. Mandel, and R. O’Shaughnessy, *Astrophysical Journal* **759**, 52 (2012), arXiv:1202.4901 [astro-ph.HE].
- [171] B. P. Abbott, R. Abbott, T. D. Abbott, M. R. Abernathy, F. Acernese, K. Ackley, C. Adams, T. Adams, P. Addesso, R. X. Adhikari, and et al., *Physical Review Letters* **116**, 131102 (2016), arXiv:1602.03847 [gr-qc].
- [172] R. F. Webbink, *Astrophysical Journal* **277**, 355 (1984).
- [173] I. Iben, Jr. and A. V. Tutukov, *ApJS* **54**, 335 (1984).
- [174] M. de Kool, E. P. J. van den Heuvel, and E. Pylyser, *A&A* **183**, 47 (1987).
- [175] M. Dominik, E. Berti, R. O’Shaughnessy, I. Mandel, K. Belczynski, C. Fryer, D. E. Holz, T. Bulik, and F. Pannarale, *Astrophysical Journal* **806**, 263 (2015), arXiv:1405.7016 [astro-ph.HE].
- [176] R. O’Shaughnessy, V. Kalogera, and K. Belczynski, *Astrophysical Journal* **620**, 385 (2005), arXiv:astro-ph/0408387.
- [177] I. Mandel, C.-J. Haster, M. Dominik, and K. Belczynski, *MNRAS* **450**, L85 (2015), arXiv:1503.03172 [astro-ph.HE].
- [178] T. Bulik and K. Belczyński, *Astrophysical Journal* **589**, L37 (2003), astro-ph/0301470.
- [179] I. Mandel and R. O’Shaughnessy, *Classical and Quantum Gravity* **27**, 114007 (2010), arXiv:0912.1074.
- [180] S. Vitale, R. Lynch, P. Graff, and R. Sturani, ArXiv e-prints (2015), arXiv:1503.04307 [gr-qc].
- [181] S. Stevenson, F. Ohme, and S. Fairhurst, *Astrophysical Journal* **810**, 58 (2015), arXiv:1504.07802 [astro-ph.HE].
- [182] A. Sesana, ArXiv e-prints (2016), arXiv:1602.06951 [gr-qc].
- [183] A. Nishizawa, E. Berti, A. Klein, and A. Sesana, ArXiv e-prints (2016), arXiv:1605.01341 [gr-qc].
- [184] S. Vitale, ArXiv e-prints (2016), arXiv:1605.01037 [gr-qc].
- [185] K. Cannon, A. Chapman, C. Hanna, D. Keppel, A. C. Searle, and A. J. Weinstein, *Phys. Rev. D* **82**, 044025 (2010).
- [186] F. Robinet, <https://tds.ego-gw.it/ql/?c=10651> (2015).
- [187] B. P. Abbott *et al.* (Virgo, LIGO Scientific), (2016), arXiv:1602.03839 [gr-qc].
- [188] “Gstreamer plugins for the LSC Algorithm Library,” <https://www.lsc-group.phys.uwm.edu/daswg/projects/gstlal.html> (2016).
- [189] K. C. Cannon, *Classical and Quantum Gravity* **25**, 105024 (2008).
- [190] K. Cannon, C. Hanna, and D. Keppel, *Phys. Rev. D* **88**, 024025 (2013).
- [191] T. Bayes and R. Price, *Phil. Trans. Roy. Soc. Lond.* **53**, 370 (1763).
- [192] E. T. Jaynes, *Probability Theory: The Logic of Science*, edited by G. L. Bretthorst (Cambridge University Press, Cambridge, 2003).
- [193] W. M. Farr, B. Farr, and T. Littenberg, *Modelling Calibration Errors In CBC Waveforms*, Tech. Rep. LIGO-T1400682 (LIGO Project, 2015).
- [194] Y. Pan, A. Buonanno, A. Taracchini, L. E. Kidder, A. H. Mroué, H. P. Pfeiffer, M. A. Scheel, and B. Szilgyi, *Phys. Rev. D* **89**, 084006 (2014), arXiv:1307.6232 [gr-qc].
- [195] J. Veitch and A. Vecchio, *Phys. Rev. D* **81**, 062003 (2010), arXiv:0911.3820 [astro-ph.CO].
- [196] H. Jeffreys, *Theory of Probability*, 3rd ed., Oxford Classic Texts in the Physical Sciences (Clarendon Press, Oxford, 1961).
- [197] D. J. Spiegelhalter, N. G. Best, B. P. Carlin, and A. van der Linde, *Journal of the Royal Statistical Society. Series B (Statistical Methodology)* **64**, 583 (2002).
- [198] A. van der Linde, *Statistica Neerlandica* **59**, 45 (2005).
- [199] A. Gelman, J. Hwang, and A. Vehtari, ArXiv e-prints (2013), arXiv:1307.5928 [stat.ME].
- [200] E. E. Flanagan and S. A. Hughes, *Phys. Rev. D* **57**, 4566 (1998), arXiv:gr-qc/9710129 [gr-qc].
- [201] C. Cutler and M. Vallisneri, *Phys. Rev. D* **76**, 104018 (2007), arXiv:0707.2982 [gr-qc].
- [202] J. Aasi *et al.* (LIGO Collaboration, Virgo Collaboration), *Phys. Rev. D* **88**, 062001 (2013), arXiv:1304.1775 [gr-qc].
- [203] B. P. Abbott, R. Abbott, T. D. Abbott, *et al.* (LIGO Scientific Collaboration, Virgo Collaboration), (2016), arXiv:1606.01262 [gr-qc].
- [204] C. J. Moore, C. P. Berry, A. J. K. Chua, and J. R. Gair, *Phys. Rev. D* **93**, 064001 (2016), arXiv:1509.04066 [gr-qc].
- [205] J. Aasi *et al.* (LIGO Collaboration, Virgo Collaboration), *Phys. Rev. D* **88**, 062001 (2013), arXiv:1304.1775 [gr-qc].
- [206] W. M. Farr, J. R. Gair, I. Mandel, and C. Cutler, *Phys. Rev. D* **91**, 023005 (2015), arXiv:1302.5341 [astro-ph.IM].
- [207] D. W. Hogg, ArXiv Astrophysics e-prints (1999), astro-ph/9905116.
- [208] I. Mandel, W. M. Farr, and J. Gair, *Extracting distribution parameters from multiple uncertain observations with selection biases*, Tech. Rep. P1600187 (LIGO, <https://dcc.ligo.org/LIGO-P1600187/public>, 2016).

Authors

B. P. Abbott,¹ R. Abbott,¹ T. D. Abbott,² M. R. Abernathy,³ F. Acernese,^{4,5} K. Ackley,⁶ C. Adams,⁷ T. Adams,⁸ P. Addesso,⁹

- R. X. Adhikari,¹ V. B. Adya,¹⁰ C. Affeldt,¹⁰ M. Agathos,¹¹ K. Agatsuma,¹¹ N. Aggarwal,¹² O. D. Aguiar,¹³ L. Aiello,^{14,15}
 A. Ain,¹⁶ P. Ajith,¹⁷ B. Allen,^{10,18,19} A. Allocca,^{20,21} P. A. Altin,²² S. B. Anderson,¹ W. G. Anderson,¹⁸ K. Arai,¹
 M. C. Araya,¹ C. C. Arceneaux,²³ J. S. Areeda,²⁴ N. Arnaud,²⁵ K. G. Arun,²⁶ S. Ascenzi,^{27,15} G. Ashton,²⁸ M. Ast,²⁹
 S. M. Aston,⁷ P. Astone,³⁰ P. Aufmuth,¹⁹ C. Aulbert,¹⁰ S. Babak,³¹ P. Bacon,³² M. K. M. Bader,¹¹ P. T. Baker,³³
 F. Baldaccini,^{34,35} G. Ballardini,³⁶ S. W. Ballmer,³⁷ J. C. Barayoga,¹ S. E. Barclay,³⁸ B. C. Barish,¹ D. Barker,³⁹ F. Barone,^{4,5}
 B. Barr,³⁸ L. Barsotti,¹² M. Barsuglia,³² D. Barta,⁴⁰ J. Bartlett,³⁹ I. Bartos,⁴¹ R. Bassiri,⁴² A. Basti,^{20,21} J. C. Batch,³⁹
 C. Baune,¹⁰ V. Bavigadda,³⁶ M. Bazzan,^{43,44} M. Bejger,⁴⁵ A. S. Bell,³⁸ B. K. Berger,¹ G. Bergmann,¹⁰ C. P. L. Berry,⁴⁶
 D. Bersanetti,^{47,48} A. Bertolini,¹¹ J. Betzwieser,⁷ S. Bhagwat,³⁷ R. Bhandare,⁴⁹ I. A. Bilenko,⁵⁰ G. Billingsley,¹ J. Birch,⁷
 R. Birney,⁵¹ O. Birnholtz,¹⁰ S. Biscans,¹² A. Bisht,^{10,19} M. Bitossi,³⁶ C. Biwer,³⁷ M. A. Bizouard,²⁵ J. K. Blackburn,¹
 C. D. Blair,⁵² D. G. Blair,⁵² R. M. Blair,³⁹ S. Bloemen,⁵³ O. Bock,¹⁰ M. Boer,⁵⁴ G. Bogaert,⁵⁴ C. Bogan,¹⁰ A. Bohe,³¹
 C. Bond,⁴⁶ F. Bondu,⁵⁵ R. Bonnand,⁸ B. A. Boom,¹¹ R. Bork,¹ V. Boschi,^{20,21} S. Bose,^{56,16} Y. Bouffanais,³² A. Bozzi,³⁶
 C. Bradaschia,²¹ P. R. Brady,¹⁸ V. B. Braginsky*,⁵⁰ M. Branchesi,^{57,58} J. E. Brau,⁵⁹ T. Briant,⁶⁰ A. Brillat,⁵⁴ M. Brinkmann,¹⁰
 V. Brisson,²⁵ P. Brockill,¹⁸ J. E. Broida,⁶¹ A. F. Brooks,¹ D. A. Brown,³⁷ D. D. Brown,⁴⁶ N. M. Brown,¹² S. Brunett,¹
 C. C. Buchanan,² A. Buikema,¹² T. Bulik,⁶² H. J. Bulten,^{63,11} A. Buonanno,^{31,64} D. Buskulic,⁸ C. Buy,³² R. L. Byer,⁴²
 M. Cabero,¹⁰ L. Cadonati,⁶⁵ G. Cagnoli,^{66,67} C. Cahillane,¹ J. Calderón Bustillo,⁶⁵ T. Callister,¹ E. Calloni,^{68,5} J. B. Camp,⁶⁹
 K. C. Cannon,⁷⁰ J. Cao,⁷¹ C. D. Capano,¹⁰ E. Capocasa,³² F. Carbognani,³⁶ S. Caride,⁷² J. Casanueva Diaz,²⁵ C. Casentini,^{27,15}
 S. Caudill,¹⁸ M. Cavaglià,²³ F. Cavalier,²⁵ R. Cavalieri,³⁶ G. Cella,²¹ C. B. Cepeda,¹ L. Cerboni Baiardi,^{57,58} G. Cerretani,^{20,21}
 E. Cesarini,^{27,15} S. J. Chamberlin,⁷³ M. Chan,³⁸ S. Chao,⁷⁴ P. Charlton,⁷⁵ E. Chassande-Mottin,³² B. D. Cheeseboro,⁷⁶
 H. Y. Chen,⁷⁷ Y. Chen,⁷⁸ C. Cheng,⁷⁴ A. Chincarini,⁴⁸ A. Chiummo,³⁶ H. S. Cho,⁷⁹ M. Cho,⁶⁴ J. H. Chow,²² N. Christensen,⁶¹
 Q. Chu,⁵² S. Chua,⁶⁰ S. Chung,⁵² G. Ciani,⁶ F. Clara,³⁹ J. A. Clark,⁶⁵ F. Cleva,⁵⁴ E. Coccia,^{27,14} P.-F. Cohadon,⁶⁰ A. Colla,^{80,30}
 C. G. Collette,⁸¹ L. Cominsky,⁸² M. Constancio Jr.,¹³ A. Conte,^{80,30} L. Conti,⁴⁴ D. Cook,³⁹ T. R. Corbitt,² N. Cornish,³³
 A. Corsi,⁷² S. Cortese,³⁶ C. A. Costa,¹³ M. W. Coughlin,⁶¹ S. B. Coughlin,⁸³ J.-P. Coulon,⁵⁴ S. T. Countryman,⁴¹ P. Couvares,¹
 E. E. Cowan,⁶⁵ D. M. Coward,⁵² M. J. Cowart,⁷ D. C. Coyne,¹ R. Coyne,⁷² K. Craig,³⁸ J. D. E. Creighton,¹⁸ J. Cripe,²
 S. G. Crowder,⁸⁴ A. Cumming,³⁸ L. Cunningham,³⁸ E. Cuoco,³⁶ T. Dal Canton,¹⁰ S. L. Danilishin,³⁸ S. D'Antonio,¹⁵
 K. Danzmann,^{19,10} N. S. Darman,⁸⁵ A. Dasgupta,⁸⁶ C. F. Da Silva Costa,⁶ V. Dattilo,³⁶ I. Dave,⁴⁹ M. Davier,²⁵
 G. S. Davies,³⁸ E. J. Daw,⁸⁷ R. Day,³⁶ S. De,³⁷ D. DeBra,⁴² G. Debreczeni,⁴⁰ J. Degallaix,⁶⁶ M. De Laurentis,^{68,5}
 S. Deléglise,⁶⁰ W. Del Pozzo,⁴⁶ T. Denker,¹⁰ T. Dent,¹⁰ V. Dergachev,¹ R. De Rosa,^{68,5} R. T. DeRosa,⁷ R. DeSalvo,⁹
 R. C. Devine,⁷⁶ S. Dhurandhar,¹⁶ M. C. Díaz,⁸⁸ L. Di Fiore,⁵ M. Di Giovanni,^{89,90} T. Di Girolamo,^{68,5} A. Di Lieto,^{20,21}
 S. Di Pace,^{80,30} I. Di Palma,^{31,80,30} A. Di Virgilio,²¹ V. Dolique,⁶⁶ F. Donovan,¹² K. L. Dooley,²³ S. Doravari,¹⁰ R. Douglas,³⁸
 T. P. Downes,¹⁸ M. Drago,¹⁰ R. W. P. Drever,¹ J. C. Driggers,³⁹ M. Ducrot,⁸ S. E. Dwyer,³⁹ T. B. Edo,⁸⁷ M. C. Edwards,⁶¹
 A. Effler,⁷ H.-B. Eggenstein,¹⁰ P. Ehrens,¹ J. Eichholz,^{6,1} S. S. Eikenberry,⁶ W. Engels,⁷⁸ R. C. Essick,¹² T. Etzel,¹
 M. Evans,¹² T. M. Evans,⁷ R. Everett,⁷³ M. Factourovich,⁴¹ V. Fafone,^{27,15} H. Fair,³⁷ S. Fairhurst,⁹¹ X. Fan,⁷¹ Q. Fang,⁵²
 S. Farinon,⁴⁸ B. Farr,⁷⁷ W. M. Farr,⁴⁶ M. Favata,⁹² M. Fays,⁹¹ H. Fehrmann,¹⁰ M. M. Fejer,⁴² E. Fenyvesi,⁹³ I. Ferrante,^{20,21}
 E. C. Ferreira,¹³ F. Ferrini,³⁶ F. Fidecaro,^{20,21} I. Fiori,³⁶ D. Fiorucci,³² R. P. Fisher,³⁷ R. Flaminio,^{66,94} M. Fletcher,³⁸
 H. Fong,⁹⁵ J.-D. Fournier,⁵⁴ S. Frasca,^{80,30} F. Frasconi,²¹ Z. Frei,⁹³ A. Freise,⁴⁶ R. Frey,⁵⁹ V. Frey,²⁵ P. Fritschel,¹²
 V. V. Frolov,⁷ P. Fulda,⁶ M. Fyffe,⁷ H. A. G. Gabbard,²³ S. Gaebel,⁴⁶ J. R. Gair,⁹⁶ L. Gammaitoni,³⁴ S. G. Gaonkar,¹⁶
 F. Garufi,^{68,5} G. Gaur,^{97,86} N. Gehrels,⁶⁹ G. Gemme,⁴⁸ P. Geng,⁸⁸ E. Genin,³⁶ A. Gennai,²¹ J. George,⁴⁹ L. Gergely,⁹⁸
 V. Germain,⁸ Abhirup Ghosh,¹⁷ Archisman Ghosh,¹⁷ S. Ghosh,^{53,11} J. A. Giaime,^{2,7} K. D. Giardino,⁷ A. Giazotto,²¹
 K. Gill,⁹⁹ A. Glaefke,³⁸ E. Goetz,³⁹ R. Goetz,⁶ L. Gondan,⁹³ G. González,² J. M. Gonzalez Castro,^{20,21} A. Gopakumar,¹⁰⁰
 N. A. Gordon,³⁸ M. L. Gorodetsky,⁵⁰ S. E. Gossan,¹ M. Gosselin,³⁶ R. Gouaty,⁸ A. Grado,^{101,5} C. Graef,³⁸ P. B. Graff,⁶⁴
 M. Granata,⁶⁶ A. Grant,³⁸ S. Gras,¹² C. Gray,³⁹ G. Greco,^{57,58} A. C. Green,⁴⁶ P. Groot,⁵³ H. Grote,¹⁰ S. Grunewald,³¹
 G. M. Guidi,^{57,58} X. Guo,⁷¹ A. Gupta,¹⁶ M. K. Gupta,⁸⁶ K. E. Gushwa,¹ E. K. Gustafson,¹ R. Gustafson,¹⁰² J. J. Hacker,²⁴
 B. R. Hall,⁵⁶ E. D. Hall,¹ H. Hamilton,¹⁰³ G. Hammond,³⁸ M. Haney,¹⁰⁰ M. M. Hanke,¹⁰ J. Hanks,³⁹ C. Hanna,⁷³
 M. D. Hannam,⁹¹ J. Hanson,⁷ T. Hardwick,² J. Harms,^{57,58} G. M. Harry,³ I. W. Harry,³¹ M. J. Hart,³⁸ M. T. Hartman,⁶
 C.-J. Haster,⁴⁶ K. Haughian,³⁸ J. Healy,¹⁰⁴ A. Heidmann,⁶⁰ M. C. Heintze,⁷ H. Heitmann,⁵⁴ P. Hello,²⁵ G. Hemming,³⁶
 M. Hendry,³⁸ I. S. Heng,³⁸ J. Hennig,³⁸ J. Henry,¹⁰⁴ A. W. Heptonstall,¹ M. Heurs,^{10,19} S. Hild,³⁸ D. Hoak,³⁶ D. Hofman,⁶⁶
 K. Holt,⁷ D. E. Holz,⁷⁷ P. Hopkins,⁹¹ J. Hough,³⁸ E. A. Houston,³⁸ E. J. Howell,⁵² Y. M. Hu,¹⁰ S. Huang,⁷⁴
 E. A. Huerta,¹⁰⁵ D. Huet,²⁵ B. Hughey,⁹⁹ S. Husa,¹⁰⁶ S. H. Huttner,³⁸ T. Huynh-Dinh,⁷ N. Indik,¹⁰ D. R. Ingram,³⁹
 R. Inta,⁷² H. N. Isa,³⁸ J.-M. Isac,⁶⁰ M. Isi,¹ T. Isogai,¹² B. R. Iyer,¹⁷ K. Izumi,³⁹ T. Jacqmin,⁶⁰ H. Jang,⁷⁹ K. Jani,⁶⁵
 P. Jananowski,¹⁰⁷ S. Jawahar,¹⁰⁸ L. Jian,⁵² F. Jiménez-Forteza,¹⁰⁶ W. W. Johnson,² N. Johnson-McDaniel,¹⁷ D. I. Jones,²⁸
 R. Jones,³⁸ R. J. G. Jonker,¹¹ L. Ju,⁵² Haris K,¹⁰⁹ C. V. Kalaghatgi,⁹¹ V. Kalogera,⁸³ S. Kandhasamy,²³ G. Kang,⁷⁹
 J. B. Kanner,¹ S. J. Kapadia,¹⁰ S. Karki,⁵⁹ K. S. Karvinen,¹⁰ M. Kasprzack,^{36,2} E. Katsavounidis,¹² W. Katzman,⁷
 S. Kaufer,¹⁹ T. Kaur,⁵² K. Kawabe,³⁹ F. Kéfélian,⁵⁴ M. S. Kehl,⁹⁵ D. Keitel,¹⁰⁶ D. B. Kelley,³⁷ W. Kells,¹ R. Kennedy,⁸⁷

- J. S. Key,⁸⁸ F. Y. Khalili,⁵⁰ I. Khan,¹⁴ S. Khan,⁹¹ Z. Khan,⁸⁶ E. A. Khazanov,¹¹⁰ N. Kijbunchoo,³⁹ Chi-Woong Kim,⁷⁹ Chunglee Kim,⁷⁹ J. Kim,¹¹¹ K. Kim,¹¹² N. Kim,⁴² W. Kim,¹¹³ Y.-M. Kim,¹¹¹ S. J. Kimbrell,⁶⁵ E. J. King,¹¹³ P. J. King,³⁹ J. S. Kissel,³⁹ B. Klein,⁸³ L. Kleybolte,²⁹ S. Klimenko,⁶ S. M. Koehlenbeck,¹⁰ S. Koley,¹¹ V. Kondrashov,¹ A. Kontos,¹² M. Korobko,²⁹ W. Z. Korth,¹ I. Kowalska,⁶² D. B. Kozak,¹ V. Kringel,¹⁰ B. Krishnan,¹⁰ A. Królak,^{114,115} C. Krueger,¹⁹ G. Kuehn,¹⁰ P. Kumar,⁹⁵ R. Kumar,⁸⁶ L. Kuo,⁷⁴ A. Kutynia,¹¹⁴ B. D. Lackey,³⁷ M. Landry,³⁹ J. Lange,¹⁰⁴ B. Lantz,⁴² P. D. Lasky,¹¹⁶ M. Laxen,⁷ A. Lazzarini,¹ C. Lazzaro,⁴⁴ P. Leaci,^{80,30} S. Leavey,³⁸ E. O. Lebigot,^{32,71} C. H. Lee,¹¹¹ H. K. Lee,¹¹² H. M. Lee,¹¹⁷ K. Lee,³⁸ A. Lenon,³⁷ M. Leonardi,^{89,90} J. R. Leong,¹⁰ N. Leroy,²⁵ N. Letendre,⁸ Y. Levin,¹¹⁶ J. B. Lewis,¹ T. G. F. Li,¹¹⁸ A. Libson,¹² T. B. Littenberg,¹¹⁹ N. A. Lockerbie,¹⁰⁸ A. L. Lombardi,¹²⁰ L. T. London,⁹¹ J. E. Lord,³⁷ M. Lorenzini,^{14,15} V. Lorientte,¹²¹ M. Lormand,⁷ G. Losurdo,⁵⁸ J. D. Lough,^{10,19} C. Lousto,¹⁰⁴ H. Lück,^{19,10} A. P. Lundgren,¹⁰ R. Lynch,¹² Y. Ma,⁵² B. Machenschalk,¹⁰ M. MacInnis,¹² D. M. Macleod,² F. Magaña-Sandoval,³⁷ L. Magaña Zertuche,³⁷ R. M. Magee,⁵⁶ E. Majorana,³⁰ I. Maksimovic,¹²¹ V. Malvezzi,^{27,15} N. Man,⁵⁴ I. Mandel,⁴⁶ V. Mandic,⁸⁴ V. Mangano,³⁸ G. L. Mansell,²² M. Manske,¹⁸ M. Mantovani,³⁶ F. Marchesoni,^{122,35} F. Marion,⁸ S. Márka,⁴¹ Z. Márka,⁴¹ A. S. Markosyan,⁴² E. Maros,¹ F. Martelli,^{57,58} L. Martellini,⁵⁴ I. W. Martin,³⁸ D. V. Martynov,¹² J. N. Marx,¹ K. Mason,¹² A. Masserot,⁸ T. J. Massinger,³⁷ M. Masso-Reid,³⁸ S. Mastrogiovanni,^{80,30} F. Matichard,¹² L. Matone,⁴¹ N. Mavalvala,¹² N. Mazumder,⁵⁶ R. McCarthy,³⁹ D. E. McClelland,²² S. McCormick,⁷ S. C. McGuire,¹²³ G. McIntyre,¹ J. McIver,¹ D. J. McManus,²² T. McRae,²² S. T. McWilliams,⁷⁶ D. Meacher,⁷³ G. D. Meadors,^{31,10} J. Meidam,¹¹ A. Melatos,⁸⁵ G. Mendell,³⁹ R. A. Mercer,¹⁸ E. L. Merilh,³⁹ M. Merzougui,⁵⁴ S. Meshkov,¹ C. Messenger,³⁸ C. Messick,⁷³ R. Metzдорff,⁶⁰ P. M. Meyers,⁸⁴ F. Mezzani,^{30,80} H. Miao,⁴⁶ C. Michel,⁶⁶ H. Middleton,⁴⁶ E. E. Mikhailov,¹²⁴ L. Milano,^{68,5} A. L. Miller,^{6,80,30} A. Miller,⁸³ B. B. Miller,⁸³ J. Miller,¹² M. Millhouse,³³ Y. Minenkov,¹⁵ J. Ming,³¹ S. Mirshekari,¹²⁵ C. Mishra,¹⁷ S. Mitra,¹⁶ V. P. Mitrofanov,⁵⁰ G. Mitselmakher,⁶ R. Mittleman,¹² A. Moggi,²¹ M. Mohan,³⁶ S. R. P. Mohapatra,¹² M. Montani,^{57,58} B. C. Moore,⁹² C. J. Moore,¹²⁶ D. Moraru,³⁹ G. Moreno,³⁹ S. R. Morriss,⁸⁸ K. Mossavi,¹⁰ B. Mours,⁸ C. M. Mow-Lowry,⁴⁶ G. Mueller,⁶ A. W. Muir,⁹¹ Arunava Mukherjee,¹⁷ D. Mukherjee,¹⁸ S. Mukherjee,⁸⁸ N. Mukund,¹⁶ A. Mullavey,⁷ J. Munch,¹¹³ D. J. Murphy,⁴¹ P. G. Murray,³⁸ A. Mytidis,⁶ I. Nardecchia,^{27,15} L. Naticchioni,^{80,30} R. K. Nayak,¹²⁷ K. Nedkova,¹²⁰ G. Nelemans,^{53,11} T. J. N. Nelson,⁷ M. Neri,^{47,48} A. Neunzert,¹⁰² G. Newton,³⁸ T. T. Nguyen,²² A. B. Nielsen,¹⁰ S. Nissanke,^{53,11} A. Nitz,¹⁰ F. Nocera,³⁶ D. Nolting,⁷ M. E. N. Normandin,⁸⁸ L. K. Nuttall,³⁷ J. Oberling,³⁹ E. Ochsner,¹⁸ J. O'Dell,¹²⁸ E. Oelker,¹² G. H. Ogin,¹²⁹ J. J. Oh,¹³⁰ S. H. Oh,¹³⁰ F. Ohme,⁹¹ M. Oliver,¹⁰⁶ P. Oppermann,¹⁰ Richard J. Oram,⁷ B. O'Reilly,⁷ R. O'Shaughnessy,¹⁰⁴ D. J. Ottaway,¹¹³ H. Overmier,⁷ B. J. Owen,⁷² A. Pai,¹⁰⁹ S. A. Pai,⁴⁹ J. R. Palamos,⁵⁹ O. Palashov,¹¹⁰ C. Palomba,³⁰ A. Pal-Singh,²⁹ H. Pan,⁷⁴ Y. Pan,⁶⁴ C. Pankow,⁸³ F. Pannarale,⁹¹ B. C. Pant,⁴⁹ F. Paoletti,^{36,21} A. Paoli,³⁶ M. A. Papa,^{31,18,10} H. R. Paris,⁴² W. Parker,⁷ D. Pascucci,³⁸ A. Pasqualetti,³⁶ R. Passaquieti,^{20,21} D. Passuello,²¹ B. Patricelli,^{20,21} Z. Patrick,⁴² B. L. Pearlstone,³⁸ M. Pedraza,¹ R. Pedurand,^{66,131} L. Pekowsky,³⁷ A. Pele,⁷ S. Penn,¹³² A. Perreca,¹ L. M. Perri,⁸³ H. Pfeiffer,⁹⁵ M. Phelps,³⁸ O. J. Piccinni,^{80,30} M. Pichot,⁵⁴ F. Piergiovanni,^{57,58} V. Pierro,⁹ G. Pillant,³⁶ L. Pinard,⁶⁶ I. M. Pinto,⁹ M. Pitkin,³⁸ M. Poe,¹⁸ R. Poggiani,^{20,21} P. Popolizio,³⁶ E. Porter,³² A. Post,¹⁰ J. Powell,³⁸ J. Prasad,¹⁶ V. Predoi,⁹¹ T. Prestegard,⁸⁴ L. R. Price,¹ M. Prijatelj,^{10,36} M. Principe,⁹ S. Privitera,³¹ R. Prix,¹⁰ G. A. Prodi,^{89,90} L. Prokhorov,⁵⁰ O. Puncken,¹⁰ M. Punturo,³⁵ P. Puppo,³⁰ M. Pürer,³¹ H. Qi,¹⁸ J. Qin,⁵² S. Qiu,¹¹⁶ V. Quetschke,⁸⁸ E. A. Quintero,¹ R. Quitzow-James,⁵⁹ F. J. Raab,³⁹ D. S. Rabeling,²² H. Radkins,³⁹ P. Raffai,⁹³ S. Raja,⁴⁹ C. Rajan,⁴⁹ M. Rakhmanov,⁸⁸ P. Rapagnani,^{80,30} V. Raymond,³¹ M. Razzano,^{20,21} V. Re,²⁷ J. Read,²⁴ C. M. Reed,³⁹ T. Regimbau,⁵⁴ L. Rei,⁴⁸ S. Reid,⁵¹ D. H. Reitze,^{1,6} H. Rew,¹²⁴ S. D. Reyes,³⁷ F. Ricci,^{80,30} K. Riles,¹⁰² M. Rizzo,¹⁰⁴ N. A. Robertson,^{1,38} R. Robie,³⁸ F. Robinet,²⁵ A. Rocchi,¹⁵ L. Rolland,⁸ J. G. Rollins,¹ V. J. Roma,⁵⁹ J. D. Romano,⁸⁸ R. Romano,^{4,5} G. Romanov,¹²⁴ J. H. Romie,⁷ D. Rosińska,^{133,45} S. Rowan,³⁸ A. Rüdiger,¹⁰ P. Ruggi,³⁶ K. Ryan,³⁹ S. Sachdev,¹ T. Sadecki,³⁹ L. Sadeghian,¹⁸ M. Sakellariadou,¹³⁴ L. Salconi,³⁶ M. Saleem,¹⁰⁹ F. Salemi,¹⁰ A. Samajdar,¹²⁷ L. Sammut,¹¹⁶ E. J. Sanchez,¹ V. Sandberg,³⁹ B. Sandeen,⁸³ J. R. Sanders,³⁷ B. Sassolas,⁶⁶ B. S. Sathyaprakash,⁹¹ P. R. Saulson,³⁷ O. E. S. Sauter,¹⁰² R. L. Savage,³⁹ A. Sawadsky,¹⁹ P. Schale,⁵⁹ R. Schilling,[†] 10 J. Schmidt,¹⁰ P. Schmidt,^{1,78} R. Schnabel,²⁹ R. M. S. Schofield,⁵⁹ A. Schönbeck,²⁹ E. Schreiber,¹⁰ D. Schuette,^{10,19} B. F. Schutz,^{91,31} J. Scott,³⁸ S. M. Scott,²² D. Sellers,⁷ A. S. Sengupta,⁹⁷ D. Sentenac,³⁶ V. Sequino,^{27,15} A. Sergeev,¹¹⁰ Y. Setyawati,^{53,11} D. A. Shaddock,²² T. Shaffer,³⁹ M. S. Shahrar,⁸³ M. Shaltev,¹⁰ B. Shapiro,⁴² P. Shawhan,⁶⁴ A. Sheperd,¹⁸ D. H. Shoemaker,¹² D. M. Shoemaker,⁶⁵ K. Siellez,⁶⁵ X. Siemens,¹⁸ M. Sieniawska,⁴⁵ D. Sigg,³⁹ A. D. Silva,¹³ A. Singer,¹ L. P. Singer,⁶⁹ A. Singh,^{31,10,19} R. Singh,² A. Singhal,¹⁴ A. M. Sintes,¹⁰⁶ B. J. J. Slagmolen,²² J. R. Smith,²⁴ N. D. Smith,¹ R. J. E. Smith,¹ E. J. Son,¹³⁰ B. Sorazu,³⁸ F. Sorrentino,⁴⁸ T. Souradeep,¹⁶ A. K. Srivastava,⁸⁶ A. Staley,⁴¹ M. Steinke,¹⁰ J. Steinlechner,³⁸ S. Steinlechner,³⁸ D. Steinmeyer,^{10,19} B. C. Stephens,¹⁸ S. Stevenson,⁴⁶ R. Stone,⁸⁸ K. A. Strain,³⁸ N. Straniero,⁶⁶ G. Stratta,^{57,58} N. A. Strauss,⁶¹ S. Strigin,⁵⁰ R. Sturani,¹²⁵ A. L. Stuver,⁷ T. Z. Summerscales,¹³⁵ L. Sun,⁸⁵ S. Sunil,⁸⁶ P. J. Sutton,⁹¹ B. L. Swinkels,³⁶ M. J. Szczepańczyk,⁹⁹ M. Tacca,³² D. Talukder,⁵⁹ D. B. Tanner,⁶ M. Tápai,⁹⁸ S. P. Tarabrin,¹⁰ A. Taracchini,³¹ R. Taylor,¹ T. Theeg,¹⁰ M. P. Thirugnanasambandam,¹ E. G. Thomas,⁴⁶ M. Thomas,⁷ P. Thomas,³⁹ K. A. Thorne,⁷ E. Thrane,¹¹⁶ S. Tiwari,^{14,90} V. Tiwari,⁹¹ K. V. Tokmakov,¹⁰⁸ K. Toland,³⁸ C. Tomlinson,⁸⁷

M. Tonelli,^{20,21} Z. Tornasi,³⁸ C. V. Torres^{‡,88} C. I. Torrie,¹ D. Töyrä,⁴⁶ F. Travasso,^{34,35} G. Traylor,⁷ D. Trifirò,²³ M. C. Tringali,^{89,90} L. Trozzo,^{136,21} M. Tse,¹² M. Turconi,⁵⁴ D. Tuyenbayev,⁸⁸ D. Ugolini,¹³⁷ C. S. Unnikrishnan,¹⁰⁰ A. L. Urban,¹⁸ S. A. Usman,³⁷ H. Vahlbruch,¹⁹ G. Vajente,¹ G. Valdes,⁸⁸ M. Vallisneri,⁷⁸ N. van Bakel,¹¹ M. van Beuzekom,¹¹ J. F. J. van den Brand,^{63,11} C. Van Den Broeck,¹¹ D. C. Vander-Hyde,³⁷ L. van der Schaaf,¹¹ J. V. van Heijningen,¹¹ A. A. van Veggel,³⁸ M. Vardaro,^{43,44} S. Vass,¹ M. Vasúth,⁴⁰ R. Vaulin,¹² A. Vecchio,⁴⁶ G. Vedovato,⁴⁴ J. Veitch,⁴⁶ P. J. Veitch,¹¹³ K. Venkateswara,¹³⁸ D. Verkindt,⁸ F. Vetrano,^{57,58} A. Viceré,^{57,58} S. Vinciguerra,⁴⁶ D. J. Vine,⁵¹ J.-Y. Vinet,⁵⁴ S. Vitale,¹² T. Vo,³⁷ H. Vocca,^{34,35} C. Vorvick,³⁹ D. V. Voss,⁶ W. D. Vousden,⁴⁶ S. P. Vyatchanin,⁵⁰ A. R. Wade,²² L. E. Wade,¹³⁹ M. Wade,¹³⁹ M. Walker,² L. Wallace,¹ S. Walsh,^{31,10} G. Wang,^{14,58} H. Wang,⁴⁶ M. Wang,⁴⁶ X. Wang,⁷¹ Y. Wang,⁵² R. L. Ward,²² J. Warner,³⁹ M. Was,⁸ B. Weaver,³⁹ L.-W. Wei,⁵⁴ M. Weinert,¹⁰ A. J. Weinstein,¹ R. Weiss,¹² L. Wen,⁵² P. Weßels,¹⁰ T. Westphal,¹⁰ K. Wette,¹⁰ J. T. Whelan,¹⁰⁴ B. F. Whiting,⁶ R. D. Williams,¹ A. R. Williamson,⁹¹ J. L. Willis,¹⁰³ B. Willke,^{19,10} M. H. Wimmer,^{10,19} W. Winkler,¹⁰ C. C. Wipf,¹ H. Wittel,^{10,19} G. Woan,³⁸ J. Woehler,¹⁰ J. Worden,³⁹ J. L. Wright,³⁸ D. S. Wu,¹⁰ G. Wu,⁷ J. Yablon,⁸³ W. Yam,¹² H. Yamamoto,¹ C. C. Yancey,⁶⁴ H. Yu,¹² M. Yvert,⁸ A. Zadrożny,¹¹⁴ L. Zangrando,⁴⁴ M. Zanolin,⁹⁹ J.-P. Zendri,⁴⁴ M. Zevin,⁸³ L. Zhang,¹ M. Zhang,¹²⁴ Y. Zhang,¹⁰⁴ C. Zhao,⁵² M. Zhou,⁸³ Z. Zhou,⁸³ X. J. Zhu,⁵² M. E. Zucker,^{1,12} S. E. Zuraw,¹²⁰ and J. Zweizig¹

(LIGO Scientific Collaboration and Virgo Collaboration)

*Deceased, March 2016. †Deceased, May 2015. ‡Deceased, March 2015.

¹LIGO, California Institute of Technology, Pasadena, CA 91125, USA

²Louisiana State University, Baton Rouge, LA 70803, USA

³American University, Washington, D.C. 20016, USA

⁴Università di Salerno, Fisciano, I-84084 Salerno, Italy

⁵INFN, Sezione di Napoli, Complesso Universitario di Monte S. Angelo, I-80126 Napoli, Italy

⁶University of Florida, Gainesville, FL 32611, USA

⁷LIGO Livingston Observatory, Livingston, LA 70754, USA

⁸Laboratoire d'Annecy-le-Vieux de Physique des Particules (LAPP), Université Savoie Mont Blanc, CNRS/IN2P3, F-74941 Annecy-le-Vieux, France

⁹University of Sannio at Benevento, I-82100 Benevento, Italy and INFN, Sezione di Napoli, I-80100 Napoli, Italy

¹⁰Albert-Einstein-Institut, Max-Planck-Institut für Gravitationsphysik, D-30167 Hannover, Germany

¹¹Nikhef, Science Park, 1098 XG Amsterdam, The Netherlands

¹²LIGO, Massachusetts Institute of Technology, Cambridge, MA 02139, USA

¹³Instituto Nacional de Pesquisas Espaciais, 12227-010 São José dos Campos, São Paulo, Brazil

¹⁴INFN, Gran Sasso Science Institute, I-67100 L'Aquila, Italy

¹⁵INFN, Sezione di Roma Tor Vergata, I-00133 Roma, Italy

¹⁶Inter-University Centre for Astronomy and Astrophysics, Pune 411007, India

¹⁷International Centre for Theoretical Sciences, Tata Institute of Fundamental Research, Bangalore 560012, India

¹⁸University of Wisconsin-Milwaukee, Milwaukee, WI 53201, USA

¹⁹Leibniz Universität Hannover, D-30167 Hannover, Germany

²⁰Università di Pisa, I-56127 Pisa, Italy

²¹INFN, Sezione di Pisa, I-56127 Pisa, Italy

²²Australian National University, Canberra, Australian Capital Territory 0200, Australia

²³The University of Mississippi, University, MS 38677, USA

²⁴California State University Fullerton, Fullerton, CA 92831, USA

²⁵LAL, Univ. Paris-Sud, CNRS/IN2P3, Université Paris-Saclay, Orsay, France

²⁶Chennai Mathematical Institute, Chennai 603103, India

²⁷Università di Roma Tor Vergata, I-00133 Roma, Italy

²⁸University of Southampton, Southampton SO17 1BJ, United Kingdom

²⁹Universität Hamburg, D-22761 Hamburg, Germany

³⁰INFN, Sezione di Roma, I-00185 Roma, Italy

³¹Albert-Einstein-Institut, Max-Planck-Institut für Gravitationsphysik, D-14476 Potsdam-Golm, Germany

³²APC, AstroParticule et Cosmologie, Université Paris Diderot, CNRS/IN2P3, CEA/Irfu, Observatoire de Paris, Sorbonne Paris Cité, F-75205 Paris Cedex 13, France

³³Montana State University, Bozeman, MT 59717, USA

³⁴Università di Perugia, I-06123 Perugia, Italy

³⁵INFN, Sezione di Perugia, I-06123 Perugia, Italy

³⁶European Gravitational Observatory (EGO), I-56021 Cascina, Pisa, Italy

³⁷Syracuse University, Syracuse, NY 13244, USA

³⁸SUPA, University of Glasgow, Glasgow G12 8QQ, United Kingdom

³⁹LIGO Hanford Observatory, Richland, WA 99352, USA

⁴⁰Wigner RCP, RMKI, H-1121 Budapest, Konkoly Thege Miklós út 29-33, Hungary

⁴¹Columbia University, New York, NY 10027, USA

- ⁴²Stanford University, Stanford, CA 94305, USA
- ⁴³Università di Padova, Dipartimento di Fisica e Astronomia, I-35131 Padova, Italy
- ⁴⁴INFN, Sezione di Padova, I-35131 Padova, Italy
- ⁴⁵CAMK-PAN, 00-716 Warsaw, Poland
- ⁴⁶University of Birmingham, Birmingham B15 2TT, United Kingdom
- ⁴⁷Università degli Studi di Genova, I-16146 Genova, Italy
- ⁴⁸INFN, Sezione di Genova, I-16146 Genova, Italy
- ⁴⁹RRCAT, Indore MP 452013, India
- ⁵⁰Faculty of Physics, Lomonosov Moscow State University, Moscow 119991, Russia
- ⁵¹SUPA, University of the West of Scotland, Paisley PA1 2BE, United Kingdom
- ⁵²University of Western Australia, Crawley, Western Australia 6009, Australia
- ⁵³Department of Astrophysics/IMAPP, Radboud University Nijmegen, P.O. Box 9010, 6500 GL Nijmegen, The Netherlands
- ⁵⁴Artemis, Université Côte d'Azur, CNRS, Observatoire Côte d'Azur, CS 34229, Nice cedex 4, France
- ⁵⁵Institut de Physique de Rennes, CNRS, Université de Rennes 1, F-35042 Rennes, France
- ⁵⁶Washington State University, Pullman, WA 99164, USA
- ⁵⁷Università degli Studi di Urbino "Carlo Bo," I-61029 Urbino, Italy
- ⁵⁸INFN, Sezione di Firenze, I-50019 Sesto Fiorentino, Firenze, Italy
- ⁵⁹University of Oregon, Eugene, OR 97403, USA
- ⁶⁰Laboratoire Kastler Brossel, UPMC-Sorbonne Universités, CNRS, ENS-PSL Research University, Collège de France, F-75005 Paris, France
- ⁶¹Carleton College, Northfield, MN 55057, USA
- ⁶²Astronomical Observatory Warsaw University, 00-478 Warsaw, Poland
- ⁶³VU University Amsterdam, 1081 HV Amsterdam, The Netherlands
- ⁶⁴University of Maryland, College Park, MD 20742, USA
- ⁶⁵Center for Relativistic Astrophysics and School of Physics, Georgia Institute of Technology, Atlanta, GA 30332, USA
- ⁶⁶Laboratoire des Matériaux Avancés (LMA), CNRS/IN2P3, F-69622 Villeurbanne, France
- ⁶⁷Université Claude Bernard Lyon 1, F-69622 Villeurbanne, France
- ⁶⁸Università di Napoli "Federico II," Complesso Universitario di Monte S. Angelo, I-80126 Napoli, Italy
- ⁶⁹NASA/Goddard Space Flight Center, Greenbelt, MD 20771, USA
- ⁷⁰RESCEU, University of Tokyo, Tokyo, 113-0033, Japan.
- ⁷¹Tsinghua University, Beijing 100084, China
- ⁷²Texas Tech University, Lubbock, TX 79409, USA
- ⁷³The Pennsylvania State University, University Park, PA 16802, USA
- ⁷⁴National Tsing Hua University, Hsinchu City, 30013 Taiwan, Republic of China
- ⁷⁵Charles Sturt University, Wagga Wagga, New South Wales 2678, Australia
- ⁷⁶West Virginia University, Morgantown, WV 26506, USA
- ⁷⁷University of Chicago, Chicago, IL 60637, USA
- ⁷⁸Caltech CaRT, Pasadena, CA 91125, USA
- ⁷⁹Korea Institute of Science and Technology Information, Daejeon 305-806, Korea
- ⁸⁰Università di Roma "La Sapienza," I-00185 Roma, Italy
- ⁸¹University of Brussels, Brussels 1050, Belgium
- ⁸²Sonoma State University, Rohnert Park, CA 94928, USA
- ⁸³Center for Interdisciplinary Exploration & Research in Astrophysics (CIERA), Northwestern University, Evanston, IL 60208, USA
- ⁸⁴University of Minnesota, Minneapolis, MN 55455, USA
- ⁸⁵The University of Melbourne, Parkville, Victoria 3010, Australia
- ⁸⁶Institute for Plasma Research, Bhat, Gandhinagar 382428, India
- ⁸⁷The University of Sheffield, Sheffield S10 2TN, United Kingdom
- ⁸⁸The University of Texas Rio Grande Valley, Brownsville, TX 78520, USA
- ⁸⁹Università di Trento, Dipartimento di Fisica, I-38123 Povo, Trento, Italy
- ⁹⁰INFN, Trento Institute for Fundamental Physics and Applications, I-38123 Povo, Trento, Italy
- ⁹¹Cardiff University, Cardiff CF24 3AA, United Kingdom
- ⁹²Montclair State University, Montclair, NJ 07043, USA
- ⁹³MTA Eötvös University, "Lendulet" Astrophysics Research Group, Budapest 1117, Hungary
- ⁹⁴National Astronomical Observatory of Japan, 2-21-1 Osawa, Mitaka, Tokyo 181-8588, Japan
- ⁹⁵Canadian Institute for Theoretical Astrophysics, University of Toronto, Toronto, Ontario M5S 3H8, Canada
- ⁹⁶School of Mathematics, University of Edinburgh, Edinburgh EH9 3FD, United Kingdom
- ⁹⁷Indian Institute of Technology, Gandhinagar Ahmedabad Gujarat 382424, India
- ⁹⁸University of Szeged, Dóm tér 9, Szeged 6720, Hungary
- ⁹⁹Embry-Riddle Aeronautical University, Prescott, AZ 86301, USA
- ¹⁰⁰Tata Institute of Fundamental Research, Mumbai 400005, India
- ¹⁰¹INAF, Osservatorio Astronomico di Capodimonte, I-80131, Napoli, Italy
- ¹⁰²University of Michigan, Ann Arbor, MI 48109, USA
- ¹⁰³Abilene Christian University, Abilene, TX 79699, USA
- ¹⁰⁴Rochester Institute of Technology, Rochester, NY 14623, USA
- ¹⁰⁵NCSA, University of Illinois at Urbana-Champaign, Urbana, Illinois 61801, USA

- ¹⁰⁶*Universitat de les Illes Balears, IAC3—IEEC, E-07122 Palma de Mallorca, Spain*
- ¹⁰⁷*University of Białystok, 15-424 Białystok, Poland*
- ¹⁰⁸*SUPA, University of Strathclyde, Glasgow G1 1XQ, United Kingdom*
- ¹⁰⁹*IISER-TVM, CET Campus, Trivandrum Kerala 695016, India*
- ¹¹⁰*Institute of Applied Physics, Nizhny Novgorod, 603950, Russia*
- ¹¹¹*Pusan National University, Busan 609-735, Korea*
- ¹¹²*Hanyang University, Seoul 133-791, Korea*
- ¹¹³*University of Adelaide, Adelaide, South Australia 5005, Australia*
- ¹¹⁴*NCBJ, 05-400 Świerk-Otwock, Poland*
- ¹¹⁵*IM-PAN, 00-956 Warsaw, Poland*
- ¹¹⁶*Monash University, Victoria 3800, Australia*
- ¹¹⁷*Seoul National University, Seoul 151-742, Korea*
- ¹¹⁸*The Chinese University of Hong Kong, Shatin, NT, Hong Kong SAR, China*
- ¹¹⁹*University of Alabama in Huntsville, Huntsville, AL 35899, USA*
- ¹²⁰*University of Massachusetts-Amherst, Amherst, MA 01003, USA*
- ¹²¹*ESPCI, CNRS, F-75005 Paris, France*
- ¹²²*Università di Camerino, Dipartimento di Fisica, I-62032 Camerino, Italy*
- ¹²³*Southern University and A&M College, Baton Rouge, LA 70813, USA*
- ¹²⁴*College of William and Mary, Williamsburg, VA 23187, USA*
- ¹²⁵*Instituto de Física Teórica, University Estadual Paulista/ICTP South American Institute for Fundamental Research, São Paulo SP 01140-070, Brazil*
- ¹²⁶*University of Cambridge, Cambridge CB2 1TN, United Kingdom*
- ¹²⁷*IISER-Kolkata, Mohanpur, West Bengal 741252, India*
- ¹²⁸*Rutherford Appleton Laboratory, HSIC, Chilton, Didcot, Oxon OX11 0QX, United Kingdom*
- ¹²⁹*Whitman College, 345 Boyer Avenue, Walla Walla, WA 99362 USA*
- ¹³⁰*National Institute for Mathematical Sciences, Daejeon 305-390, Korea*
- ¹³¹*Université de Lyon, F-69361 Lyon, France*
- ¹³²*Hobart and William Smith Colleges, Geneva, NY 14456, USA*
- ¹³³*Janusz Gil Institute of Astronomy, University of Zielona Góra, 65-265 Zielona Góra, Poland*
- ¹³⁴*King's College London, University of London, London WC2R 2LS, United Kingdom*
- ¹³⁵*Andrews University, Berrien Springs, MI 49104, USA*
- ¹³⁶*Università di Siena, I-53100 Siena, Italy*
- ¹³⁷*Trinity University, San Antonio, TX 78212, USA*
- ¹³⁸*University of Washington, Seattle, WA 98195, USA*
- ¹³⁹*Kenyon College, Gambier, OH 43022, USA*

(16 JUNE 2016)